Michael Johann Gleichweit, BSc

Optimization and Characterization of a High Temperature Optical Particle Counter for Automotive Applications

Master's Thesis

to achieve the university degree of

Diplom-Ingenieur

Master's degree programme: Technical Physics

submitted to

Graz University of Technology

Supervisor

Assoc.Prof. Dipl.-Ing. Dr.techn. Markus Koch
Institute of Experimental Physics

Co-Supervisor

Univ.-Prof. Mag.rer.nat. Dr.rer.nat. Alexander Bergmann
Institute of Electronic Sensor Systems

Graz, September 2019

Acknowledgement

I would first like to thank my thesis advisor Markus Koch of the institute for experimental physics for supervising my thesis. From him I have received more support, assistance and professional guidance than I expected, for which I want to express my deep gratitude.

Second, I would like to offer my special thanks to Co-supervisor Alexander Bergmann for all the invaluable information, remarks and comments throughout the process of this master thesis.

Without my colleagues from the institute for electronic sensor systems, writing this thesis would not have been possible. I would like to express great appreciation for their warm welcome and fruitful collaboration. They were always willing to help me and offered great support. I would particularly like to single out Martin Kupper for introducing me to the topic and his assistance during my laboratory work.

Finally, I wish to thank my parents for their encouragement and support throughout my studies.

This work was performed within the Competence Centre ASSIC - Austrian Smart Systems Research Center, co-funded by the Austrian Federal Ministries of Transport, Innovation and Technology (bmvit) and of Science, Research and Economy (bmwfw) as well as by the Federal Provinces of Carinthia and Styria within the COMET program.

Affidavit

I declare that I have authored this thesis independently, that I have not used other than the declared sources/resources, and that I have explicitly indicated all material which has been quoted either literally or by content from the sources used. The text document uploaded to TUGRAZonline is identical to the present master's thesis.

Eidesstattliche Erklärung

Ich erkläre an Eides statt, dass ich die vorliegende Arbeit selbstständig verfasst, andere als die angegebenen Quellen/Hilfsmittel nicht benutzt, und die den benutzten Quellen wörtlich und inhaltlich entnommenen Stellen als solche kenntlich gemacht habe. Das in TUGRAZonline hochgeladene Textdokument ist mit der vorliegenden Diplomarbeit identisch.

Datum

Unterschrift

Abstract

For the determination of particulate number concentration in automotive exhaust gasses particle number counters are prescribed (EU/ECE Regulation 83/49), where condensation particle counters (CPC) are the prevailing measurement instruments. Todays CPCs work at ambient temperatures, where volatile and semi-volatile contents of the exhaust gas are prone to condensation and lead to unpredictable adulterations during measurement. This necessitates appropriate pre-conditioning processes to measure solely solid particulates. However, current means to remove volatile and semi-volatile contents are complex, costly and subject to particle losses. The newly developed high temperature condensation particle counter operates at temperatures above 180°C, which is the boiling point of all major volatile exhaust gasses components. Thereby, all artefacts and interferences are avoided and pre-conditioning is rendered unnecessary.

Within this thesis a new optics unit that operates at these high temperatures was designed, built and thoroughly characterized. It features a thin laser light sheet above a nozzle that ejects the particles. Stray light created by particles traversing the light sheet is collected and imaged onto a photo diode detector. The design proved to be reliable and durable at all relevant temperatures.

Compared to prior solutions, the optical pulse duration was reduced from (560 ± 35) ns to (300 ± 20) ns ($1/e^2$-limit) by decreasing the laser light sheet width. Thereby, coincidence effects were significantly reduced and linearity for concentrations of up to $30.000\,{}^{\text{particles}}/_{\text{cm}^3}$ was confirmed, which marks the upper counting limit of the optical particle counter. The signal to noise ratio was enhanced from ∼8 to ∼23 for the photo diode detector and up to ∼50 is achievable with an avalanche photo diode detector.

The setup guarantees detection of particles with an efficiency comparable to state-of-the-art low temperature devices, does not require any realignment due to temperature variations and even allows minor initial misalignment. The high temperature condensation particle counter in combination with the new particle counting optics is now in a state, where the optimization process of the total instrument can be performed.

The following publication is associated to this master thesis:
Kupper, M., Kügler, M., Gleichweit, M., Kraft, M., Koch, M. & Bergmann, A. High-Temperature Condensation Particle Counter Optimized for Engine Exhaust. Article in preparation (2019)

Kurzfassung

Zur Bestimmung der Partikelanzahlkonzentration in Abgasen von Fahrzeugen sind Partikelzähler vorgeschrieben (UN/ECE Regulation 83/49), wobei in erster Linie Kondensations-Partikelzähler (Condensation Particle Counter, CPC) eingesetzt werden. Aktuelle CPCs arbeiten bei Umgebungstemperatur, bei der flüchtige Bestandteile der Abgase kondensieren können und so das Resultat unvorhersehbar beeinflussen. Um ausschließlich nicht-flüchtige Bestandteile zu vermessen, sind geeignete Maßnahmen nötig. Die gegenwärtigen Systeme zur Entfernung flüchtiger und teil-flüchtiger Stoffe sind aufwendig, teuer und weisen Partikelverluste auf. Ein neu entwickelter Prototyp eines Hochtemperatur-Kondensations-Partikelzählers arbeitet mit Betriebstemperaturen über 180°C, die über dem Siedepunkt der wesentlichen flüchtigen Abgaskomponenten liegen. Damit werden Kondensations-Artefakte und sonstige Interferenzen zuverlässig verhindert sowie die aufwendige Abgasaufbereitung umgangen.

In dieser Arbeit wurde eine bei solch hohen Temperaturen einsetzbare Partikelzähl-Optik entworfen, gefertigt und sorgfältig charakterisiert. Laserlicht wird über einer Düse zu einem dünnen Lichtblatt fokussiert. Partikel treten aus der Düse aus, passieren das Lichtblatt und erzeugen Streulicht, welches gesammelt und auf einen Photodiodendetektor abgebildet wird. Dieses Design hat sich bei allen relevanten Betriebstemperaturen als strapazierfähig und zuverlässig erwiesen.

Im Vergleich zu bestehenden Prototypen konnte durch Reduktion der Lichtblattdicke die optische Pulslänge von (560±35) ns auf (300±20) ns ($1/e^2$-Niveau) verringert werden. Dadurch wurden Koinzidenzeffekte vermindert und Linearität für Konzentrationen bis zu 30.000 $\mathrm{Partikel}/\mathrm{cm}^3$ ermöglicht, was zugleich die maximale Zählrate vorgibt. Der Signal-Rausch-Abstand konnte von ∼8 auf ∼23 für den Photodiodendetektor und ∼50 für einen Avalanche-Photodiodendetektor angehoben werden.

Die Zähleffizienz des neuen Designs ist vergleichbar mit jener von modernen Niedrigtemperatur-Optiken, nach einmaliger Ausrichtung justagefrei, temperaturstabil und lässt geringe Einrichtungsfehler zu. Der Hochtemperatur-Kondensations-Partikelzähler in Kombination mit der neuen Partikelzähl-Optik ist voll funktionstüchtig und kann einem Optimierungsprozess zugeführt werden.

Die folgende Publikation steht im Zusammenhang mit dieser Masterarbeit:
Kupper, M., Kügler, M., Gleichweit, M., Kraft, M., Koch, M. & Bergmann, A. High-Temperature Condensation Particle Counter Optimized for Engine Exhaust. Article in preparation (2019)

Contents

Index of Abbreviations

AC	Alternating Current
ADC	Analog Digital Converter
AOI	Angle of Incidence
APD	Avalanche Photo Diode
AR	Anti-Reflective
BFL	Back Focal Length
CAST	Combustion Aerosol Standard
CCD	Charge-Coupled Device, image sensor
CDF	Cumulative Distribution Function
CNC	Condensation Nucleus Counter
CNM	Condensation Nuclei Magnifier
CPC	Condensation Particle Counter
CS	Catalytic Stripper
CVS	Constant Volume Sampler
CWL	Center Transmission Wavelength
DBS	Dilution Bridge Stage
DC	Direct Current
DMA	Differential Mobility Analyzer
FFKM/FFPM	Full Fluoro-elastomeric material
FKM/FPM	Fluoro-elastomeric material (DIN ISO 1629; ASTM D1418)
FPGA	Field-programmable Gate Array
FWHM	Full Width Half Maximum
HEPA	High Efficiency Particulate Air (filter)
HTCPC/HT-CPC	High Temperature Condensation Particle Counter
IR	Infrared Radiation, Infrared Light
MFC	Mass Flow Controller
NIR	Near Infrared Radiation
OPC	Optical Particle Counter
PID	Proportional Integral Derivative
PM	Particulate Matter
PNC	Particle Number Counter
ppm	Parts Per Million
RTM	Ray Transfer Matrix
SCAG	Standard Combustion Aerosol Generator

SNR	Signal-to-Noise Ratio
SPN	Solid Particle Number
UV	Ultra violet light
UVFS	UV-fused silica window
WHO	World Health Organization

1. Introduction

Modern day's combustion engine powered vehicles are hardly emitting visible soot clouds anymore. Gasoline-powered automobiles are predominantly CO_2 emitters and usually do not fume from the exhaust, and if they do so, its most likely clouds of water vapour during cold winter days. However, just 20 years ago diesel-powered cars and lorries caught negative attention due to the dark smoke gushing from the exhaust pipe, especially under load conditions. Traditional diesel engine concepts were prone to aggregation of fuel droplets in the combustion chamber, that then caused large flakes of soot due to incomplete combustion processes. Today's diesel engines in combination with modern after-treatment of exhaust gases are far away from such conditions [2].

Nevertheless, diesel and nowadays also gasoline engines still produce soot particles, they just became less and, very importantly, smaller. In the pursuit of optimal combustion and highest fuel efficiency, the injectors used in current engines disperse the fuel in very fine droplets throughout the combustion chamber and combust with an excessive amount of air. This process gives rise to the formation of nanometer-sized particles, that are virtually invisible. As a consequence, diesel engines are attributed to be the main perpetrators of ultra-fine particles [2].

The emitted, ultra-fine particles are polluting the environment evermore and pose a threat to human health [3]. Epidemiologic studies show connections between *particulate matter* (PM) concentrations in the environment and health outcomes [4]. Early on, the American Medical Association found correlations, that link PM exposure to cancer formation [5][6]. In 2012 the *World Health Organization* (WHO) classified diesel exhaust gas as carcinogenic for humans [7] based on two studies that show close ties to lung cancer formation [8].

Prior to that, in the 1980s, the European Emission Standard directive was released in Europe, which introduced the EURO-1 norm in 1992 with the goal to limit the particle emissions to $0.14\,{}^{\mathrm{g}}/_{\mathrm{km}}$ [9]. By release of this work, the EURO-6 regulation standard (EU/ECE Regulation 83/49) is applicable, that allows an emission of only $5\,{}^{\mathrm{mg}}/_{\mathrm{km}}$ and a *Solid Particle Number* (SPN) of $6 \cdot 10^{11}\,{}^{\#}/_{\mathrm{km}}$ [10]. For that matter, the determination of the number concentration of particles in an aerosol becomes evermore important. But it faces some challenges, as the EU/ECE Regulation 83/49 itself raises the subject of revising the measurement methods.

1.1. Classification of particle sizes and their health impact

Deposition of soot particles in the human respiratory tract depends strongly on the particle diameter. Therefore, also the pollutant's size distribution becomes an important metric for health effects [3]. The upper respiratory tract filters out particles with sizes larger than 10 µm quite easily. Particles between 1 µm and 10 µm are more dangerous, because they are able pass the upper inhalation system and enter the pulmonary alveoli. Even smaller particles with diameters below 1 µm are considered the most carcinogenic. Such small objects can penetrate deep into the human lungs, where the lung clearance mechanisms are not very effective anymore [11][12].

Considering the health impacts, fine particles and micrometer-sized particles are considered as separate types of pollutants [3]. Appropriately, there is an established categorization for particle size measurements [13]: "PM10" with particles smaller than 10 µm and "PM2.5" with particles smaller than 2.5 µm. However, the number concentration of even smaller particles with sizes well below 100 nm gets increasingly relevant as combustion engine technologies progress [14].

1.2. Current means of detection of ultra-fine particles in automobile exhaust gases

The state-of-the-art device to measure particles with sizes down to a couple of nanometers in diameter is a *Condensation Particle Counter* (CPC), also sometimes referred to as *Condensation Nucleus Counter* (CNC). Such devices are built to count individual particles by optical means. The EU/ECE Regulation 83/49 [10] prescribes the general usage of *particle number counters* (PNCs) for SPN measurements on exhaust gasses. Today, CPCs are the prevailing instruments to perform such measurements.

In general, particles with sizes well below the wavelengths of visible light are not optically detectable due to the resolution limit. To circumvent this issue, the particles are "magnified" by a *Condensation Nucleus Magnifier* (CNM) first. A CNM uses the particles as condensation nuclei to form droplets in a supersaturated environment, where mainly n-butanol is used as working fluid nowadays [15, pp. 381]. Under controlled conditions heterogeneous condensation takes place that magnifies the particles to droplets of several micrometers in diameter, which is well above the optical detection limit. Traditional counting optics consists of a laser where the droplets pass through and some optical detection unit, that captures stray light generated by each droplet passage.

A CPCs detection limit is defined as the particle diameter at which the CNM is still able to magnify with 50% efficiency. It depends mainly on the conditions of the supersaturation, but also on the particle type (chemistry and morphology) in combination with the employed working fluid and the design itself [16]. Typical detection limits with modern devices are below 10 nm [2].

1.3. Motivation to develop a High Temperature Condensation Particle Counter

Regular CPCs are working just above room temperature ($\approx 40°C$), which is adventurous for electronics operating such a device and convenient due to short startup times. Exactly this low temperature, however, is the biggest drawback in the experiment with vehicular exhaust gases, because volatile components are prone to condensation and falsify the measurement non-reproducibly. Further, according to the EU/ECE Regulation 83/49, SPN is the relevant measure for vehicle manufacturers for type approval [10][14].

In order to conduct measurements on solid particles only, thus without any volatile particulars present, extensive sample pre-conditioning is necessary. Possible means are e.g. evaporation tubes, cyclones, catalytic stripping or hot dilution bridges [17]. All these methods of exhaust gas pre-conditioning introduce further uncertainties in measurement. Since CPCs with n-butanol are restricted to specific operating temperatures, there is no way to improve the concept based on that working fluid. A further drawback of n-butanol is its toxicity, which requires special disposal and ventilation during operation.

In 2012 Rongchai & Collings [18] proposed a *High Temperature Condensation Particle Counter* (HTCPC) that renders exhaust gas pre-conditioning unnecessary. The idea is to operate the section where the particles act as condensation nuclei at such high temperatures, that all major volatile components of the sample aerosol remain in the gas phase. In order to do so, the temperature has to be above 180°C. In 2014, Collings, Rongchai & Symonds [19] proved their concept with a variety of working fluids. As optical counting unit, the system of a commercial n-butanol-driven CPC ("TSI 3034") was taken over and thermally isolated to protect its electrical components from overheating. However, they never reported long term stability.

Kupper, Kraft, Bergmann & Boies [20] are working on a very similar concept, featuring again a different working fluid and which enables lower operating temperatures in the saturator section compared to Collings, Rongchai & Symonds. The aim is first and foremost the development of a particle counter for direct automotive exhaust gas measurements, but also enabling interference-free measurement in highly humid environments or other defiled aerosols with little or no pre-conditioning. Kügler [21]

already presented the proof of principle for this HTCPC in his master thesis. What is left to be done is the development of an optical module for particle counting, which is able to withstand temperatures of up to 235°C, and the characterization of the final setup.

1.4. Challenges in optics at high temperature operation

The counting optics for any CPC has to be operated such that condensation of working fluid in the optics unit itself, especially on lenses or windows, is prevented. Collings, Rongchai & Symonds chose to use an existing optics unit and to "isolate" the hot particle stream with a sheath-flow from the cold components and thereby circumventing the problem of condensation [19]. Another way is to operate the whole optical unit at temperatures higher than the aerosol stream that transports the particles.

In this work the second approach is pursued. With an operating temperature of up to 220°C for the HTCPC used in this work and assuming a safety margin of 15°C, this concept implies that the optics unit must be designed to permanently withstand temperatures of 235°C. The first issue that has to be addressed is the lens and window material. Regular N-BK7, B270 and fused silica glasses (UVFS) withstand these temperatures. However, standard materials for anti-reflective coatings of optical components do not. Consequently, either un-coated lenses and windows have to be used or a suitable coating has to be found.

Black body radiation in the infrared part of the spectrum has to be considered as well. Silicon photo detectors pick up NIR radiation of up to 1100 nm. Although the IR intensity is very low for the temperatures expected in this work, the surface area may be large enough to cause considerable background noise on the detector.

More on the mechanical side, the aspect of thermal expansion has to be considered. Thermally induced stress may cause bending or distortion of the setup, thereby influencing focal points and beam paths. By preference, the design should be inherently stable against misalignment due to thermal expansion. A configuration or realignment during operation is neither practicable nor desirable. And last but not least, the optics unit has to be air-tight since the HTCPC is operated under low pressure. The utilized gaskets and O-ring seals have to be made from special material (e.g. FEPM/FFKM).

2. Fundamentals

Laser light is the most important tool used in this work. For this reason, the basics of the Gaussian laser beam shape and the relations between the most important beam parameters are discussed in the section about Gaussian beam.

A second very important topic is light scattering at microscopic particles. In the section about Mie theory, the basic mathematical approach is elucidated and the most important implications for this work are discussed.

2.1. Gaussian beam

When looking at light interacting with objects much smaller than its wavelength, the common model of harmonic plane-waves is most adequate to describe the process. However, for the description of a true laser focus region, this model becomes insufficient. Inherently, every laser beam has some beam divergence, which origins from the finite beam diameter. As a consequence, the beam has non-planar wavefronts, that can be pictured as curved surfaces when looking at constant phase angles. This contradicts the concept of plane harmonic waves, since the intensity is not constant over the beam cross section [22, pp. 27].

A much more realistic description, that fits most cases which involve the transverse fundamental mode of typical laser sources, is the so-called Gaussian beam [22]. Figure 2.1(a) shows the traverse profile of a Gaussian beam and Fig. 2.2(a) shows the beam propagation and the wavefronts close to the focal point.

2.1.1. Mathematical description and beam parameters

For a first description, the Gaussian beam is assumed to be a rationally symmetric laser beam with respect to the propagation direction. Therefore, it is convenient to choose cylinder coordinates with the positive z-axis as propagation direction (= optical axis). The radial flux density $I(r, z)$, or irradiance, is then decreasing radially outwards following a Gaussian function, given by

$$I(r,z) = I(0,0)\left(\frac{w_0}{w(z)}\right)^2 \mathrm{e}^{-2\left(\frac{r}{w(z)}\right)^2}, \tag{2.1}$$

where $I(0,0)$ describes the flux amplitude (= peak irradiance) at the beam center in the focal point, w_0 the minimum beam radius at the focal point, also called *beam waist*, and $w(z)$ the beam radius in dependence of the beam propagation, also simply called the *beam radius*. The factor $\left({}^{w_0}/_{w(z)}\right)^2$ serves as the normalization and guarantees energy conservation, since for larger beam radii the irradiance per solid angle must decrease [23, p. 32].

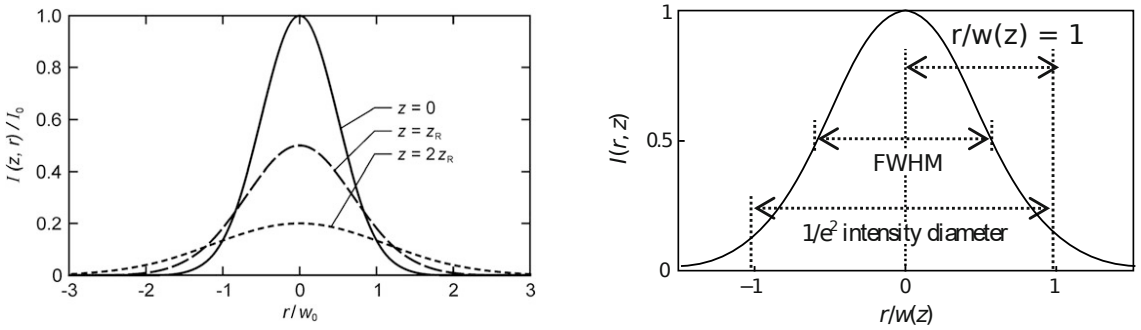

(a) Gaussian beam profile[1]

(b) FWHM and $1/e^2$-width[2]

Figure 2.1.: Gaussian beam profile and beam radius. (a) The normalized Gaussian beam profile is plotted at the focal point (solid line), at the Rayleigh length z_R (coarse dashed line) and at twice the Rayleigh length $2z_R$ (fine dashed line). (b) A Gaussian function is commonly described by either the *full width at half maximum* (FWHM) or the width at $1/e^2$-level.

As indicated in Fig. 2.1(b), the beam radius $w(z)$ is defined as half of the Gaussian profiles diameter, where the irradiance has decreased to a factor of $1/e^2 (= 0.135)$ [22, p. 28][23, p. 34]. It is further a function of the beam waist w_0 and the parameter z_r,

$$w(z) = w_0 \sqrt{1 + \left(\frac{z}{z_r}\right)^2}. \tag{2.2}$$

In Fig. 2.2(b) the beam radius is plotted as a function of distance along the optical path. Appropriately, at the focus point ($z = 0$) the beam radius becomes the beam waist and for any z larger than zero the beam radius grows. For $z = z_r$, which is called the *Rayleigh length*, the beam radius increased by a factor of $\sqrt{2}$ [23, p. 33]. It is also indicated in Fig. 2.1(a) and given by

$$z_r = \frac{k w_0^2}{2} = \frac{\pi w_0^2}{\lambda}, \tag{2.3}$$

where k is the wavenumber and λ is the wavelength of the applied laser light. The so-called *Rayleigh range* is the region of $\pm z_r$ around the focal point and is indicated as shaded a area in Fig. 2.2(a). For any z below the Rayleigh length (near field) the beam

[1] Figure taken from Donges & Noll, *Laser Measurement Technology* [22].

[2] Figure taken from Sun, *A Practical Guide to Handling Laser Diode Beams* [23] and slightly modified.

radius is about the size of the beam waist ($w(z) \approx w_0$) and is therefore considered independent of z. Far away from the focal point, well outside the Rayleigh length (far field), the beam radius grows almost linear with z [23, p. 34].

$$w(z) = \frac{w_0}{z_r}|z|$$

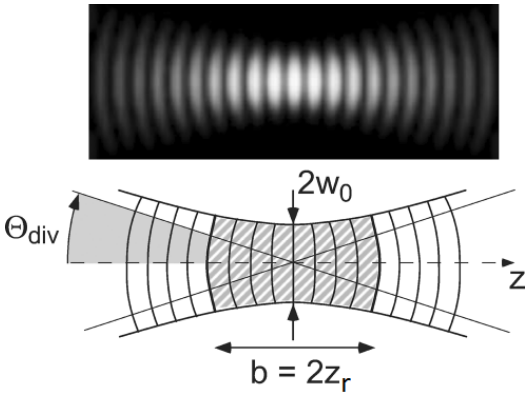

(a) Gaussian beam parameters[3]

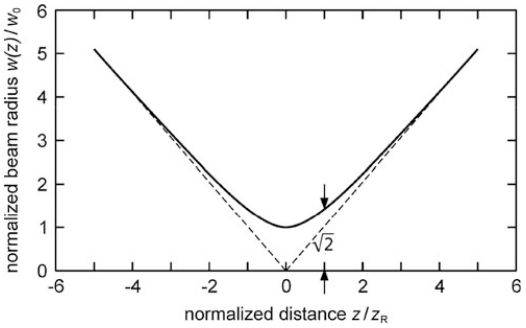

(b) Beam radius in propagation direction[4]

Figure 2.2.: Gaussian beam in the focal region. (a) Top: A still image indicating the wave fronts propagating trough the focal region. Bottom: A description of the beam parameters in the focal region, $2w_0$... beam diameter, $2z_r$... Rayleigh range, Θ_{div}... far-field divergence angle, (b) The beam radius as a function of distance from the focal point (see Eq. (2.2)), normalized to the Rayleigh length z_r.

In Fig. 2.2(a) the *far-field divergence angle* Θ_{div} is indicated. Simple trigonometry together with Eq. (2.3) yields

$$\tan(\Theta_{\text{div}}) = \frac{w_0}{z_r} = \frac{\lambda}{\pi w_0}. \tag{2.4}$$

The wavelength is in general much smaller than the attainable beam waist, so the approximation $\tan(\Theta_{\text{div}}) \approx \Theta_{\text{div}}$ is valid. Rearranging Eq. (2.4) yields

$$\Theta_{\text{div}} w_0 \cong \frac{\lambda}{\pi}, \tag{2.5}$$

which indicates that for a given wavelength the product $\Theta_{\text{div}} \cdot w_0$ is a conservation quantity. That means, to reduce the beam waist, the far-field divergence angle has to be increased, which associated with a reduction of the lenses focus length and an increase of lens diameter. Another implication is, that in order to further reduce the beam waist for a given divergence angle, the wavelength has to be reduced.

[3]Figure taken from Meschede, *Optik, Licht und Laser* [24].
[4]Figure taken from Donges & Noll, *Laser Measurement Technology* [22].

2.1.2. Connection between FWHM and the beam radius w(z)

The beam radius $w(z)$ is defined as the distance from the beam center to the point, where irradiance has reduced to 13.5% ($=1/e^2$) compared to peak irradiance. The definition of Full-Width-Half-Maximum (FWHM) is the full beam width at the level where the irradiance reaches half of its maximum. Both cases are illustrated in Fig. 2.1(b).

Starting from Eq. (2.1), the relation between the FWHM and the $1/e^2$ beam width can be derived. The whole pre-factor is set to I_0, since the relation must hold for any position z along the optical path. For the radius r_{FWHM}, where the beam irradiance is half of its maximum, we can write

$$\frac{I_0}{2} = I_0 \exp\left(-2\left(\frac{r_{\mathrm{FWHM}}}{w(z)}\right)^2\right). \tag{2.6}$$

The FWHM is then twice that radius,

$$\mathsf{FWHM} = 2r_{\mathrm{FWHM}}.$$

Per definition, $w(z)$ describes the beam radius at the $1/e^2$-level and Eq. (2.6) simplifies to

$$-2\ln(0.5) = \frac{\mathsf{FWHM}^2}{w(z)^2}.$$

The relation to convert from the total beam width $2w(z)$ to FWHM results in

$$\mathsf{FWHM}(z) = w(z)\sqrt{2\ln(2)} = 2w(z)\cdot\sqrt{\frac{\ln(2)}{2}} = 2w(z)\cdot 0.5887, \tag{2.7}$$

or in turn for FWHM to the total beam width

$$2w(z) = \mathsf{FWHM}(z)\sqrt{\frac{2}{\ln(2)}} = \mathsf{FWHM}(z)\cdot 1.699. \tag{2.8}$$

The formulas Eq. (2.7) and Eq. (2.8) enable now to convert one definition of beam width to the other.

2.2. Mie theory

In 1908, Gustav Mie formulated a mathematical description of colour effects of gold nano-particles in a suspension [25]. Today the set of equations from this work are known as Mie Theory. It describes the angular intensity distribution of light scattered by a spherical particle and can be understood as interference of waves diffracted by an object. Thus, rather simple measurements of the angular intensity distribution give information about the object properties. To this day, Mie theory is used to determine size and index of refraction of microscopic particles.

2.2.1. Angular intensity distribution of scattered light

The mathematics behind Mie theory is beyond the scope of this work, therefore only some key points are described here. For further reading, please refer to the work of Baron [15], Kerker [26] and Mie [25] in literature.

Mie Theory provides an analytical solution to the Maxwell-equations in spherical coordinates and describes scattering of plane electromagnetic waves from spherical objects of arbitrary size [27][15, pp. 276]. Thereby, Mie expressed both incoming and outgoing electromagnetic waves as a series of spherical wave functions [25, pp. 383]. With the boundary conditions known from classical electrodynamics, the expansion coefficients are determined and an expression for the electromagnetic field for all solid angles can be derived analytically. Since there are no constraints for the sphere diameter, Mie theory explains Rayleigh-Scattering as well as phenomena in geometrical optics[5].

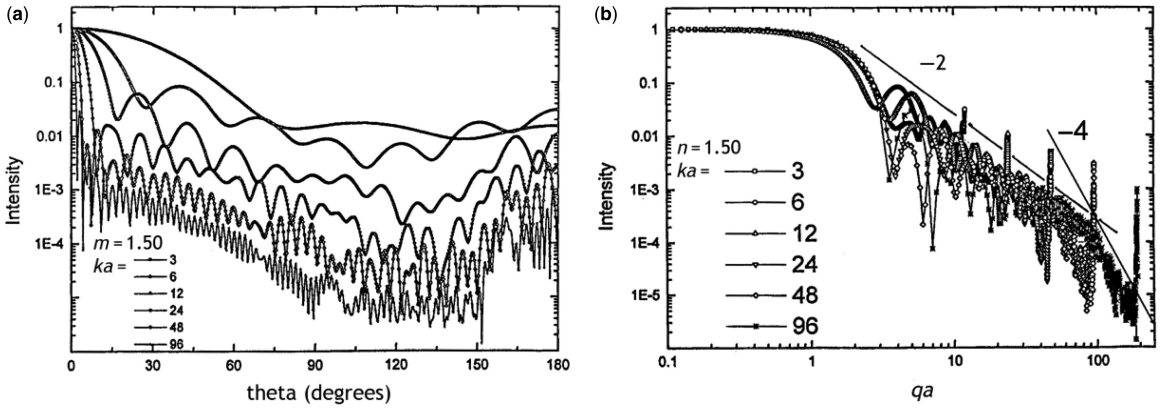

Figure 2.3.: Scattered intensity according to Mie-theory for different size parameters[6]. Calculations are performed for one ratio of indices of refraction, $m = {}^{n_{\text{sph}}}/_{n_{\text{amb}}} = 1.5$. The normalized intensity ${}^{I_e}/_{\max(I_e)}$ is plotted over (a) the scattering angle Θ, and (b) the dimensionless product qa (see Eq. (2.11)), on a logarithmic scale. Where in the left figure no clear pattern is recognizable, the plot in the right figure clearly shows a systematical behaviour.

Alongside many other quantities, Mie theory yields an equation describing the light intensity scattered towards certain angles,

$$I_e(\Theta, \Phi) = \frac{I_i}{(ka)^2} \left(S_1^2 \sin^2\Phi + S_2^2 \cos^2\Phi \right), \tag{2.9}$$

with

$$S_{1,2} = S_{1,2}(\Theta, n_{\text{sph}}, n_{\text{amb}}, ka).$$

The polar angle Θ, also called the *scattering angle*, is defined as the angle between the scattered ray and the optical axis. The azimuthal angle Φ is the angle between the

[5]Diffraction of light by spherical objects much larger than the light wavelength.

[6]Figure taken from Baron, *Aerosol measurement* [15].

scattered ray and one particular direction perpendicular to the optical axis. Hence, the problem is rotationally symmetric in Φ. To calculate the angular intensity distribution, the sphere radius a, the indices of refraction for the sphere n_{sph} and the surroundings n_{amb}, as well as the wavelength λ of the incoming light have to be known. Mie also defined the size parameter ka as independent variable,

$$ka = \frac{2\pi a}{\lambda}. \tag{2.10}$$

S_1 and S_2 in Eq. (2.9) are the scattering functions written as an infinite series expansion in Legendre polynomials, where each expansion coefficient depends on the indices of refraction, the scattering angle and an additional factor which depends on spherical Bessel functions ("Riccati-Bessel functions") with the size parameter as argument. Most of the work in calculating the angular intensity distribution goes into determining these scattering functions [28].

Figure 2.3(a) shows the scattered intensity for different size parameters ka plotted over the angle Θ. However, the radius together with the scattering wave vector q,

$$q = \frac{4\pi}{\lambda}\sin\left(\frac{\Theta}{2}\right), \tag{2.11}$$

gives the dimensionless product qa, that turns out to be a much more convenient parameter, as Fig. 2.3(b) shows. When plotted over qa, the scattered intensity distribution may be qualitatively separated into three regimes.

- $I \propto (qa)^0$ for $qa < 1$, or $a \ll \lambda$
  The curve is flat. For objects much smaller than the wavelength, the Rayleigh scattering approximation [22, pp. 56] is valid.

- $I \propto (qa)^{-2}$ for $1 < qa < \rho$, or $a \approx \lambda$
  The curve follows a power law of second order. This is the so called Mie-scattering regime. At the low end, there is a fluent transition from Rayleigh scattering to Mie-scattering when the wavelength approaches the object size. The upper boundary is characterized by the phase shift parameter ρ,

  $$\rho = 2ka\left|\frac{n_{\text{sph}}}{n_{\text{amb}}} - 1\right|.$$

  It describes the phase difference between a wave that propagates without disturbances in the ambient medium and one that passes directly, head on through the sphere and has a longer optical path to run through [15, p. 274].

- $I \propto (qa)^{-4}$ for $qa > \rho$, or $a \gg \lambda$
  The curve follows a power law of fourth order. This is called the Geometric scattering regime, also sometimes referred to as Porod-regime in the context of Rayleigh-Debye-Gans scattering [15, pp. 274]. Here, the scattered intensity approaches the solutions found with classical geometric optics.

2.2.2. Visualization of the intensity distribution

Equation (2.9) allows us to calculate and plot the scattered intensity distribution for configurations used in this work. The complex code to calculate the scattering functions in Eq. (2.9) is based on the work of Schäfer in his Ph.D. thesis [29]. Figure 2.4 shows the simulation, assuming a vertically polarized laser source with a wavelength of $\lambda = 635$ nm and spheres made from Eicosane, which has an index of refraction of $n_{C_{20}H_{42}} \approx 1.44$ [30]. For larger sphere sizes, the light is predominantly scattered in forward direction. For smaller particles the cone gets wider and more back-scattering occurs. The black and cyan colored lines indicate the angular aperture for two different lens setups, discussed later in Sec. 4.1 and Sec. 6.1.

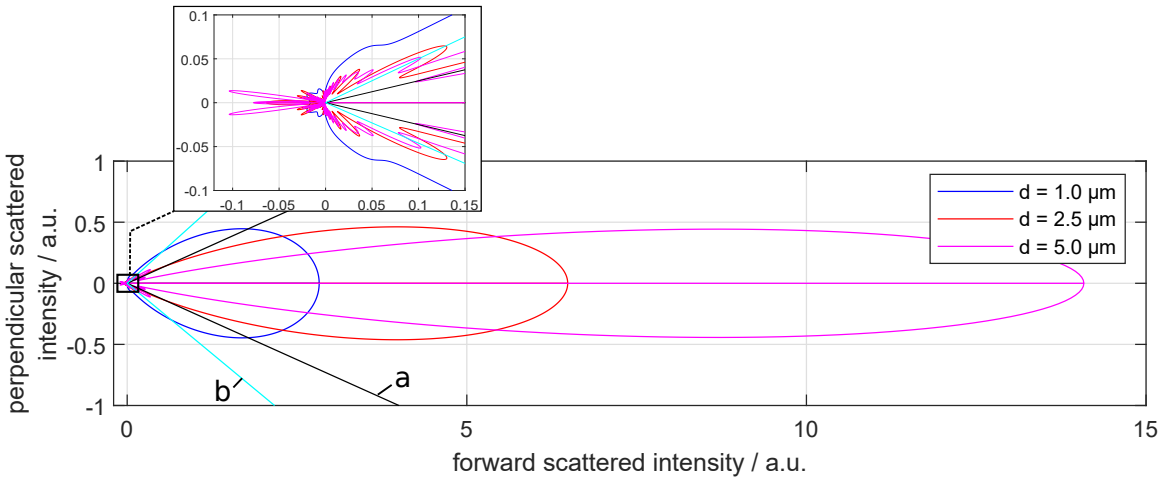

Figure 2.4.: Normalized scattered intensity according to Mie-theory. For three different sphere sizes, the scattered intensity is calculated and normalized to unity area. with respect to the maximal intensity. The index of refraction of Eicosane is set as the sphere material property, the surrounding material is assumed to be nitrogen gas with a refractive index of $n_{N_2} \approx 1$. Vertically polarized light with a wavelength of $\lambda = 635$ nm is incident from the left. Numerical aperture for (a, black) 2f setup, NA = 0.243, and (b, cyan) microscope like setup, NA = 0.447.

In Figure 2.5 the total scattered intensity is plotted for the particle diameters relevant for this work. It is clearly visible that the amount of scattered light increases for larger particle diameters and decreases rapidly as the particle diameter approaches the order of the light wavelength. Note that the absolute amount of scattered light radiated in all directions of space is plotted and therefore includes back-scattering.

The lobes forming in Fig. 2.4 and the ripples visible in Fig. 2.5 are complicated to understand. For different sets of parameters, different regularities, or even irregularities, for the patterns have been found. For example, Nussenzveig [31] explained some patterns with scattering induced by surface waves on the spheres. On the other hand he describes very different patterns in the form of “resonating” waves, that orbit

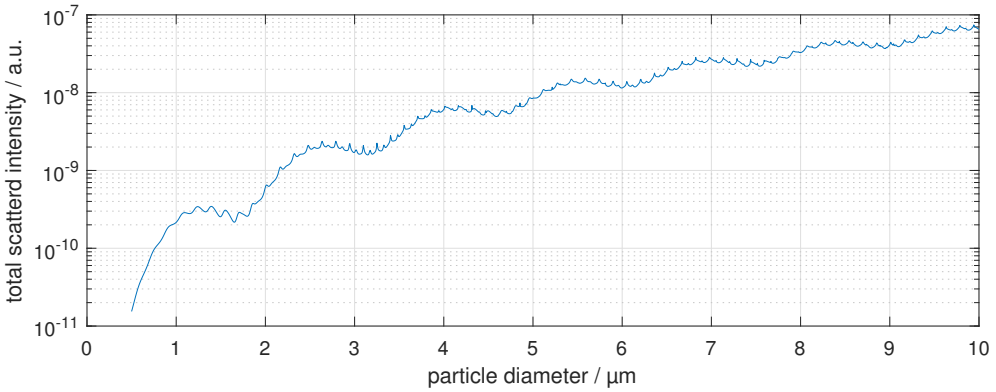

Figure 2.5.: Total scattered intensity according to Mie-theory plotted for particle diameters from 500 nm to 10 µm and a wavelength of $\lambda = 635$ nm. Mie-theory predicts changing scattering cross sections for the scattering parameter qa, which is proportional to the particle diameter here, since the wavelength is fixed. For small particles we see a lot less intense light scattering than for larger particles due to the decreasing scattering cross-section.

within the particle while experiencing (near-) total internal reflection. However, this phenomenon will not dominate here, because the particles where light will be scattered from are neither perfect spheres nor of exactly the same diameter. And last, but not least, they are moving with some velocity and therefore hit from various angles during the passage through the laser.

3. Methodology

This chapter focuses on the main instruments used in this work. First, an outline of the working principles of the laboratory equipment will be given to understand the main restrictions of experiments conducted later on. Then, the HTCPC is described in more detail.

3.1. Instrumentation

The focus of this section will be on the main devices and non-standard components found in measurement set-ups of this document. Any additional standard equipment or well documented appliances are cross-referenced in the text as they are mentioned and the reader is encouraged to do further reading on these items using the references.

3.1.1. Conventional Condensation Particle Counter - CPC

Already in the 1880s, John Aitken used condensation to grow water droplets from particles, that would have been too small to see under magnifying glasses otherwise. Since then, this basic idea lead to the development of instruments that are capable of detecting nano-particles. The latest, commercially available device is able to detect particles of diameters down to 2.5 nm [32].

The principle is rather simple: Particles in a supersaturated environment act as condensation nuclei. In theory, each particle produces one droplet. However, the probability that a particle triggers condensation depends on many parameters. The particle size and morphology are of course of great importance, but the working fluid's diffusion coefficient, vapor pressure and temperature of the surrounding volume, the vapor pressure and temperature of the particle interface, the molar volume and finally the chemical interplay between working fluid and particle substance are important, too. Further, for particles with sizes below 100 nm, the Knudsen number gets relevant as the particle diameter approaches the molecular mean free path length of the vapour. By knowing the material constants and controlling all operation parameters, homogeneous particle growth in the supersaturated vapor can be achieved [15, pp. 385].

The *Kelvin diameter* d* usually refers to the critical diameter for which condensation on a particle takes place, and thereby defines the cut-off for a CPC. The cut-off refers to the particle diameter, where still 50% trigger the formation of a droplet. This parameter changes naturally with the particle chemistry, so different counting efficiencies and cut-offs are expected for different particle sources.

In the past century, three fundamental ways to create such supersaturation have been developed. The techniques of adiabatic expansion, mixing of hot with cold streams and thermal diffusion (or "conductive cooling"). The latter is the most common type of CPC. All CPCs used in this work, including the HTCPC, are of this conductive cooling type.

In conductive cooling type CPCs, supersaturation of the working fluid is induced by diffusional cooling of the working fluid. It is a two stage process that also supports a steady flow of vapor through the system, thus enabling a continuous operation. First, in a saturator the environment, i.e. a carrier gas, is saturated with the working fluid utilizing a wick[1]. The (regular) saturated gas then flows into the condenser section, where it is chilled by thermal conduction with cooled walls, hence the name "conductive cooling". The nanometer-sized particles for nucleation are either in the stream from begin with ("full-flow"-type) or get injected directly into the condenser tube with a separate sample flow ("mixing-inlet"-type).

Once the growth of particles in the condenser is ensured, they are counted one by one with *optical particle counters* (OPC).

TSI 3775

The TSI 3775 is an n-butanol driven CPC of thermal diffusion type (conductive cooling) manufactured by the company "TSI Incorporated". Figure 3.1 shows the flow schematics of this device. It uses a "full-flow"-type CNM which funnels the sample aerosol through the saturator. In the OPC a regular laser diode with focusing optics and two photo diodes are used. One photo diode measures light transmission through the particle stream and the other one scattered light from particles at an angle of 90 degrees to the optical axis. The saturator is operated at 39°C, the condenser at 14°C and the optics at 40 °C. With this differential temperature, the detection limit is at about 4 nm for this device.

The flow rate through the CNM itself is limited by a critical orifice to 0.3 l/min. Alternatively, a bypass allows to draw 1.3 l/min from the sample inlet, which is of advantage to increase response time and to reduce particle loss is tubing. [33]

[1] A porous material that provides a very large surface area for the fluid to enhance evaporation.
[2] Figure taken from TSI Incorporated, *Condensation Particle Counter 3775* [33].

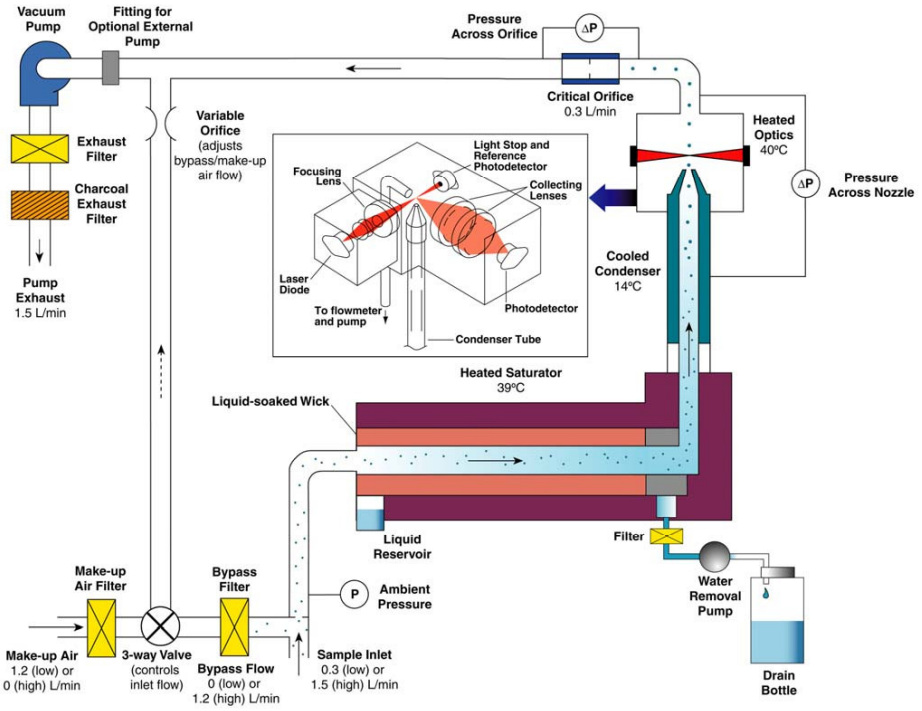

Figure 3.1.: Schematics of the flow in a TSI 3775 CPC[2].

Laboratory CPC

In this work the term "Laboratory CPC" refers to a CNM developed by Kraft, Reinisch & Bergmann [16]. This unit is, like the TSI 3775, a n-butanol driven "full-flow"-type device, whose geometry is developed for a continuous sample flow of up to $1\,{}^{l}/_{min}$. It is implemented in the commercially available "APCplus" AVL Particle Counter, marketed by AVL List GmbH. Figure 3.2 shows the concept of this CPC. The actual CNM used later in this work features a more complicated wick structure and a more sophisticated condenser design that are both undisclosed, but they are not of concern for this work.

The standard operation conditions are 38 - 40°C for the saturator, 26°C the condenser and 40°C for the optics. With this temperature difference, a detection limit of about 23 nm is reached. A lower Kelvin diameter can be achieved by increasing the temperature difference between saturator and condenser.

This CPC can be operated with either low-pressure or over-pressure. In the operation with low-pressure, a pump sucks the particle loaded sample aerosol into the CNM, through a nozzle for a particle jet and across the optical unit. In this case, the optical unit has to be air-tight. Alternatively, gas may be pushed through the device using

[3]Figure taken from Kraft, Reinisch & Bergmann, "Non-reactive Working Fluids for Reliably Sensing Nanoparticles in Automotive Exhaust Gases" [16].

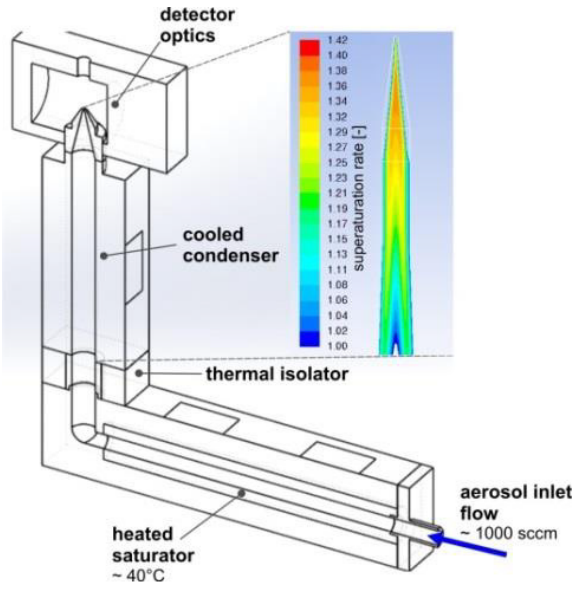

Figure 3.2.: Basic concept of the laboratory CPC[3].

compressed air in combination with a Venturi nozzle prior to the saturator to sample the particle loaded aerosol. In this operation mode, the CNM shoots out the grown droplets at the top nozzle, which enables straight-forward light scattering experiments without the need of enclosed or even air-tight setups. However, a very good ventilation is needed, since n-butanol is toxic.

3.1.2. Catalytic Stripper

Catalytic strippers are part of pre-conditioning systems to remove volatile and semi-volatile[4] components from exhaust gasses, before classification of particle sizes and determination of number concentration takes place. This pre-conditioning is necessary, since for automotive applications the EU/ECE Regulation 83/49 [10] prescribes measurement of SPN only[5]. Extra (semi-)volatile components in the aerosol would cause artefacts and thus interfere with the measurement by conventional n-butanol driven CPCs [15, p. 121, 136][34].

In Fig. 3.3 the principle is illustrated. The idea is to use an evaporation tube in combination with an oxidation catalyst. The evaporation tube heats the sample

[4]Particles that evaporate only above 100°C, but below the pyrolysis threshold (about 350°C) [17].

[5]The catalytic stripper is actually not conformable to the regulation, which dictates the use of an Evaporation Tube operated at 350°C. However, for laboratory measurements the catalytic stripper is a good substitute.

[6]Figure taken from Giechaskiel *et al.*, "Review of motor vehicle particulate emissions sampling and measurement: From smoke and filter mass to particle number" [17] and slightly modified.

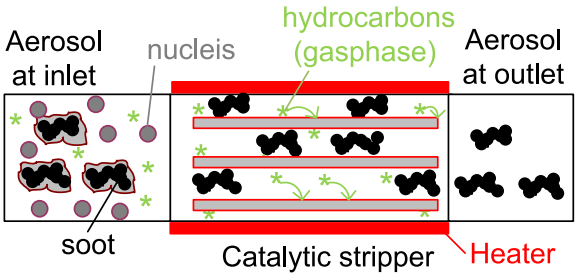

Figure 3.3.: Basic concept of the Catalytic Stripper[6]. Sample aerosol enters the evaporation tube from the left and get heated up, such that the condensed volatile components (nuclei) turn into the gas phase. The oxidation catalyst then removes the hydrocarbons and sulfates. Only solid particles exit on the right.

aerosol to evaporate volatile compounds, where usually temperatures above 250°C are needed to evaporate semi-volatile particles as well. In the oxidation catalyst volatile hydrocarbons are oxidized and sulfates are bound due to adsorption. The precipitation efficiency is dominated by the residence time (which in turn depends on the flow rate and instrument size) and the (semi-)volatile compound concentration. A treatment of the sample flow with this chemical approach practically eliminates the risk for subsequent nucleation or re-condensation, assuming appropriate dimensions of the instrument. Together with an additional sulfur trap, this instrument counts to the most efficient procedures for pre-conditioning of exhaust gases prior to SPN-measurements. A drawback, however, is the particle loss inside the catalyst [17].

The catalytic stripper used in this work consists of a stand-alone commercial oxidation catalyst followed by a simple heat exchanger (cooling tube). The latter is necessary to cool the aerosol back to ambient temperature for further processing.

3.1.3. Differential Mobility Analyzer - DMA

A Differential Mobility Analyzer is the main instrument for particle size distribution measurements. Some literature may also refer to it as *differential electrical mobility classifier* (DEMC). The norm "ISO15900" thoroughly describes all necessary definitions about how a DMA is supposed to work. Here, only a brief outline about the function principle will be given.

The size of a particle strongly influences its mobility and thus its behavior. In different regimes, one can assign particles certain *mobility equivalent diameters*. For particles larger than 300 µm, where inertial behavior still dominates, the *aerodynamic diameter* is a good measure. It describes the diameter of an equivalent sphere which settles at the same terminal velocity [15, p. 531]. However, for particle sizes in the region of the mean free path of surrounding gas molecules and below, the behavior is less guided by inertia, but dominated more by Brownian motion instead. This is exactly the case for

nanometer-sizes objects in air under atmospheric conditions. For classifying particle sizes with a DMA the *electrical mobility diameter* will be important. It describes the diameter of an equivalent spherical particle that shows the same migration rate (*electrical mobility*) in an electric field [15, p. 6, 240, 242].

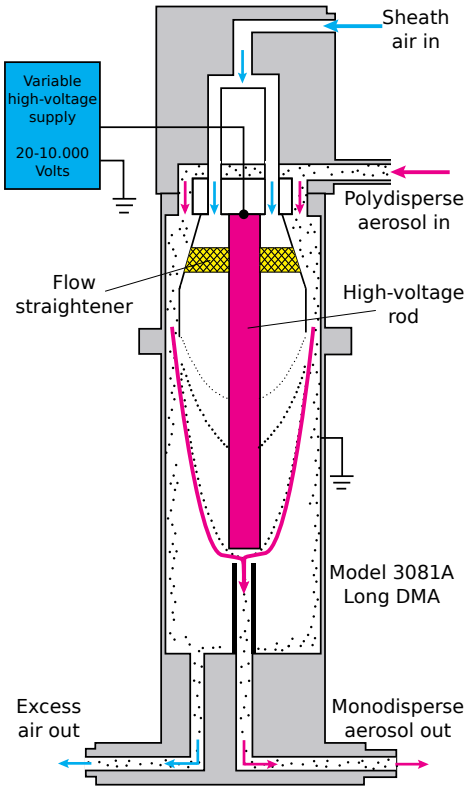

Figure 3.4.: Basic concept of the TSI 3082 Differential Mobility Analyzer[7]. The particles are charged, e.g. by a bipolar diffusion charger, before they reach the aerosol inlet and enter the electric field on the top rim of the cylinder capacitor. Negative charged particles hit the outer capacitor plate. Positive charged particles join the sheath air flow, while being deflected towards the center electrode. Only Particles with a certain electrical mobility diameter can enter an annular slit downstream and exit the column. All other particles either precipitate earlier on the center electrode or leave the column together with the sheath flow as excess air.

As shown in Fig. 3.4 the DMA is in principle a coaxial flow precipitator, which utilizes a high-voltage cylindrical capacitor consisting of two nested rods that act as electrodes. Particles that traverse the zone between the inner and outer electrode get deflected according to their electric charge and electric mobility.

The sample aerosol is passed into the electric field close to the inner surface of the cylinder hull, which functions as outer electrode. Simultaneously, a particle-free laminar

[7]Figure taken from TSI Incorporated, *Electrostatic Classifier Model 3082* [35] and slightly modified.

flow, the so-called *sheath air*, flows down the column. Starting from the point where both streams are joined, positively charged particles are deflected towards the inner electrode. Negatively charged particles immediately hit the outer wall. Particles with high electrical mobility move faster towards the center, while the ones with lower mobility arrive there further down. Only a narrow range of particles with a certain electrical mobility diameter can enter an annular slit at one position of the inner electrode. Those particles are then mono-disperse according to their *mobility equivalent diameter*. In this way, particles with a smaller electrical mobility precipitate in the column and the ones with larger mobility exit the DMA together with the sheath air as excess air at the bottom [11][36][15, pp. 342]. The *transfer function* describes the probability for a particle with a certain electrical mobility, to reach the exit slit of the DMA column when classifying for a certain particle size. The resolution of a DMA is thereby defined as the half-width of the transfer function. An important factor for the resolution is the absolute flow rate in the column, but also the ratio of the sheath air flow to the sample aerosol flow is crucial [36]. A typical aerosol-to-sheath flow ratio is 1:10, which leads to a resolution of about 3% of the selected classification width [15, p. 406][35].

Since the DMA classifies according to electric mobility rather than physical diameter, the particle charge state has to be controlled. Only with the charge state well known, the inversion to the particle size (electric mobility diameter) is possible. In general there are *unipolar chargers*, that create particles with same polarity (positive or negative), and *bipolar diffusion chargers*. The latter evenly charges the particles positive and negative, thereby being misleadingly referred to as *aerosol neutralizer*[8]. In modern devices soft-X-ray sources are used to create ions, since ionization with UV-sources is strongly dependent on the particles material and radioactive sources are under regulatory restrictions [15, p. 399, 350].

In this work, the TSI 3082 is used. It features the "TSI Model 3088 Advanced Aerosol Neutralizer" which uses X-rays with excitation energies of up to 9.5 keV and the "TSI Long DMA 3081A" column, applicable for particle size classification in the range of 8 nm to 1150 nm. The DMA is also equipped with interchangeable impactor nozzles at the inlet to remove larger particles from the aerosol stream. They reduce contamination and double as pressure drop elements for the inlet flow rate measurement. As it determines the upper limit of particle size for certain flow rates, the impactor size has to be selected appropriately. The available sizes and flow rate ranges are listed in Tab. 3.1. If not stated otherwise, the impactor with 0.071 mm will be used in this work .

DMAs are often used in tandem with a CPC (see 3.1.1). Together, the instruments form a so called *Scanning Mobility Particle Sizer* (SMPS). The DMA scans over

[8]The term became initially established, because eventually the aerosol is (approximately) overall electrically neutral.

Table 3.1.: Assortment of selectable impactor sizes for the TSI 3082 DMA and corresponding flow rate range.

flow rate / $^{l}/_{min}$	impactor size / mm
$0.1 - 0.8$	0.0457
$0.3 - 1.0$	0.0508
$0.6 - 2.1$	0.071

particle sizes by sweeping the electrode voltage, while the CPC determines the number concentration of the particles [11].

3.1.4. miniCAST soot generator

A *Combustion Aerosol Standard* (CAST), also referred to as *Standard Combustion Aerosol Generator* (SCAG), produces soot via controlled incomplete combustion in an environment low in oxygen. Figure 3.5 illustrates the function principle of the burner by Jing. In particular, this CAST soot generator is a diffusion flame generator, which means that the burner is designed in such a way, that oxygenation of the flame above a certain height is prevented, what in turn stimulates the soot formation processes. Imminent mixing with quenching gas prohibits additional combustion processes, thereby stabilizing the formed soot particles. Since the burner is capable of producing up to 10^8 particles per cubic centimeter, a dilution gas may be introduced to lower the particle number per unit volume to more moderate levels [37][38].

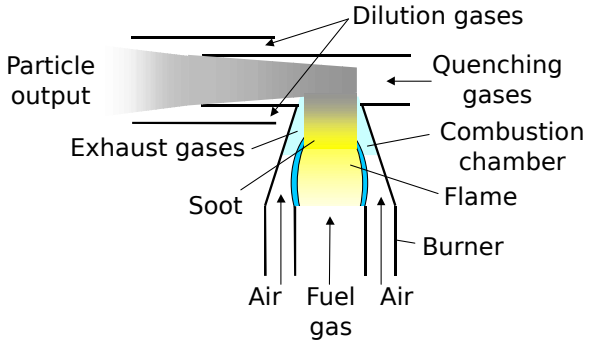

Figure 3.5.: Principle of the burner in the miniCAST soot generator[9].

In this work the "miniCAST Series 6200 Type-B Low-Mass" by Jing Ltd. is used. It produces up to 30 mg of soot per hour and was developed by Jing [38]. As the prefix suggests, the design of the burner in the miniCAST is rather compact. Fueled by high purity propane gas (C_3H_8), it produces particles in size range of 10 - 160 nm [38]. Figure 3.6 shows example particle size distributions.

[9]Figure taken from Jing, *Standard Combustion Aerosol Generator (SCAG) for Calibration Purposes* [37] and slightly modified.

Table 3.2.: Standard operation parameters for the "miniCAST Series 6200 Type-B Low-Mass" by Jing Ltd.

Supply	Volume flow
Propane, C_3H_8	$20\,^{\mathrm{ml}}/_{\mathrm{min}}$
Oxidation air	$500\,^{\mathrm{ml}}/_{\mathrm{min}}$
Dilution air	$5\,^{\mathrm{l}}/_{\mathrm{min}}$
Quench gas, N_2	$2\,^{\mathrm{l}}/_{\mathrm{min}}$
Propane dilution, N_2	off

With the standard operation parameters listed in Tab. 3.2, the mean particle diameter is expected at about 70 nm, which approximately fits the center distribution in Fig. 3.6. If not stated otherwise, the instrument is operated with the given standard parameters. Since one of the natural combustion products is H_2O, a catalytic stripper (see Sec. 3.1.2) is absolutely essential in the measurement setup later.

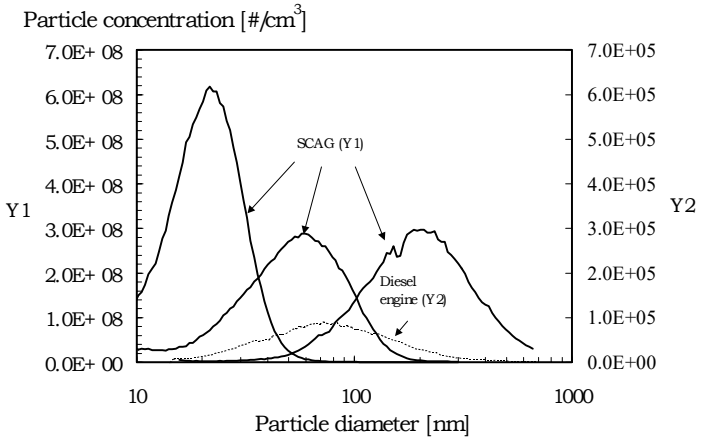

Figure 3.6.: Particle size distribution produced by a CAST soot generator[10]. The three SCAG-curves show examples of possible soot particle size distributions produced by the incomplete combustion. The miniCAST is intended to form particle distributions anywhere between the left and center curves. For comparison, the dotted line shows a typical size distribution of an older Diesel engine.

3.1.5. AVL-ADC-sensor board

The AVL-ADC-sensor board is a detector system which is capable of rapidly counting light pulses with duration down to 200 ns. It is closely related to the final detection optics counting electronics of the commercially available CPC by AVL List GmbH.

[10]Figure taken from Jing, *Standard Combustion Aerosol Generator (SCAG) for Calibration Purposes* [37].

Its hardware is based on a photo-diode and a fast sampling *analog-to-digital converter* (ADC) with a controller unit to record and store sample data. As controller a *Field Programmable Gate Array* (FPGA) is implemented. The photo-diode is a "Hamamatsu S5971", which is a silicon based "positive intrinsic negative"-type diode for frequencies of up to 100 MHz [39]. Specific data about the ADC and the FPGA is not disclosed and therefore not available, but the working principle is straight forward: The FPGA collects samples with 50 MHz and stores it. If the sampling period is over, the program recalls the data and evaluates it for peaks according to a predefined counting algorithm and stores the peak count separately. Although the sampling duration would be limited by storage capacity only, the software on the FPGA limits it to 1 s.

The counting algorithm needs to be extremely fast, what constitutes a rather simple programming. It was developed in the knowledge of a virtually noise-free signal and only features a basic coincidence correction to enhance the upper count rate and a drift correction to cover for fluctuations in laser light intensity. This also means, that fringes in the signal, especially in the rising edge, handicap the algorithm and lead to corrupted peak counts, since it triggers the coincidence correction[11]. The AVL-ADC-sensor board can be implemented with confidence only if the noise amplitude is lower than the intensity increase between two data points on the rising edge of a pulse.

Four essential values are tuneable for parametrization:

- THRHLD_PK, Peak threshold: The threshold in amplitude from which the algorithm starts to search for a peak.
- SMPL_MIN_INCR, Minimal sample increase: The minimal increase between two data points to mark it as rising edge.
- SMPL_MIN_DECR, Minimal sample decrease: The minimal decrease between two data points to mark it as falling edge and to break this instance of peak search.
- SMPL_PK_VALD, Sample peak valid: The amount of successive rising data points to accept a peak.

As software for computers, a preliminary user interface is available to either read measurement data directly (limited to 50.000 sample points, which corresponds to 1 ms sample time) and to test algorithm parameters offline or to continuously sample and count peaks within successive periods. The software stores the sampled data in regular text files for further processing.

Since this hardware and software is provided and thoroughly tested, it is highly preferable to implement it as the final counting system for the HTCPCs optical counting unit developed in this work.

[11] The other way round, the coincidence correction can be misused to skip fringes for the sake of count rate, but also instability when the fringes appear inconsistently.

3.1.6. Knife Edge Beam Profiler

Regular beam profilers based on CCD-cameras are limited to their pixel size and often their resolution is not high enough to resolve micrometer-sized features. To measure the spot size and profile of a Gaussian shaped laser beam, a *Knife Edge Beam Profiler* is a simple, yet powerful tool. In Fig. 3.7 the principle of a Knife Edge Beam Profiler is sketched. While moving a knife edge through the beam, thereby slowly covering or uncovering the laser spot, the intensity is recorded. From that, the original intensity profile is recovered mathematically.

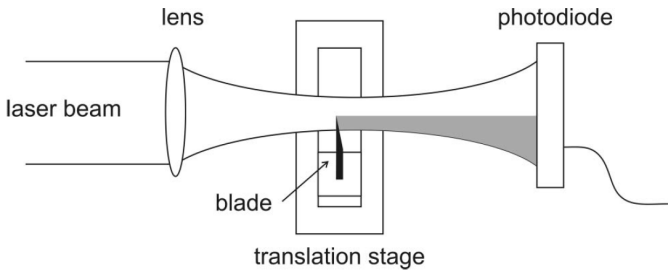

Figure 3.7.: Principle of a Knife Edge Beam Profiler[12]. A knife is moved though the laser beam and slowly covers it. The shaded area indicates the covered section of the beam.

Consider a Gaussian shaped beam like described in Sec. 2.1. First Eq. (2.1) has to be transformed to Cartesian coordinates. For a given z-position, we find

$$I(x,y) = I(0,0)A\mathrm{e}^{-2\left(\frac{(x-x_0)^2}{w(z)}\right)^2}\mathrm{e}^{-2\left(\frac{(y-y_0)^2}{w(z)}\right)^2} \tag{3.1}$$

where A is the signal Amplitude, x_0/y_0 are the beam center coordinates and σ_x/σ_x are the standard deviations.

Lets assume the beam is cut in x-direction. The power on the detector is simply the two-dimensional integral over the uncovered beam area. For the position x_k of the knife, one has to integrate the x-coordinate from x_k to $+\infty$. To solve this, the error function (erf),

$$\mathrm{erf}(x) = \frac{2}{\sqrt{\pi}}\int_0^x \mathrm{e}^{x'^2}\,\mathrm{dx'},$$

is used. Since in y-direction the full beam cross section is visible, the integral over the y-coordinate runs from $-\infty$ to $+\infty$ and is therefore trivial to solve. Integration over the Gaussian, or normal, distribution finally yields

$$I(x) = \frac{A}{2}\mathrm{erfc}\left(\frac{x-x_0}{\sqrt{2}\sigma_x}\right) + I_0 \tag{3.2}$$

[12]Figure taken from de Araújo, Silva, Lima, Pereira & De Oliveira, "Measurement of Gaussian laser beam radius using the knife-edge technique: Improvement on data analysis" [40].

where

$$\mathrm{erfc}(x) := 1 - \mathrm{erf}(x) \tag{3.3}$$

and I_0 is the baseline (or offset) that might occur during a measurement. Eq. (3.3) describes the cumulative distribution function (CDF) of a normal distribution with the very same mean x_0 and standard deviation σ_x. Thus, a measurement of $I(x)$ yields all parameters of the underlying Gaussian beam [40]. Additionally, Eq. (3.2) does not depend on σ_y. This means that this method is also valid for elliptically shaped Gaussian beams, as long as the measurement takes place along one of the principal axes.

The Knife Edge Beam Profiler employed here features a razor blade mounted on a spring-driven retracting stage. A computer controlled linear actuator, in this case "Newport CONEX-LTA-HS High Speed Motorized Actuator", moves the stage. This linear actuator features an origin repeatability of ±2.0 µm, a guaranteed uni-directional repeatability of ±0.25 µm and a guaranteed bi-directional repeatability of ±1.0 µm. The minimum incremental motion is listed with 0.10 µm with an encoder resolution of 0.03539317 µm [41]. The varying origin is of no concern for this method, since the beam center is just a parameter in Eq. (3.2). The step size is the limiting factor for the resolution of this method. Considering the actuators parameters and the spring-driven mechanics, the preferred operation mode is to push the blade trolley across the beam rather than retracting the linear actuator.

Due to its large sensor area of 8.77 mm x 6.6 mm the "Thorlabs CCD Camera Beam Profiler BC106N-VIS/M" is utilized as detector with the total irradiance as measurement value[13]. A large detector area is preferable to catch diffraction effects that occur at the blade [40]. A simple "Matlab" script controls the stage movement and power readout[14]. A fit of Eq. (3.2) to the measurement data yields the standard deviation σ in the particular direction, in which the measurement was performed. It translates to the traditional $1/e^2$ beam width parameter simply like

$$2w = 4\sigma$$

and with Eq. (2.7) to FWHM like

$$\mathrm{FWHM} = 2\sigma\sqrt{2\ln(2)}.$$

[13] A second advantage is that the adjustment is very simple, since the position of the laser spot is visible in the camera software.

[14] The "Matlab" class used to address the linear actuator was written by Thaler [42] during his master thesis.

3.2. High Temperature Condensation Particle Counter - HT-CPC

In 2012 Rongchai & Collings [18] proposed a *High Temperature Condensation Particle Counter* with the idea to operate the condenser at such high temperatures, that volatile components of the sample aerosol remain in the gas phase, very much like in an evaporation tube. The temperature has to be above 180°C to do so. They proved their concept back in 2014 with a variety of working fluids [19], although they never reported long term stability.

The HTCPC, or to be precise, the high temperature particle nucleus magnifier, in this work was developed by Kupper, Kraft, Bergmann & Boies [20]. It employs a very similar concept, but with a different working fluid: Eicosane. It is an acyclic alkane composed of 20 carbon atoms in a straight chain with a melting point of 36.48°C [43]. The proof of principle of this HTCPC was already presented in the master thesis of Kügler [21].

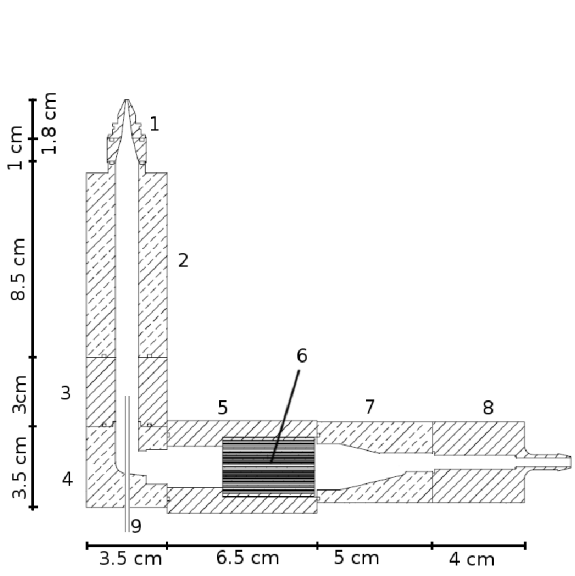

(a) Basic concept showing the direct inlet[15]

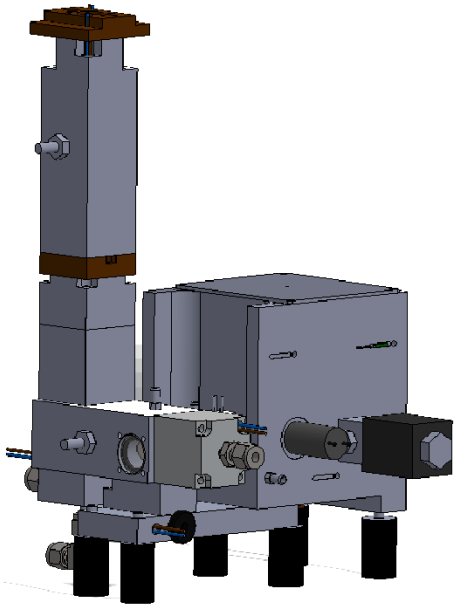

(b) 3D-rendering including base and tank[16]

Figure 3.8.: Principle and illustration of the HTCPC. (a) (1) ejecting nozzle, (2) conductive cooling-type condenser section, (3) insulation (PEEK), (4) elbow, (5) main saturator section, (6) wick for saturation, (7) saturator inlet, (8) aerosol inlet, (9) capillary for particle injection. (b) 3D-rendering of the HTCPC including the base plate and working fluid tank. On top, the thermal insulation made from "Vespel®" connector plate for the high temperature optics is visible.

Figure 3.8(a) shows the basic concept of the HTCPC. It is a conductive cooling type CPC where the particles, that serve as condensation nuclei, are injected directly into the condenser (="mixing type CPC"). In Figure 3.9 the flow schematics to operate this instrument is presented. The setup is designed for low-pressure operation. In total, 1 l/min is flowing trough the nozzle on top, limited by a critical orifice. The saturator is thereby suction-fed with nitrogen gas to prevent degradation of the working fluid. Mixing type CPCs have an inherent dilution of the sample aerosol, since the particle flow is combined with the carrier gas coming from the saturator. In this case, the capillary is designed for a dilution of 1:10. Because the flow through the capillary is rather low, a second pump transports the desired aerosol past the inlet in order to increase response time and to decrease particle loss in tubing with higher flow rates.

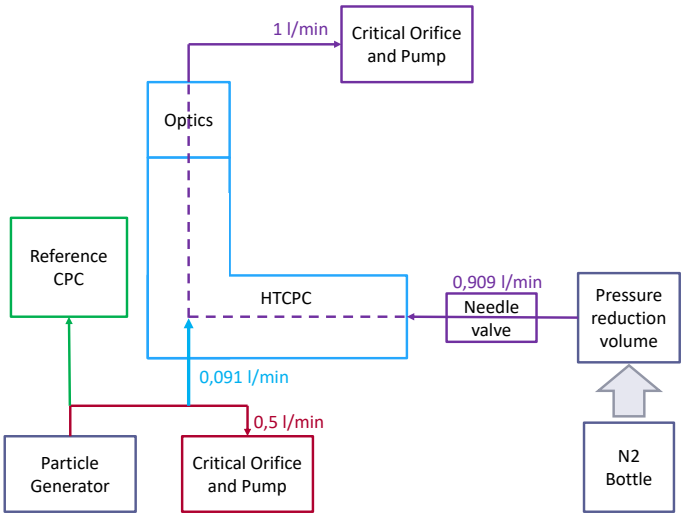

Figure 3.9.: Flow diagram of the operation of the HTCPC[17].

The standard operation conditions are 200°C for the saturator, 180°C for the condenser and 215°C for the optics. With a temperature difference of 20°C between saturator and condenser, the Kelvin diameter is expected to be somewhere around or below 40 nm. Lower values are expected when the saturator temperature is increased, which is why the optics has to withstand up to 235°C. The condenser temperature may not be reduced, because then the sole purpose to build a HTCPC would not be fulfilled.

However, the last major element of the HTCPC is still missing: The high temperature optics for particle counting. Therefore, the main topic of this master thesis is to investigate the current system and possibly develop a new prototype with enhanced optics for high temperature operation.

[15]Figure taken from Kupper, Kraft, Bergmann & Boies, "High-Temperature Condensation Particle Counter Using a Systematically Selected Dedicated Working Fluid" [20].
[16]Figure taken with permission from internal review documents.
[17]Figure taken with permission from internal review documents.

4. Prototype I: Optics with fixed lens setup

This first optics module for the HTCPC serves as the starting point of this thesis. In this chapter, the development from the principle design, investigation of internal and external components and operation on the conventional CPC up to the first application with the actual HTCPC is discussed.

Originally this prototype was developed by Martin Kupper as a simple solution to perform the verification process of the L-Type HTCPC [44][20]. This module proved to be a good engineering sample from which the prototype III in Sec. 6 was eventually derived from.

The idea behind this detection module is rather simple, as depicted in Fig. 4.1. The particles are transported through a nozzle within a gaseous stream (aerosol). A sheet of laser light is placed right above the nozzle, such that the particles pass it un-dispersed and one by one. Light scattered from the particles is then collected and imaged onto a photo diode. A key point for this concept to work properly is, that the particles travel through a very thin sheet of laser light (about 10 - 20 µm) to generate pulses as short as possible. Short pulses in turn cause less coincidence and thus allow for higher maximum count rates.

4.1. General design aspects

Since the optical system around the nozzle needs to withstand temperatures up to 230°C to be operable on the HTCPC, all electrical elements, such as laser and detector, must not be too close to this heated region. Therefore, an external, well collimated laser is a key complementary component for this prototype. In this setup a Thorlabs "CPS635" with a wavelength of 635 nm is used. It is focused above the nozzle that ejects the particles, using a plano-convex cylinder lens with a Back-Focal-Length of 12.5 mm. Figure 4.1 shows the principle in detail.

Since the particles are coming from the condenser of a CPC, we can expect them to be in the range from 2 µm up to 15 µm [15, p. 383]. Scattering visible light from particles this size means that Mie Theory (see Sec. 2.2) is valid.

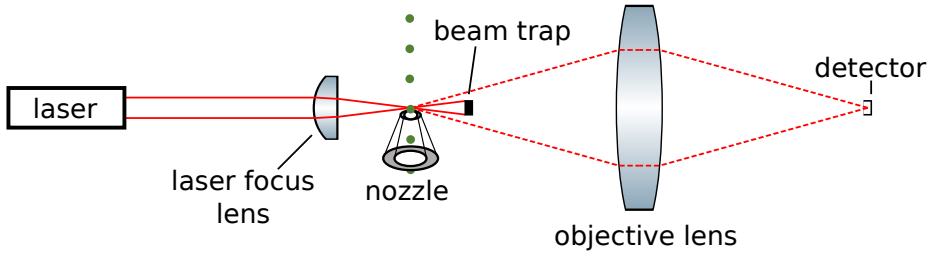

Figure 4.1.: General optical principle of prototype I. A well collimated laser is focused above a nozzle, using a plano-convex cylinder lens. This nozzle ejects the particles to be detected (ideally) one by one. Laser light hitting a particle will be scattered according to Mie Theory (see sec. 2.2). These rays are imaged onto a photo diode, utilizing another lens in a so-called 2f-setup. Most of the laser light, however, will pass trough the aerosol stream without hitting any particles. Therefore a beam dump is required to not saturate the detector. Solid line: main beam outline; Dashed line: exemplary scattered light from particles.

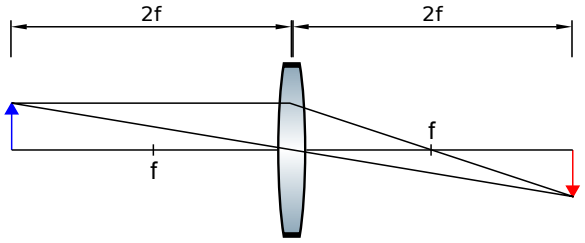

Figure 4.2.: A bi-convex lens in 2f-setup. If the object (blue, left) is two focal lengths away from the principal plane, the lens generates a 1:1 up-side-down image (red, right).

Light that passes through the particle stream without being scattered is terminated in a beam dump placed along the optical axis, while rays that do get scattered are collected by a lens in 2f-setup (sometimes also referred to as 4f-setup; see Fig. 4.2). That is a configuration, where the object is in a distance of two focal lengths from the principal plane. The nature of this 2f-setup is, that it produces a 1:1 up-side-down image of the object, which is again two focal lengths apart from the principal plane. In this case, the object is the scattering volume which is imaged onto a photo diode, where a jump in intensity will be detected, when a particle passes the laser light sheet.

Since a large numerical aperture is desired, objective lenses with a rather short focal length f of 25.4 mm are considered, where in general both a bi-convex and a plano-convex lens is possible. Particularly, Thorlabs "LB1761-ML" and "LA1951" lenses with a standard diameter of 25.4 mm (1 inch) were used. Since the lens diameter and the focal length are equal, the numerical aperture results in

$$\mathrm{NA}_{2\mathrm{f}} = n_{\mathrm{air}} \sin\left(\operatorname{atan}\left(\frac{1}{4}\right)\right) = \frac{1}{\sqrt{17}} = 0.243, \tag{4.1}$$

with $n_{\mathrm{air}} \cong 1$. This basic design considerations lead to the concept shown in Fig. 4.3. It is milled from a single block of aluminium. Further implementations are two sockets

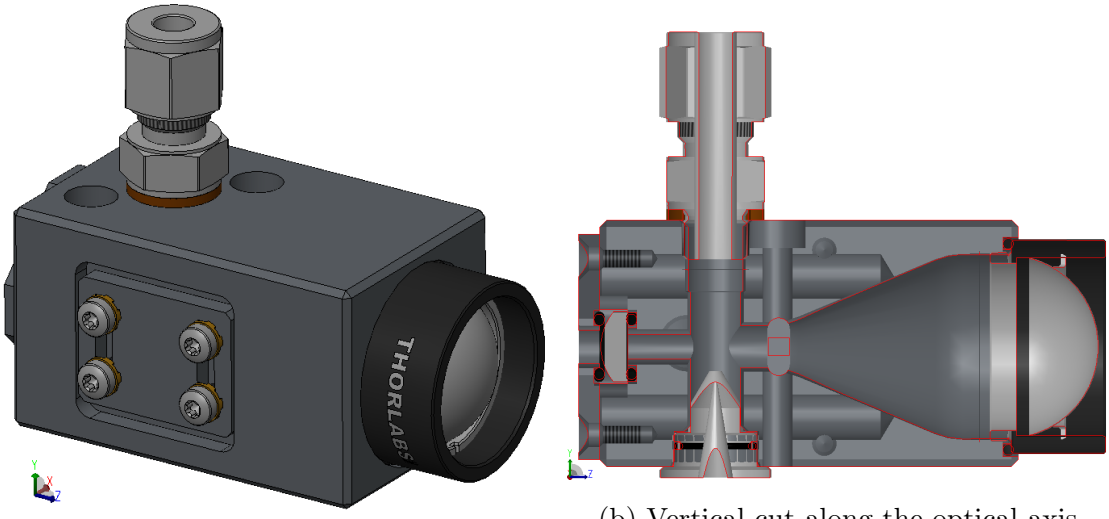

(a) Aspect view of the assembled module

(b) Vertical cut along the optical axis

Figure 4.3.: CAD drawings of prototype I. In (a) the assembled unit is depicted. At the front the objective lens is already installed, atop a connector for the aerosol pump is visible. (b) shows a cross section from top to bottom along the optical axis of this unit. On the right a plano-convex lens is installed, on the left the plano-convex cylinder lens, that creates the light sheet above the nozzle, is visible.

for 50 mm x 6.5 mm heating cartridges, a threaded M8 tap to install a temperature sensor and a slit normal to the optical axis for the option to install an internal beam trap. This beam trap may be large enough to catch the whole beam, but not too large because then the scattered light is obstructed as well.

As nozzle an existing part from a previous development is used. It is milled such that from an initial diameter of 5 mm the flow channel follows a conically tapered tubular cross-section ending with an orifice of 500 µm. Figure 4.4(a) shows a vertical cross-section of this work piece. The true diameter as manufactured is (570 ± 10) µm (see Fig. 4.4) and yields a cross section of

$$A_{\text{nozzle}} = (260 \pm 10)\ 10^{-9}\ \text{m}^2. \tag{4.2}$$

4.1.1. Theoretical capture efficiency of the 2f-configuration

With Mie-theory (discussed in Sec. 2.2), it is possible to calculate the ratio of the intensity within the angular aperture of the lens in relation to the total scattered intensity. We want to call that the capture efficiency. In Fig. 2.4, the detection cone for a 2f-setup is indicated by the black lines. Figure 4.5 shows a plot of the capture efficiency for the laser used here and particles made from Eicosane.

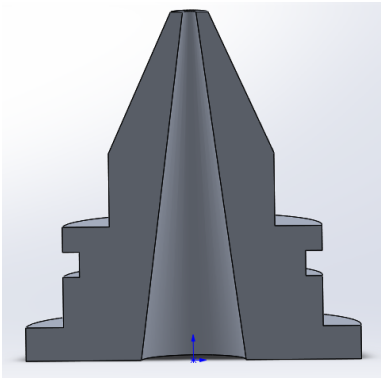

(a) CAD drawing, vertical cut

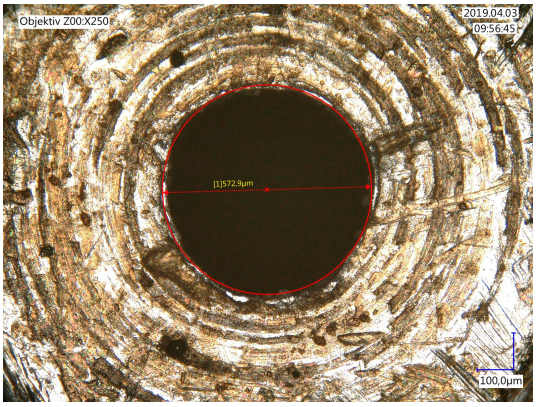

(b) Microscope image of the orifice

Figure 4.4.: The nozzle is taken over from a previous project. The drawing in (a) represents a the vertical cross section showing the conically tapered tubular channel. (b) shows the microscope image of the orifice from the milled work piece. The true diameter is measured with the microscope software and yields $d_{\text{nozzle}} = (570 \pm 10)$ µm.

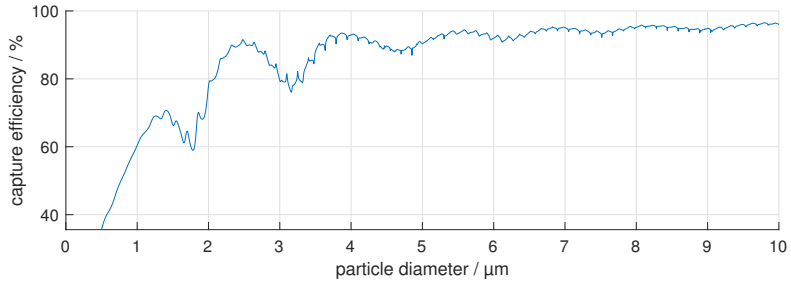

Figure 4.5.: Capture efficiency of the 2f-setup. For particle diameters starting from 500 nm up to 10 µm, the capture efficiency is calculated. The progression suggests, that particles with a diameter below the laser wavelength with a diameter of around 1.8 µm are detected least. The CPC should be operated with temperatures that guarantee larger particle diameters than 3 µm.

According to the calculation, only about 5% of the scattered light enters the detection cone of the 2f-setup, which gives further motivation to analyze and optimize this setup to have better signal yield.

4.2. Component Verification

First applications of this prototype showed neither reliable nor reproducible results. The signal was highly sensitive to misalignment of the external laser and detector, vibrations and beam trap position. Therefore, a closer look at the components of this set-up was required.

4.2.1. Laser - Thorlabs CPS635

As mentioned at the beginning of this chapter, the correct placement above the nozzle and thinness of the light sheet is essential. Any divergence of the incoming laser beam would shift the point where that beam is focused by the plano-convex cylinder lens. Since the nozzle is placed directly below the focal point, such a shift must be avoided. To investigate the collimation state of the present Thorlabs "CPS635" laser module, the CCD Camera Beam Profiler Thorlabs "BC106N" is used.

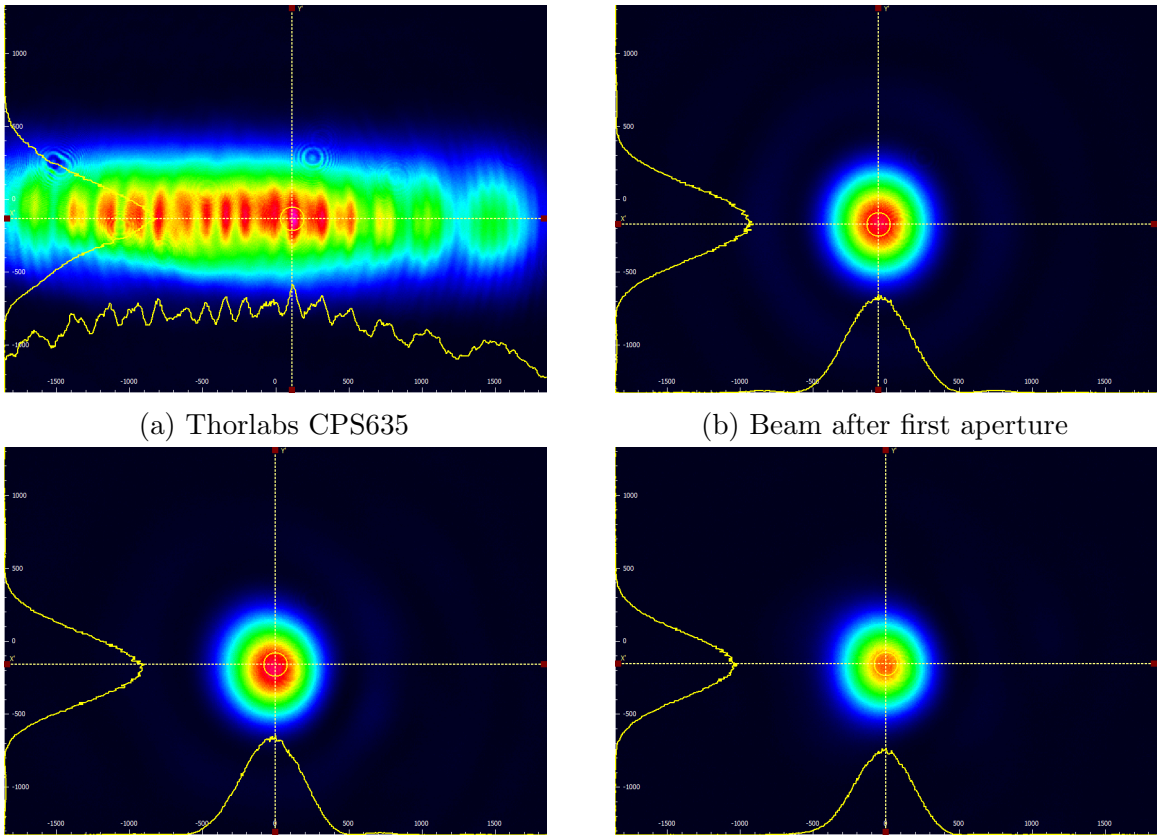

(a) Thorlabs CPS635

(b) Beam after first aperture

(c) Beam after second aperture

(d) Beam after third aperture

Figure 4.6.: Thorlabs CPS635 raw pattern and beam propagation. Setup description in sec. 4.2.1. In picture (a) the raw emission pattern of the laser is shown, where (b), (c) and (d) picture the beam shape as successively more apertures are added to clean the beam.

The speciality about the Thorlabs CPS635 is, that it produces a collimated, rather flat line of light. Up to now it was used in combination with a variable aperture to vary that line width. As shown in Fig. 4.6(a), the raw emission pattern has fringes which also move and change their shape with distance. The assumption is that the laser diode inside the module is collimated using diffractive optics. Because only one aperture was used previously, a mixture of diffraction patterns from laser and aperture were imaged above the nozzle.

As quick solution, the beam profile is now manipulated using the available means of the laboratory equipment. By introducing successively more apertures, the goal is to clean the beam from diffraction patterns before it hits the lens. A first small orifice reduces the raw light pattern to a single point source like shape (Fig. 4.6(b)). The second and third aperture (Fig. 4.6(c,d)) are used to clean the beam from the diffraction pattern generated by the first aperture.

4.2.2. Cylinder lens

After the beam is cleaned (see Sec. 4.2.1), the plano-convex cylinder lens (Thorlabs "LJ1636L1") is introduced. It produces a very thin and apparently flawless focus, that is now too thin along the direction of the particle stream for the CCD beam profiler to capture properly (fig. 4.7). Therefore, an Edge Beam Profiler (see Sec. 3.1.6) is now used, where a razor blade gradually covers (or uncovers) the beam. If we assume the beam profile to be of a Gaussian shape, an Error Function can be fitted to the resulting intensity profile to directly retrieve the FWHM and $1/e^2$ parameters.

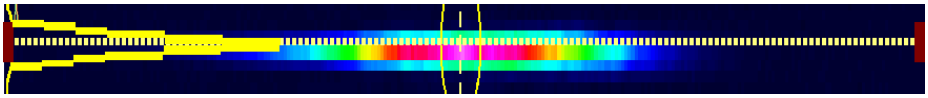

(a) Vertically zoomed view of the laser focus.

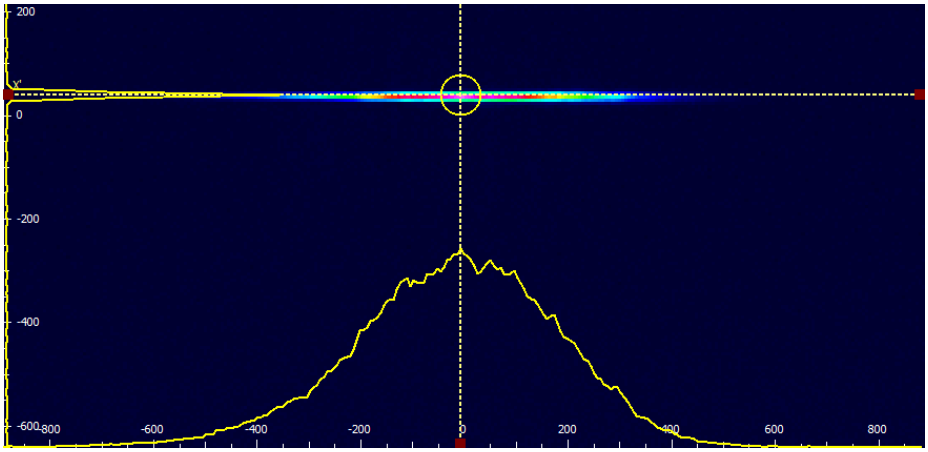

(b) Image of the CCD beam profiler in original aspect ratio

Figure 4.7.: Light sheet shape in the focus point of the plano-convex cylinder lens. (a) With only three pixels in height, the resolution of the CCD beam profiler is too low to properly capture the beam shape along the vertical axis, which is the flight direction of the particles passing the beam. To get a proper profile along that direction, a Edge Beam Profiler (see Sec. 3.1.6) has to be used. (b) The transverse beam profile is captured well and has a Gaussian shape.

If a poorly collimated laser beam is focused by a lens, the focal length does not coincide with the focus point, since the lens then images the laser source rather than

focusing plane-parallel light rays. To find the point where the laser is imaged by the plano-convex cylinder lens, and thus the optimal position regarding the nozzle, the Edge Beam Profiler is utilized to conduct measurements at various distances around the focal length (see Fig. 4.8). With the point of minimal beam width located, the distance d_{image} between razor blade and lens is measured.

$$d_{\text{image}} = (13.2 \pm 0.2)\ \text{mm}$$

That is the image distance for this plano-convex cylinder lens in combination with this particular laser in this setup and its divergence. Since the prototype was manufactured under the assumption of a perfectly collimated laser, also a BFL of 12.5 mm was assumed. In the real setup the nozzle is now too close to the lens by a margin of 0.7 mm.

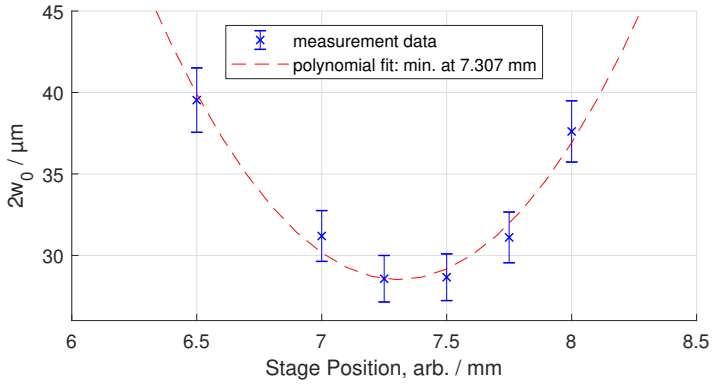

Figure 4.8.: The beam width was measured in dependence of the arbitrary stage position to find the point of minimal beam width. A polynomial fit yields the function $f(x[\mu\text{m}]) = 17.5\ \frac{\mu\text{m}}{\text{mm}^2}\, x^2 - 255.8\ \frac{\mu\text{m}}{\text{mm}}\, x + 963.0\,\mu\text{m}$ with a minimum at $x = 7.24$ mm, coefficient of determination $R^2 = 0.93$. The Error Function fit for the beam widths is processed with 95% confidence interval. The image distance d_{image} is determined by moving the stage to the optimal position and measuring the apparent BFL.

From the fit in Fig. 4.8 the measured Rayleigh range is determined to be

$$2z_r = (1640 \pm 220)\ \mu\text{m}.$$

When the lens is now approximately 700 µm to close to the nozzle, this means that the position where the droplets traverse the light sheet is at the outer border of the Rayleigh range. The missing distance is compensated later with a suitable distance plate inserted between aluminium block and lens.

Using Eq. (2.5), the divergence angle is determined to

$$\Theta_{\text{div}} = 15.3\ \text{mrad} \approx 0.9°$$

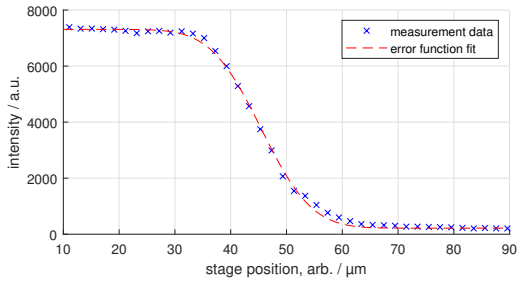

Figure 4.9.: Beam width measured at the beam waist minimum. The minimal beam FWHM is (17.0 ± 0.2) µm, which corresponds to a $1/e^2$-width of $2w_0 = (28.9 \pm 0.3)$ µm. Fit according to Eq. (3.2) yields the parameters $A = (7010 \pm 50)$ a.u., $x_0 = (3.0 \pm 0.2)$ µm, $\sigma = (7.2 \pm 0.3)$ µm and $y_0 = (200 \pm 20)$ a.u, with 95% confidence interval.

Figure 4.9 shows the Edge Beam Profiler measurement at the beam waist minimum, which results in a light sheet width of

$$s_{\mathrm{FWHM}} = (17.0 \pm 0.2)\ \mu\mathrm{m} \rightleftharpoons 2w_0 = (28.9 \pm 0.3)\ \mu\mathrm{m}.$$

This width is within the dimensions necessary to expect rather short scattering events and reasonably high count rates.

4.2.3. Beam trap

The beam trap size and position is crucial to the amount of stray light captured by the lens. If a large solid angle is covered, most of the stray light is dumped in the beam trap as well. However, if the beam trap is too small, there might be too much intensity from the main beam reaching the detector, thereby worsening SNR or even saturating it.

In the design of prototype I a port to insert a beam trap between nozzle and lens is incorporated. This element is essentially a small aluminium bar with 2 mm in height, which is inserted laterally from the side and can be shifted up and down by about ±1 mm. Figure 4.11(a) shows the internal beam trap. However, this solution poses the problem that the bar size and distance to the nozzle can not be changed easily, because the solid angle obstructed by the bar is determined in the design process. As depicted in Fig. 4.10, this internal beam trap is larger than necessary and the signal bound to the unduly covered solid angle a is lost. Further, because the beam trap has its full width horizontally all across the optical path, as visible in Fig. 4.11(a), even more signal is lost. Yet another problem is caused by stray light from the diffuse reflecting aluminium bar itself. It produces a bright background that further lowers SNR.

Due to the drawbacks mentioned above, an external beam trap is introduced. Hereby the distance to the lens, the absolute size and the material can be selected in such a

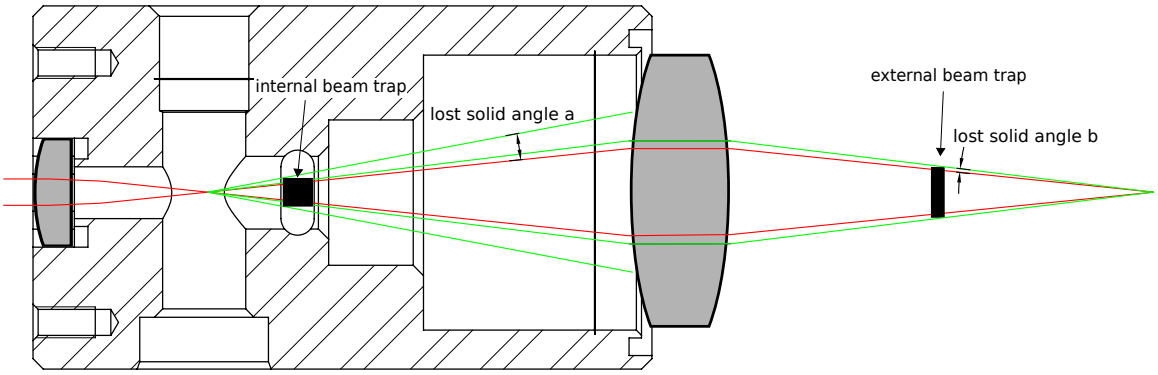

Figure 4.10.: Geometry and positions of internal and external beam trap. The internal beam trap covers a large solid angle and obstructs the signal considerably, which manifests in a lost solid angle a. An external solution enables one to change size and distance, such that losses in signal intensity are minimized, thus angle b is smallest. Red: main beam outline; Green: scattered light from particles.

way, that a maximum of scattered light from the particles is captured and stray light from the beam trap is minimized, whilst the main laser beam is annihilated entirely. In practice this beam dump is realized with a rectangular profiled, special absorbing tape ("black-out tape") suspended on a taut wire, as Fig. 4.11(b) shows. Because this wire covers only a very small solid angle, light reflection can be neglected. With this element tailored well, a minimum of signal intensity is lost due to the beam dump.

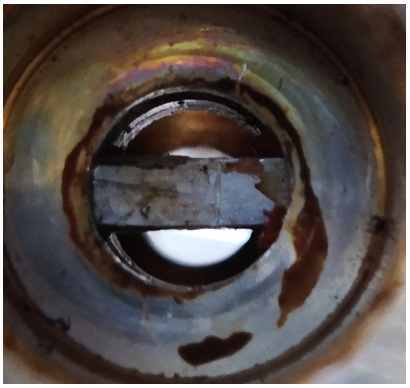

(a) Internal beam trap

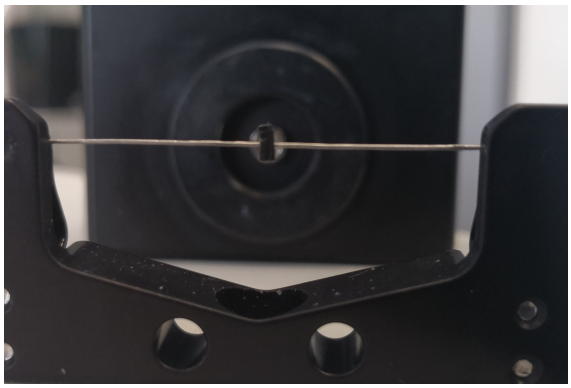

(b) External beam trap

Figure 4.11.: Internal and external beam trap of prototype I. Photo (a) shows the internal beam trap viewed from the detector's perspective. It blocks the beam across the whole horizontal width. The stains on the surface is residue from oxidized Eicosane. In Photo (b) the external beam trap viewed from the source perspective is shown. It is freely adjustable placed between the objective lens and the photo diode.

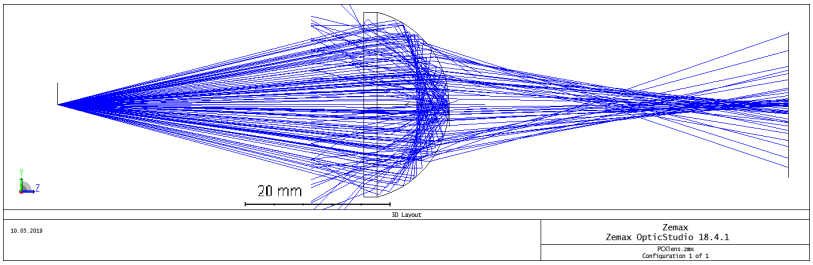

(a) plano-convex lens

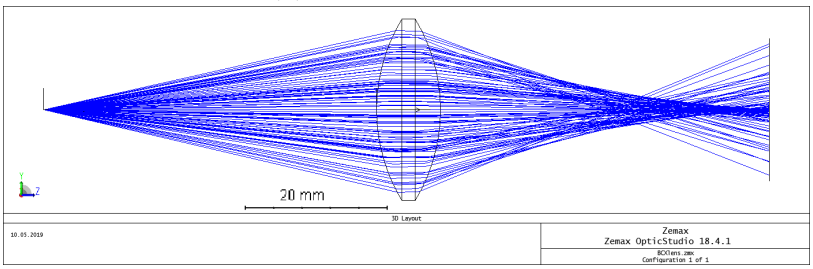

(b) bi-convex lens

Figure 4.12.: Plano-convex versus bi-convex lens in a 2f-setup. (a) shows the layout in ZEMAX for a 2f-setup with the Thorlabs "LA1951" plano-convex lens. Rays that hit the second interface with a steeper angle than θ_{crit} are not imaged to the focal point on the other side. Instead they get reflected internally twice and exit the lens the same side they entered it, causing the virtual aperture effect. In (b) the same setup with a bi-convex lens is illustrated, which does not have this issue in this configuration. The detector in the image plane is placed in the respective geometric image distances according to the 2f-setup. Light reflected from the lenses is caught by a detector plane placed $\approx 10\,\text{mm}$ in front of the lenses.

4.3. Objective lens: plano-convex versus bi-convex

The original design of this prototype involves a Thorlabs "LA1951" plano-convex lens with 25.4 mm free aperture and a focal length of 25.4 mm, that is also shown in the CAD-drawing in Fig. 4.3. However, this lens in this specific 2f-setup has a major drawback. For rays hitting the plane side of the lens in a rather steep angle, it suffers from total internal reflection on the convex side, as Fig. 4.12(a) illustrates. This is easily explained by looking at Snells law [45, p. 237]. The critical angle, when light would be refracted by an angle of $\theta_{\text{o}} = 90°$, is

$$\theta_{\text{crit}} = \arcsin\left(\frac{n_{\text{air}}}{n_{\text{N-BK7}}}\right) \approx 42°. \tag{4.3}$$

For N-BK7 the refractive index is $n_{\text{N-BK7}} = 1.516$ at 635 nm and room temperature[46], for ambient air we assume $n_{\text{air}} = 1$. Any ray hitting the interface above this angle is actually reflected internally twice, since it hits another point on the convex surface above the critical angle again. In this way, the light is reflected back out of the lens at

the same side it entered, creating a virtual aperture. In Fig. 4.12(a) the setup of the ZEMAX simulation is illustrated and shows the virtual aperture effect. Of course this gets less prominent with larger focal lengths, but in this case with the very short focal length this effect is very pronounced.

Imperative is also the amount of potentially reflected intensity. To evaluate this, in the simulation a point-like source with equally distributed emission is used, so that the energy is the same for all solid angles. The geometric data about the lenses is provided on the Thorlabs web page as ZEMAX .ZMX files. In this simulation the surfaces are simulated without anti-reflective coating. The positions of the lenses are set to the actual distance as they would be mounted in the manufactured module (see Fig. 4.10).

The simulation results in Fig. 4.13 and Fig. 4.14 yield, that the energy reflected by the virtual aperture accounts for 49.1% of the total irradiance and the energy transmitted by the lens accounts for 42.0%, the rest is absorbed. Compared to the bi-convex lens, where only 5.2% are reflected and 89.8% gets transmitted, a severe portion of signal intensity might be lost by using the plano-convex lens.

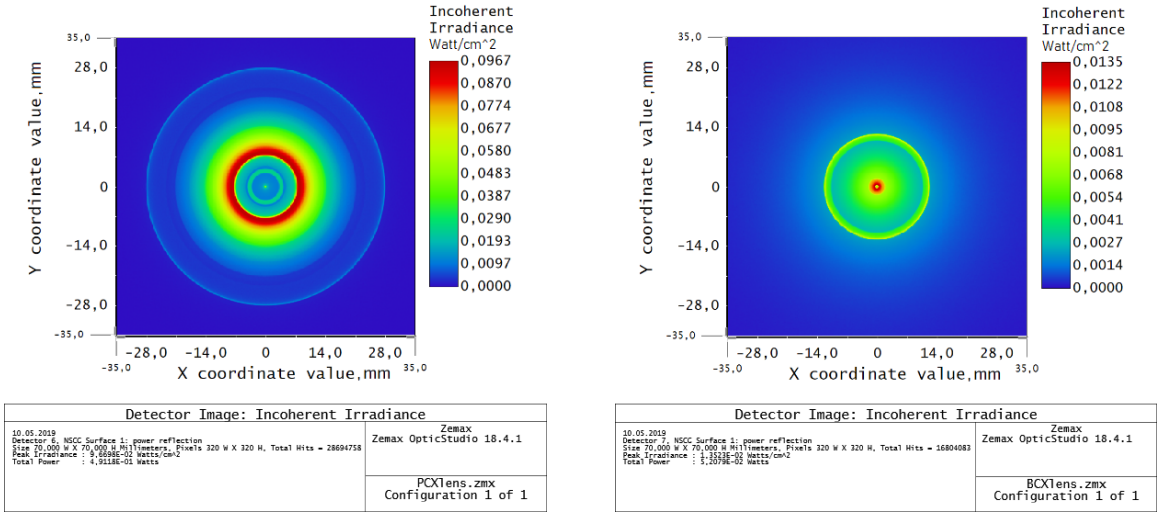

(a) Plano-convex lens (b) Bi-convex lens

Figure 4.13.: ZEMAX simulations of the light reflected back out by a plano- or bi-convex lens. (a) The virtual aperture created by the plano-convex lens is visible as the intense ring in the center. (b) Since the simulation is done without anti-reflective coating, also the bi-convex lens reflects some light. Both reflection patterns are surrounded by further reflection rings created by the respective lens edges. The geometric setups are shown in Fig. 4.12.

By replacing the plano-convex lens by a Thorlabs “LB1761-ML” bi-convex lens this

issue is resolved[1]. No rays hit an interface above the critical angle, as Fig. 4.12(b) shows. Nonetheless, both lenses are regular spherical milled ones and therefore suffer from spherical aberration, which is also clearly visible in the ZEMAX simulations in Fig. 4.14.

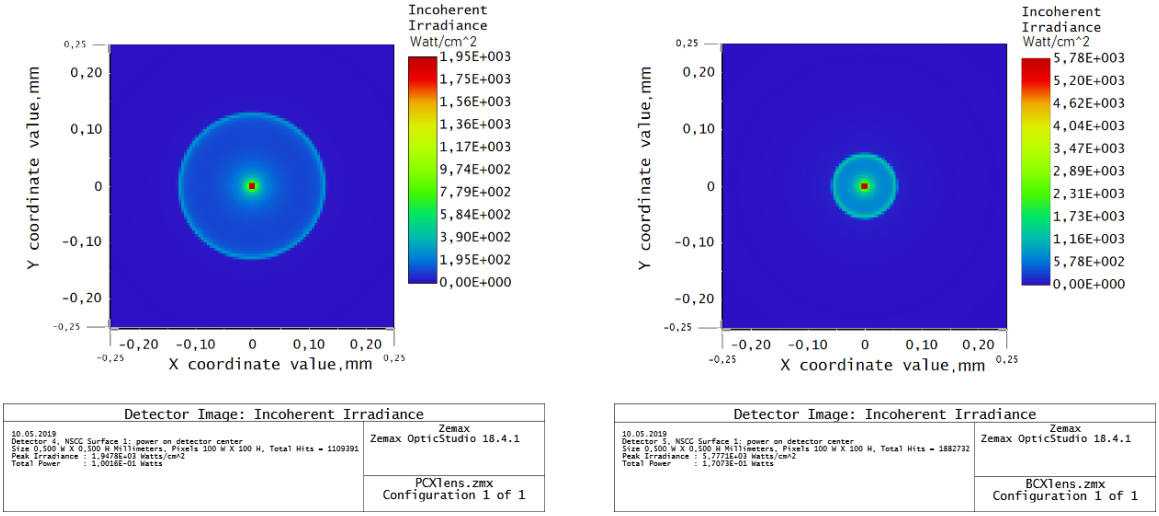

(a) Plano-convex lens (b) Bi-convex lens

Figure 4.14.: ZEMAX simulations of the light transmitted by a plano- or bi-convex lens in 2f-setup. Compared to the result of the point-like light source imaged by the plano-convex lens in (a), the image by the bi-convex lens in (b) shows a smaller over-all spot size. Since the curvature of the plano-convex lens is larger, in this setup the spherical aberration is more pronounced as well, despite the virtual aperture effect, which limits the amount of off-axis rays contributing to the image. Also here, further reflection rings are created by the lens edges. The geometric setups are shown in Fig. 4.12.

However, plano-convex lenses are usually used for collimation of laser light and point-like light sources or focusing of plane-parallel light. In those cases they reduce spherical aberration over regular bi-convex lenses [24, p 167].

4.4. Performance with a conventional CPC

With the setup and its optimized components, it is possible to quantify the temporal peak width and relative peak intensity. All measurements in this chapter are conducted with the plano-convex cylinder lens shifted by the required distance (see Sec. 4.2.2) with a spacer and the plano-convex objective lens still installed. The laboratory CPC, described in Sec. 3.1.1, is operated with the saturator at $T_{\mathrm{sat}} = 38°\mathrm{C}$ and the condenser

[1] In order to maintain the 2f-configuration this lens also features 25.4 mm free aperture and a focal length of 25.4 mm.

at $T_{\text{cond}} = 26°\text{C}$. By knowing the flow rate through the CPC, also the light sheet width can be estimated.

4.4.1. Pulse duration

To collect long samples in adequate resolution, a Thorlabs "APD120A/M" Silicon Avalanche Photo-detector in combination with a "Tektronik MDO3024" 350 MHz storage oscilloscope is used. While operating the CPC with ambient air as sample aerosol, a 10 ms long measurement is recorded with a sample frequency of 100 MHz, which in this case contains 543 pulses. Figure 4.15 shows an excerpt containing three pulses.

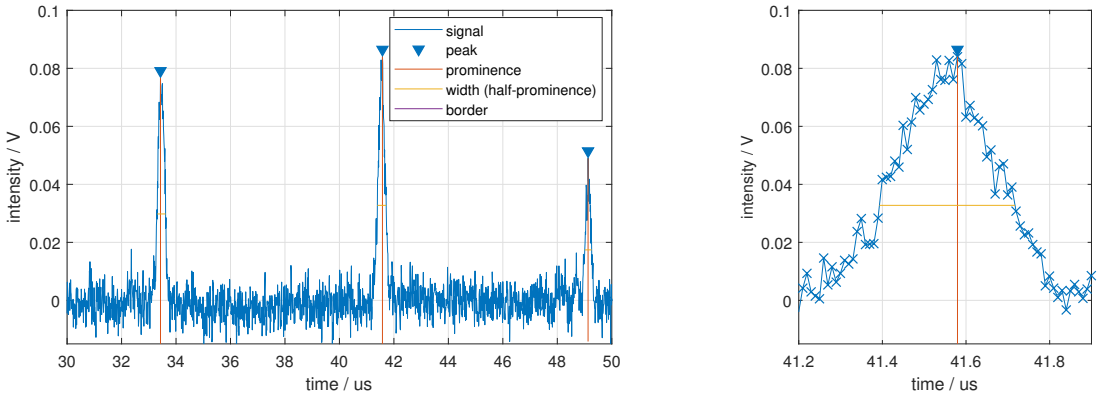

(a) Example pulses (b) Detail

Figure 4.15.: Excerpt from a particle signal from prototype I on the conventional CPC. (a) Example pulses with a FWHM of approximately 290 ns. (b) Detail on a single pulse.

Evaluation of the signal (see Fig. 4.16) yields a pulse duration of

$$t_{\text{FWHM}} = (290 \pm 40)\ \text{ns} \rightleftharpoons t_{1/e^2} = (590 \pm 70)\ \text{ns}.$$

Figure 4.15 shows an example pulse recorded with the Avalanche Photo-detector from that measurement. The flow rate Φ_{V} trough the CPC is measured with a "red-y compact" to

$$\Phi_{\text{V}} = (800 \pm 20)\ \frac{\text{cm}^3}{\text{min}}.$$

Together with the nozzle area measured in Sec. 4.1 the aerosol flow velocity can be determined, which is assumed to be equal to the particle velocity.

$$v_{flow} = \frac{\Phi_{\text{V}}}{A_{\text{nozzle}}} = (51 \pm 3)\ \frac{\text{m}}{\text{s}} \cong v_{\text{particle}} \tag{4.4}$$

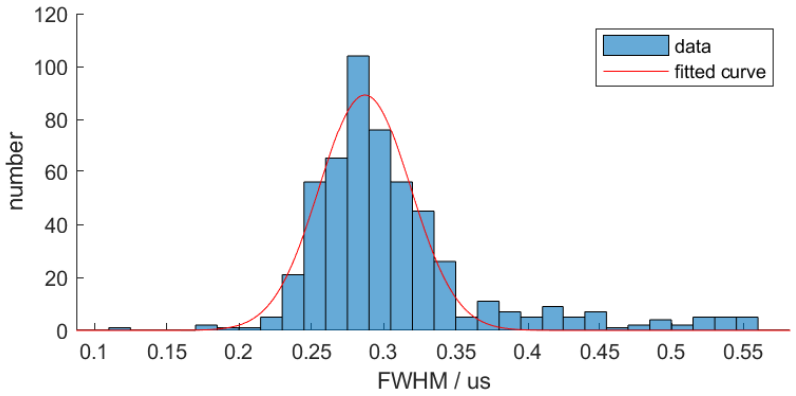

Figure 4.16.: Pulse duration distribution. The figure shows a histogram compiled from a measurement containing 543 pulses. A Gaussian distribution function is fitted to the data set to estimate the pulse FWHM in time, resulting in $t_{\mathrm{FWHM}} = (290 \pm 40)$ ns (with 1 sigma confidence interval).

With the pulse length and particle velocity and assuming that the particles are one order of magnitude smaller than the light sheet, the laser beam width is estimated to a size of

$$2w_{0,\mathrm{laser}} = v_{\mathrm{particle}}\, t_{1/e^2} = (30 \pm 5)\ \mu\mathrm{m}, \tag{4.5}$$

which agrees very well with the measurement in Fig. 4.9 ($2w_0 = (26.5 \pm 0.3)\ \mu$m).

4.4.2. Pulse height

With the same method as in Sec. 4.4.1 statistics regarding pulse amplitude I_{pulse} can be performed[2]. Figure 4.17 shows the histogram from which the average pulse amplitude

$$I_{\mathrm{pulse}} = (65 \pm 15)\ \mathrm{mV}$$

is derived. The noise on the signal is in the range of $I_{\mathrm{noise}} = (10 \pm 5)$ mV, which yields a signal-to-noise ratio of about

$$\mathrm{SNR} \approx 7.$$

Due to the counting algorithm's principle, an operation of the AVL-ADC-sensor board (see Sec. 3.1.5) with such a low SNR is not feasible. The algorithm is designed to be very fast and therefore forgoes complexity. The sole parameter to skip drops in the signal is used to reduce double counting. Consequently, it cannot handle signals with low SNR. Since there are no simple means to introduce further low-pass filters to the electronics on the AVL-ADC-sensor board, the signal needs to be of high quality instead.

[2]The pulse amplitude alone is in general not significant, but it is of interest when determining the SNR.

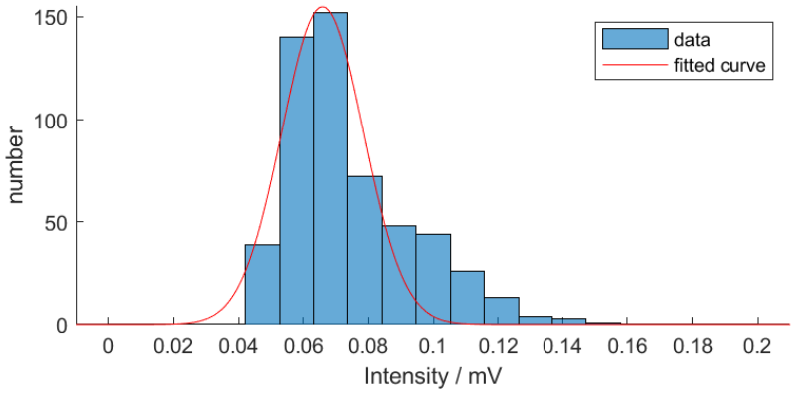

Figure 4.17.: Pulse intensity distribution. The histogram is based on the same 543 pulses contained in the measurement sample from Sec. 4.4.1. To the data set, a Gaussian distribution function is fitted to estimate the pulse intensity and standard deviation, resulting in $I_{\text{pulse}} = (65 \pm 15)\,\text{mV}$ (1 sigma confidence interval). The average noise on the detector is $\approx (10 \pm 5)\,\text{mV}$

Nonetheless, the "Tektronik MDO3024" oscilloscope provides a built-in peak recognition functionality which enables one to count also such noisy pulses contained in a just recorded sample. In this way, it is still possible to count particles per unit time with this setup. Note that the detector is connected to the oscilloscope in AC-coupling mode, consequently all DC contents, like a constant signal background caused by stray light or remnant light from the main beam, are filtered out.

4.5. Operation with HTCPC

The same optics setup as in Sec. 4.4 is now transferred to the HTCPC. In the course of this, the plano-convex objective lens is replaced by the bi-convex lens. See Sec. 4.3 for further details. Some minor changes to the laser setup had to be made as well in order to move the apertures and the laser further away from the heated chamber.

For these measurements the HTCPC is operated with the saturator at $T_{\text{sat}} = 110°\text{C}$ and the condenser at $T_{\text{cond}} = 90°\text{C}$. To begin with, the optics is carefully heated to a temperature of $T_{\text{optics}} = 120°\text{C}$.

4.5.1. Thermal induced noise

Common silicon based detectors, like the ones employed here, are sensitive up to a wavelength of $\lambda \approx 1050$ nm. Although black-body radiation at $T \approx 400$ K is rather low in the NIR, in combination with the emitting area there is well enough intensity

at wavelengths where silicon photo diodes are already sensitive, to add significant thermal background to optical measurements.

With 120°C the optics temperature is almost 100 degrees centigrade below the supposed operating temperature, but already here the signal is corrupted significantly by thermal induced noise, as illustrated in Fig. 4.18. Hardly any particle signal is noticeable in the detector signal.

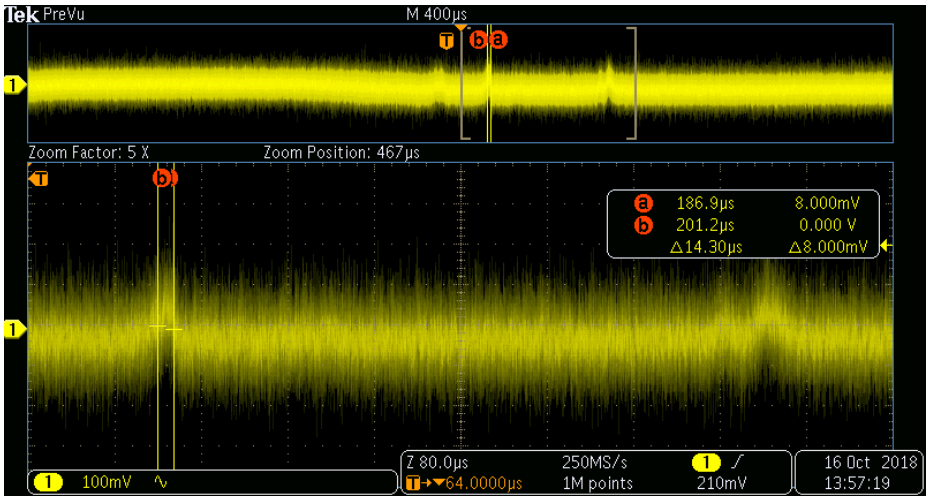

Figure 4.18.: First particle signal from prototype I on the HTCPC. The signal intensity is hardly noticeable because of the high thermally induced noise.

A quick and very effective solution for this issue is to introduce a band-pass filter in the beam path. Here a Thorlabs "FL635-10" with a center transmission wavelength (CWL) of $\lambda_{\mathrm{CWL}} = 635$ nm and a pass region width (in FWHM) of $\lambda_{\mathrm{FWHM}} = 10$ nm is used. The filter is only permeable for light within a small spectral region which is selected to be centered around the wavelength of the laser. Thereby it prevents infrared radiation emanated by the heated optical chamber from reaching the photo diode whilst preserving only the desired signal[3].

As ascertained later in Sec. 4.5.3, this not only restores the noise level to the known level from Sec. 4.4.2, but further reduces it resulting in an even better SNR, because ambient light is blocked as well[4].

[3] At a Temperature of $T \approx 400$ K the black-body radiation can be assumed to be zero in the range of the visible light spectrum. Thus, there is no thermal radiation emitted at the filter transmission wavelengths.

[4] The intensity of ambient light in the transmission region of the band-pass filter is negligible.

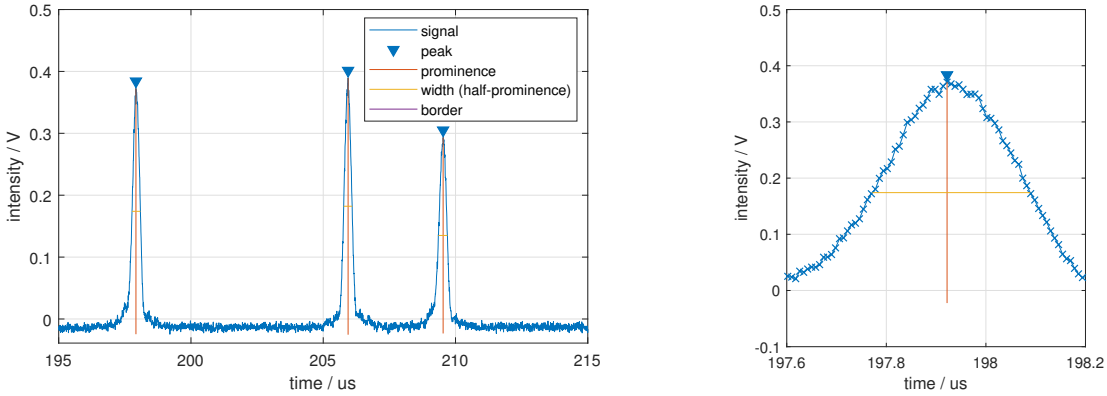

(a) Example pulses (b) Detail

Figure 4.19.: Particle signal from prototype I on the HTCPC with optical band-pass filter. (a) By incorporating the band-pass filter, the signal is significantly enhanced over the first operation, shown in Fig. 4.18. (b) The SNR is considerably higher than in Sec. 4.4.2 and the noise level within the pulse is significantly reduced to such a level, where the usage of the AVL-ADC-sensor board (see Sec. 3.1.5) can be attempted.

4.5.2. Pulse duration

Similar to the evaluation in Sec. 4.4.1, a 4 ms long sample is collected, which here contains 174 pulses. The sample aerosol is ambient air as well. The data evaluation (see Fig. 4.20) yields a pulse duration of

$$t_{\mathrm{FWHM}} = (330 \pm 20)\ \mathrm{ns} \rightleftharpoons t_{1/e^2} = (560 \pm 35)\,\mathrm{ns}. \tag{4.6}$$

For the HTCPC, the same nozzle as in Sec. 4.4 is used, where here the flow rate trough it is

$$\Phi_{\mathrm{V}} = (980 \pm 20)\ \frac{\mathrm{cm}^3}{\mathrm{min}}.$$

The aerosol flow velocity is again assumed to be equal to the particle velocity. The calculation yields

$$v_{\mathrm{flow}} = \frac{\Phi_{\mathrm{V}}}{A_{\mathrm{nozzle}}} = (64 \pm 4)\ \frac{\mathrm{m}}{\mathrm{s}} \cong v_{\mathrm{particle}}, \tag{4.7}$$

which consequently leads to the light sheet width estimation of

$$2w_{0,\mathrm{laser}} = v_{\mathrm{particle}}\ t_{1/e^2} = (36 \pm 5)\ \mu\mathrm{m}. \tag{4.8}$$

This sightly larger light sheet width suggests that moving the laser-aperture setup further away from the optics, and therefore away from the plano-convex cylinder lens, unfavourably influenced the focus. Unfortunately, this issue cannot be easily solved with this laser setup.

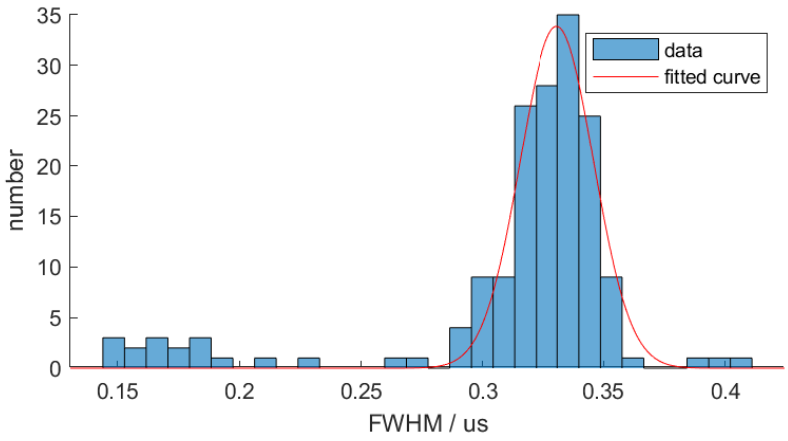

Figure 4.20.: Temporal pulse width distribution with prototype I on HTCPC. The histogram is compiled of a measurement containing 174 pulses. A Gaussian distribution function is fitted to the data to estimate the pulse FWHM in time, resulting in $t_{\mathrm{FWHM}} = (330 \pm 20)$ ns (1 sigma confidence interval).

4.5.3. Pulse intensity

With the same data set as in Sec. 4.5.2, the average pulse intensity is determined by again creating a histogram (see Fig. 4.21). The analysis yields a pulse intensity distribution of

$$I_{pulse} = (390 \pm 100)\ \mathrm{mV} \tag{4.9}$$

which is very broad, yet significantly higher in amplitude than in section Sec. 4.4.2. The noise on the signal is comparable to the one from the conventional CPC with $I_{noise} = (10 \pm 5)$ mV. With the improved signal quality however, this results in a signal-to-noise ratio of about

$$\mathrm{SNR} \approx 19.$$

This enhancement is attributed to the bi-convex lens by enhancing the signal yield and the band-pass filter that blocks infrared radiation and ambient light.

4.5.4. Testing the AVL-ADC-sensor board

Due to the previous changes, the signal on the Avalanche Photo Diode looks rather promising (Fig. 4.19). With 0.44 A/w [39], the regular photo diode is about 40 times less sensitive than the APD (17 A/w [47]), but the operation of the AVL-ADC-sensor board (see Sec. 3.1.5) seems possible nevertheless. The counting algorithm on this unit needs a virtually noise free rising edge to correctly count the scattering events. In general, as long as within the rising edge, the intensity increase from one sample point to the next is considerably larger than the noise amplitude, the algorithm can be implemented with confidence.

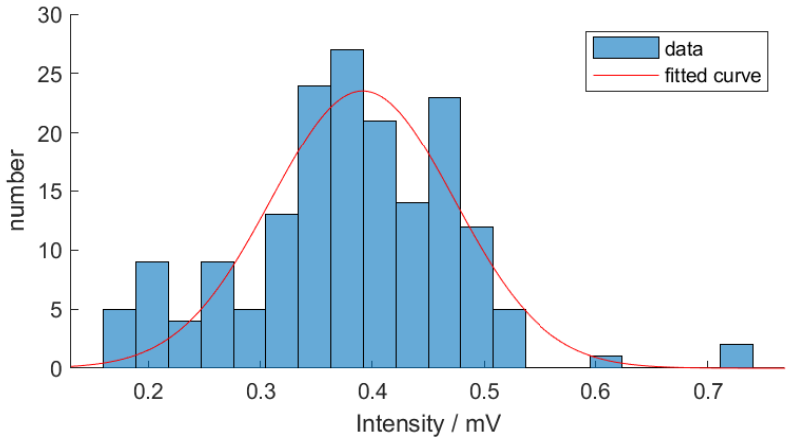

Figure 4.21.: Pulse intensity distribution. The histogram is based on the same 174 pulses contained in the measurement sample from Sec. 4.5.2. To the data set, a Gaussian distribution function is fitted to estimate the pulse intensity and standard deviation, resulting in $I_{pulse} = (390 \pm 100)$ mV (1 sigma confidence interval). The average noise on the detector is $\approx (10 \pm 5)\ mV$.

However, a readout shows that the intensity jump between two sample points in a pulse is right within the order of the noise. Figure 4.22 illustrates some example pulses. Fringes in the rising edge handicap the algorithm and lead to corrupted peak counts. An additional implemented feature of the algorithm is meant to deal with such drops, but the parametrization without an intense analysis and quite stable signal quality is not feasible[5]. Comparing this to the signal quality in Fig. 4.19, the assumption is that the photo diode is not sensitive enough to cause large signal amplitudes and that the detector might be subject to amplifier noise, that unfortunately is on the order of signal intensity[6]. Normally it is no problem to filter such noise with electronics, for example a simple low-pass filter. But because the sensor board is an integrated system and any schematics are company confidential, no additional filter could be fitted without considerable effort. Consequently, operating the AVL-ADC-sensor board together with prototype I is not possible.

4.6. Notes for further development

In the course of the investigation of this prototype, several design issues were found that have to be addressed in the development of the next counting optics.

[5]If the parametrization of this feature is deficient, the algorithm potentially recognizes more peaks than actually present in the sample, which corrupts the pulse count in an unpredictable manner.

[6]The system is developed for much larger optical signals.

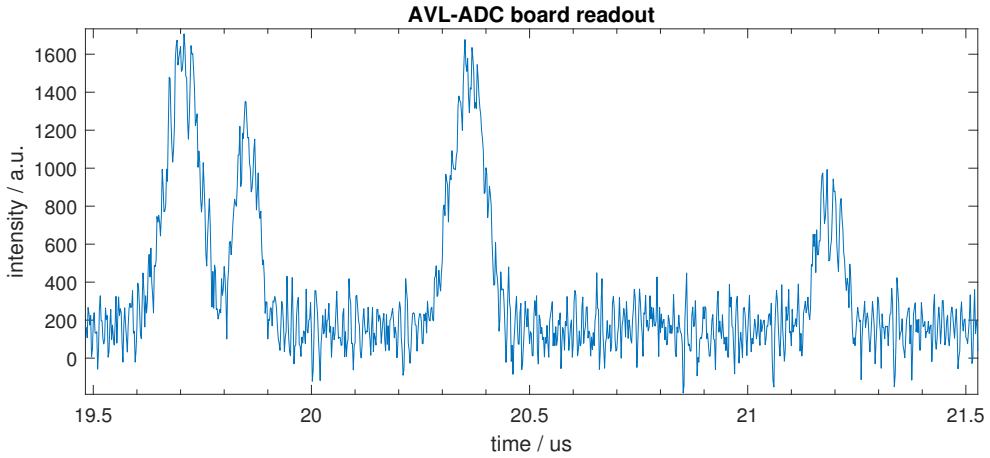

Figure 4.22.: AVL-ADC-sensor board readout with prototype I on HTCPC. The signal from scattered particles is clearly visible, but the signal quality is very poor. The counting algorithm cannot process such defective signals.

- There is no feasible way to check the focus above the nozzle. Only a passive estimation of the light sheet width via flight time is possible, to verify whether the focus with the lens separately is the same as when the lens is mounted in the chamber. As a consequence it is hard to adjust the laser in such a way, that it both traverses the chamber throughout centered and guarantee the focus lies close above the nozzle.
- A very well collimated laser is necessary to achieve the desired focus above the nozzle. The current laser is not well collimated and the diffractive optics it incorporates causes diffraction patterns in the far field. The aperture setup resolved that problem at costs of laser intensity and compactness and is therefore very unfavourable.
- The lens distance for the objective lens cannot be adjusted. There is no exact distance to the primary plane of the lens due to the sealing the mechanism (Teflon tape in combination with silicone-sealant), which causes a deviation from the 2f-setup.
- The lens in proceeding designs must be selected considering the angle of total internal reflection to avoid the virtual aperture effect.
- The internal beam trap is too large, causes plenty of stray light and cannot be adjusted very well. The solution is an external beam trap in the image plane in front of the detector. For future prototypes, this element must be modified to be sturdy and reliable.
- The AVL-ADC-sensor board is no capable of processing signals with low light intensities and it cannot be modified easily. When this unit is to be employed in future setups, the intensity of captured stray light must be much stronger and the optical SNR shall be on the order of 10^2 or higher.

5. Prototype II: Optics with elliptical mirror

As an alternative method to capture scatted light with lenses, mirrors can be used. This prototype uses an elliptical mirror to collect scattered rays and images them onto a detector or fiber. It was originally conceived as a counting optics for a conventional CPC operated at fairly low temperatures.

This unit was developed parallel to prototype I by a separate group at CTR, that in a previous iteration also tried a fiber coupled laser source as an alternative to the external laser. However, a single-mode fiber proved to be impractical, since at these high temperatures no cladding could be used and the fiber breaks under very little strain already. Therefore, a concept incorporating an external collimated laser in combination with a focus lens and apertures was pursued.

5.1. General design aspects

As illustrated in Fig. 5.1, a laser is focused above a nozzle that ejects the particles, very much like in prototype I. In order to handle high temperatures and yet an adaptable laser focus point, the unit features a port for a lens module (see Fig. 5.2) to use in tandem with an external collimated laser.

A major difference to other concepts is that the scattered light is captured with an elliptical mirror with 90° diversion angle. It has two focal points and is placed such that in one focal point there is the interaction region of the laser with the particles and in the other one there is the detector. The detector, in this case, is replaced by an optical fiber coupler to enable displacement of the photo diode to comply with the high temperatures during operation. To maximize the detector area a multi-mode fiber with 1 mm in diameter and a numerical aperture of $NA = 0.5$ is selected.

With this free laser setup, similar problems with the laser light sheet like in prototype I arise - a very well aligned and good collimated laser is necessary. A major advantage here is that the lens is adjustable in both distance and rotation, which greatly improves the variability of the light sheet above the nozzle. Nevertheless, the issue with the tedious laser source alignment remains.

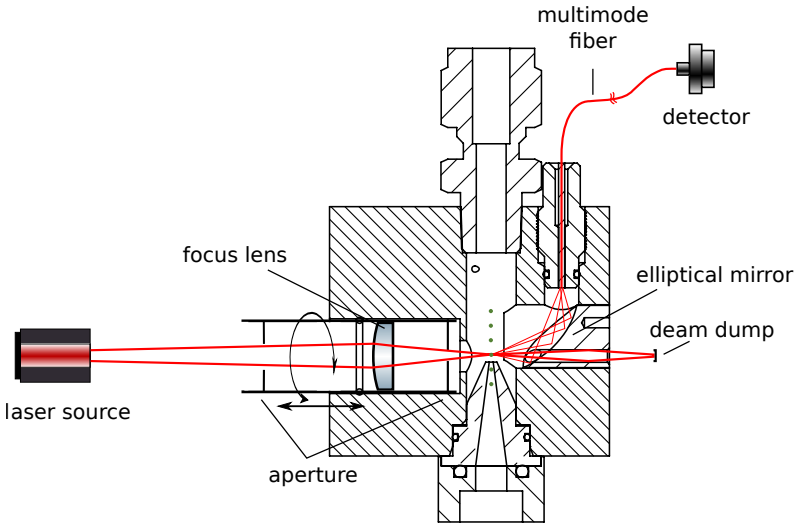

Figure 5.1.: Principle of prototype II. A laser beam is focused on the particle jet with a cylinder lens, that creates a thin sheet of light above the nozzle. An elliptical mirror is used to collect the scattered light and maps it onto a detector. The main laser beam travels on trough a hole in the mirror itself, being annihilated by a beam dump thereafter. To optimize the focus point, the module holding the lens can be adjusted by longitudinal shifting or rotation.

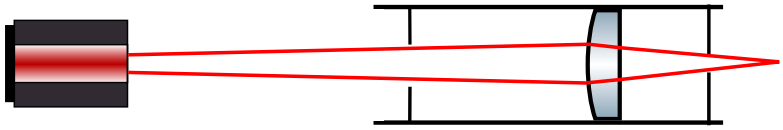

Figure 5.2.: Lens module used with prototype II. The module is a rotationally symmetric tube with 12 mm outer and 8 mm inner diameter. The first aperture is used to reduce the laser spot diameter. The second one is placed such that the diffraction pattern caused by the first aperture is captured. In the middle a cylinder lens with a focal length of 30 mm is placed.

The final layout of prototype II is presented in Fig. 5.3. The drawings also include the horn-like shaped beam dump, which is essentially a bent tube that is fully blackened out on the inside walls to efficiently annihilate the beam.

5.2. Operation with conventional CPC

To conduct measurements with the module described in the last section, the Thorlabs "APD120A/M" Silicon Avalanche Photo-detector and the "Tektronik MDO3024" 350 MHz storage oscilloscope are used again. At first, it is of interest to quantify the temporal peak width (pulse duration) and relative peak intensity (pulse height) of the signal. Like in Chapter 4, the laboratory CPC is operated with the saturator at

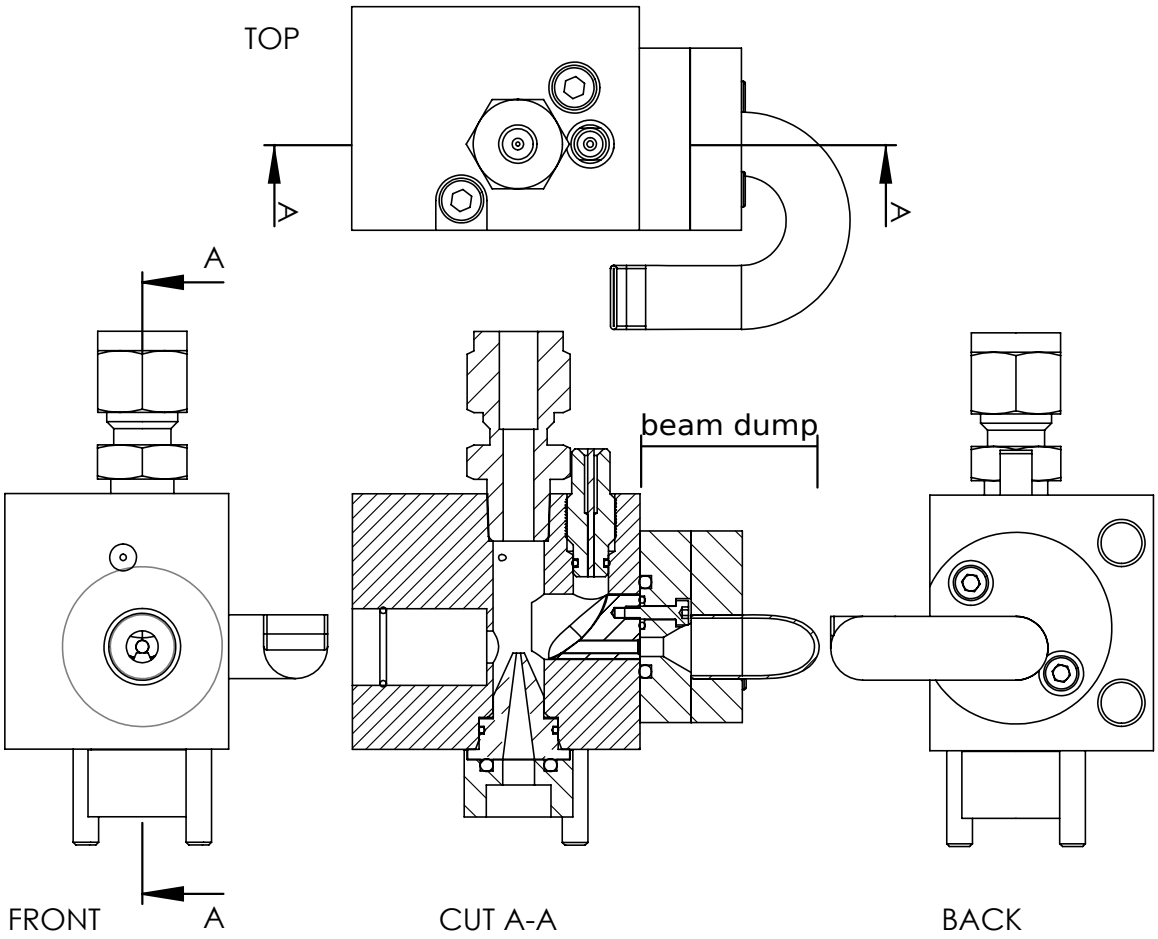

Figure 5.3.: CAD drawings of prototype II. The left drawing shows the module from the front, along the optical path. In the center, a vertical cut along the optical axis is drawn. On the right, the back side of the module is rendered, where also two holes for the heating cartridges are visible. On the top, the top view onto the module is presented, where the horn-like shape of the beam dump is visible.

$T_{\mathrm{sat}} = 38°\mathrm{C}$ and the condenser at $T_{\mathrm{cond}} = 26°\mathrm{C}$.

5.2.1. Pulse duration

With the CPC operated with ambient air as sample aerosol, a 6 ms long measurement is recorded, using a sample frequency of 100 MHz. The sample contains 126 pulses in this case. An excerpt, containing three pulses of this sample, is shown in Fig. 5.4.

Figure 5.5 shows the evaluation of the sample signal which yields a pulse duration of

$$t_{\mathrm{FWHM}} = (410 \pm 30)\ \mathrm{ns} \rightleftharpoons t_{1/e^2} = (700 \pm 50)\ \mathrm{ns}. \tag{5.1}$$

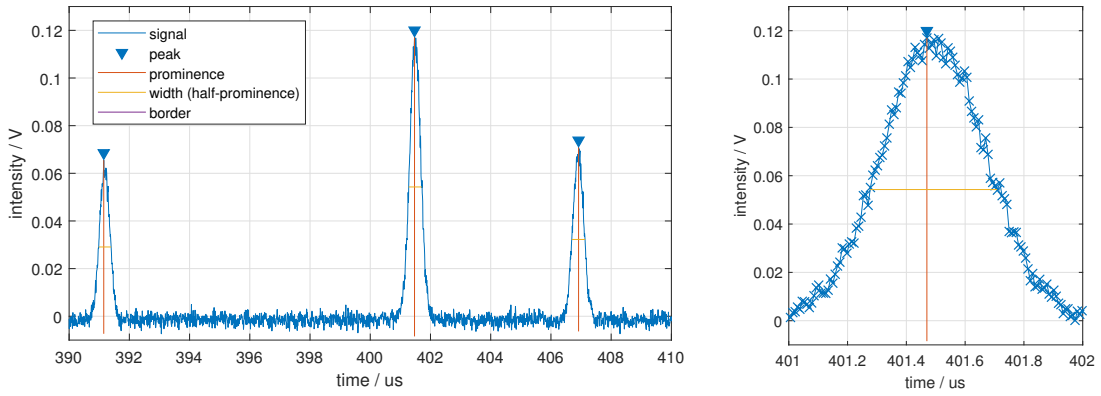

(a) Example pulses (b) Detail

Figure 5.4.: Particle signal from prototype II with the conventional CPC. (a) shows three example pulses. The signal gained looks very promising, with an SNR of ≈ 30, as calculated in Sec. 5.2.2. (b) Looking at the center pulse in detail, one can see the almost steadily rising edge and some minor fringes on the top plateau.

Since nozzle, pump and underlying CPC are the same from the last chapter, the flow rate Φ_V trough the CPC and the particle velocity v_{particle} (see Eq. (4.4)) are the same. With the pulse duration determined in Fig. 5.5, the laser beam width is estimated to a size of

$$2w_{0,\text{laser}} = v_{\text{particle}}\, t_{1/e^2} = (36 \pm 4)\ \mu\text{m}, \tag{5.2}$$

which is approximately one and a half times the size of the light sheet width determined with prototype I in Chap. 4.

The longer pulse duration (Eq. (5.1)), and thus also the larger estimation of the laser beam width (Eq. (5.2)), is most probably caused by the fact that the laser focus was not placed perfectly centered above the nozzle yet and the particles traverse the light sheet outside the Rayleigh range. A better placement was not possible before module failure, which is discussed in Sec. 5.3 later.

5.2.2. Pulse height

In order to determine the Signal-to-Noise ratio for the previously recorded sample (see Sec. 5.2.1), the mean pulse intensity is determined. The statistics are shown in Fig. 5.6 and yield a very broad distribution with a signal intensity of

$$I_{\text{pulse}} = (90\ \pm\ 40)\ \text{mV},$$

which is rather low and comparable to the results for prototype I featuring the plano-convex lens in Sec. 4.4.2. However, the noise on the detector is also very small

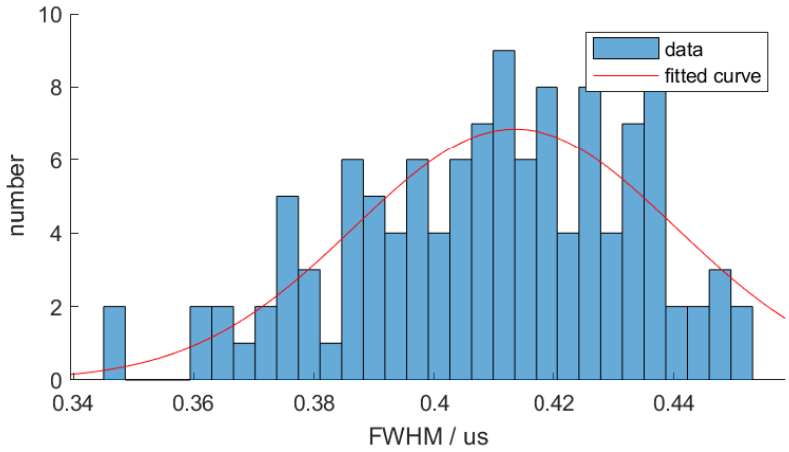

Figure 5.5.: Pulse duration distribution. The figure shows a histogram compiled from a measurement containing 126 pulses. A Gaussian distribution function is fitted to the data set to estimate the pulse FWHM in time, resulting in $t_{\mathrm{FWHM}} = (410 \pm 30)$ ns (with 1 sigma confidence interval).

with

$$I_{\mathrm{pulse}} = (3 \pm 1)\ \mathrm{mV},$$

which subsequently results in a higher SNR than in the last chapter, resulting in

$$\mathrm{SNR} \approx 30.$$

With the gained knowledge about the AVL-ADC-sensor board from chapter 4.5.4, it is clear that the signal is to low for that photo diode detector to be used here. Nevertheless, with the built in peak recognition functionality of the "Tektronik MDO3024" oscilloscope, a stable measurement is possible indeed.

5.3. High temperature operation attempt and subsequent module failure

Even tough the signal intensity is very low, the rather good SNR value is motivation enough to test this second prototype with the HTCPC. During the first test run with an optics temperature of $T_{\mathrm{optic}} = 100°\mathrm{C}$, it became clear that either the lens tube or the fiber coupler had to be adjusted, since the signal was extremely faint. After cooling down, the lens tube did not move anymore and was stuck in the prior position. No measurement data was recorded at this stage of the process yet. Any attempts to loosen the tube failed and as a result the module was rendered useless[1]. The decision

[1]The assumption is, that the lens tube deformed or buckled and consequently deadlocked in the main block.

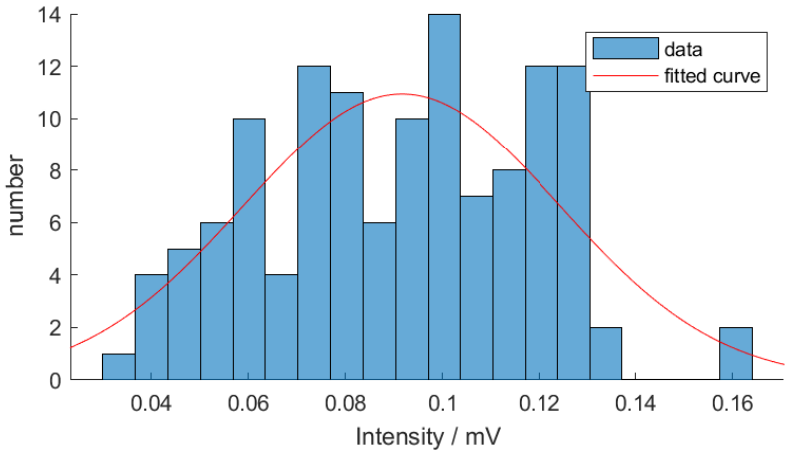

Figure 5.6.: Pulse height distribution. The figure shows a histogram compiled from a measurement containing 126 pulses. To estimate the pulse height, a Gaussian distribution function is fitted to the data, resulting in $I_{\text{pulse}} = (90 \pm 40)$ mV (with 1 sigma confidence interval). The average noise on the detector is very low with $I_{\text{pulse}} = (3 \pm 1)$ mV.

was made, to not pursue the development of this prototype. In the following section, the numerous reasons to come to this decision are discussed.

5.4. Discussion of this concept and notes for further development

Even though the signal quality looked rather promising at first (see Sec. 5.2), there were several issues with this prototype that lead to the decision, to neither pursue the development of this prototype nor the development of another optical setup that incorporates an elliptical mirror. The main reason is that there are just too many variables around the central element, the elliptical mirror. Both the stray light source and the detector element have to be adjusted almost perfectly to the two focal points of the elliptical mirror. However, the incoming laser beam has to be adjusted not only so that the focus is right in the focal point of the mirror. Simultaneously, it must also enter the channel towards the beam dump perfectly, to not cause immense stray light. Therefore, the laser must not diverge too much after the focal point to fit in the hole, which constitutes a longer focal length of the focus lens that creates the light sheet in the first place. That, on the other hand, makes it harder to create a thin sheet of light, since the beam waist radius scales linearly with the focal length of the lens, as discussed in Sec. 2.1. And last, but not least, the nozzle has to be placed such that the particles traverse the chamber exactly through the focal point and the detecting

element also has to be aligned very well[2].

The major consequence is, that a slight misalignment of the mirror, or any other component as a matter of fact, is fatal to this concept. Since the adjustments have to be made during operation conditions due to potential material expansion and deformation (for the HTCPC this means 200°C or more), this prototype proofed to be impractical at high temperatures.

The following list contains other issues with this prototype.

- The FWHM measured at first is too large for reasonable count rates, which is maybe attributable to the longer focal length of the focus lens or improper alignment. However further inspections were not possible anymore.
- Higher mechanical precision is a necessity. In this unit, the mirror is adjustable only in rotation within the mechanical tolerances of the taps and screws but not in distance, whereas the detector is only adjustable in distance. The taps to mount the mirror are not machined precisely enough to mount the mirror perfectly in its intended position. As a consequence the mirror's focal point was not in the center of the fiber coupler. Only by exploiting the large detector size (diameter of the multi-mode fibre), the signal could be captured.
- The available laser in combination with this lens tube produces a beam that is too wide to fit the channel towards the beam dump. To tackle this issue, additional apertures, held in place by threaded retaining rings, are supposed to be inserted in the lens tube. However, due to manufacturing reasons, the retaining rings cannot be screwed in far enough to secure any aperture in place.

[2]However, a large detector area leaves more room for error here.

6. Prototype III: Optics with variable lens setup

Based on the results and experience from the previous prototypes, a third optics unit has been developed. The working principle is similar to the first prototype, but with two integral changes. First, a high quality laser with integrated focus optics is used. Consequently, a plane-parallel window is used now to shine into the chamber. Second, the lens system is changed to a microscope-like setup featuring two lenses. The following sections first describe the fundamental ideas and provide reasoning for the design decisions. Later, the verification process and the high temperature operation are discussed.

6.1. Aspects in development

The experiments with prototype I underline the fact that the laser is the most sensitive part of the detection system with the highest influence on performance. Any shift of the light sheet above the nozzle moves the scattering volume, which in turn shifts the image in the detector plane. The lens system has to be designed in such a way as to capture a high amount of stray light and to reduce the effects of a shifting scattering volume to a minimum.

Figure 6.1 shows the principle of the new, third prototype for two different lens configurations. Figure 6.2 shows basic drawings of the final module. The full design drawing is given in Appendix A.1.

A high quality laser by Schäfter & Kirchhoff with integrated focusing optics is utilized to create the thin sheet of laser light. Since the chamber must be air-tight, the laser has to pass a plane-parallel window. The window is sealed with a FFKM o-ring seal and locked in place by a retaining plate. In Sec. 6.1.5 the evaluation of the new laser module is discussed and in Sec. 6.1.6 the window's influence on the beam waist is determined. The module embeds the very same nozzle known from previous prototypes (see. Figure 4.4). To map the scattered light onto the detector, the new module supports different lens configurations with freely selectable focus lengths up to 50 mm. See Sec. 6.1.1 for a discussion of the two main setups. Instead of a regular beam trap, a mirror is used here to reflect the main laser beam out of the optical path towards a

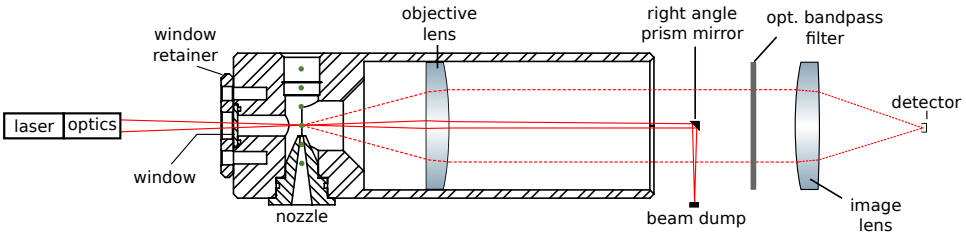

(a) Microscope-like setup

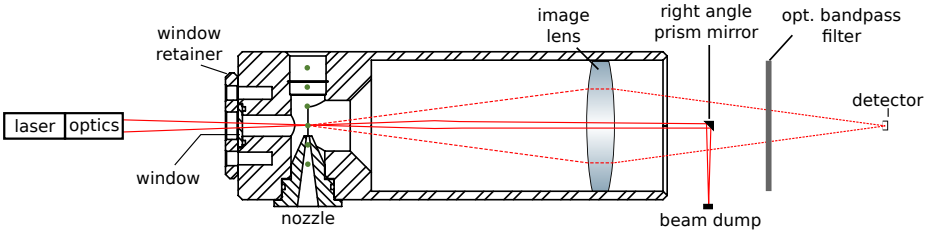

(b) 2f setup

Figure 6.1.: Principle of prototype III for two lens configurations. (a) In the microscope-like setup the objective lens collimates the scattered light and the image lens then focuses the light onto the detector. The beam trap and IR-filter are in between the lenses. (b) The 2f-setup depicted here is analog to the one of prototype I.

beam dump, as described in Sec. 6.1.9. Furthermore, a Thorlabs "FBH660-10 Premium Hard-Coated" IR-filter is employed to block black body radiation emanated by the hot chamber to reach the detector. It features a CWL of 660 nm, a pass-region FWHM of 10 nm and is rated for temperatures up to 90°C.

6.1.1. Variable lens and microscope setup

The module was designed in such way, that it can be operated with different lenses and lens combinations. The wide channel visible in Fig. 6.2(CUT A-A), starting shortly after the nozzle and extending to the right, is designed to host Thorlabs 1-inch lens tube optics without any restrictions on distance to the nozzle. Basically, any setup with an object distance of up to 50 mm could be employed.

In general, also the known 2f-setup used in prototype I could be realized again. However, it would suffer from the same problems and tedious alignment process mentioned in Sec. 4.6. Instead, the scattering center above the nozzle is imaged onto the photo-diode detector by a two-lens setup, as illustrated in Fig. 6.1(a). The principle is identical to a traditional microscope. An objective lens collimates light emanating from the scattering volume above the nozzle and an image lens focuses it onto the detector. This will not only increase the numerical aperture, it will reduce the effects of lens misalignment too.

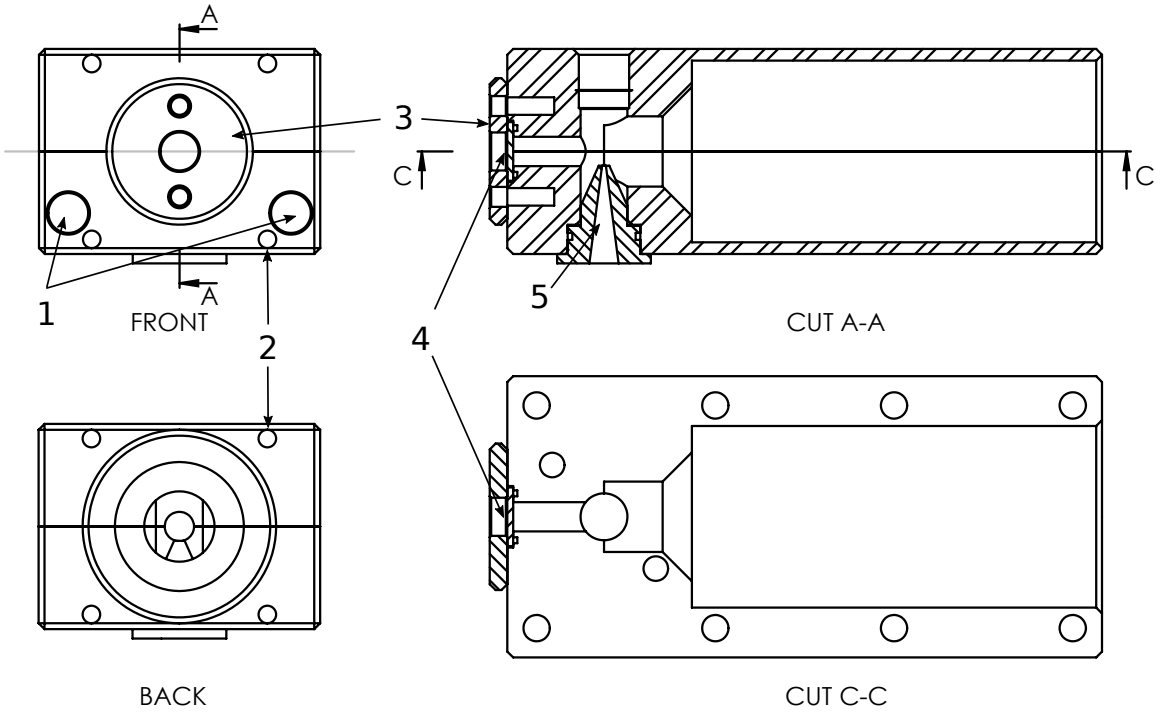

Figure 6.2.: CAD-drawings of prototype III. (1) Slots for two 50 mm x 6.5 mm heating cartridges, (2) 4-40 tap to attach a 30 mm Thorlabs cage system, (3) window retaining plate, mounted with two M3 screws, (4) window, 10 mm in diameter, 1 mm in thickness, (5) nozzle (see Figure 4.4). Not visible: M8 tap in the top half to attach the temperature sensor.

For collimation the "Thorlabs LA1951" plano-convex lens known from Chap. 4 will be reused. This lens used in the 2f-setup resulted in a NA according to Eq. (4.1) of $\mathrm{NA}_{\mathrm{2f}} = 0.243$. With the same formula, the NA for this lens in collimation configuration now yields

$$\mathrm{NA}_{\mathrm{coll}} = n_{\mathrm{air}} \sin\left(\operatorname{atan}\left(\frac{1}{2}\right)\right) = 0.447, \tag{6.1}$$

which corresponds to an increase of solid angle by 54%. Differences in signal yield correlated to the NA are discussed in the next section (Sec. 6.1.2).

The Thorlabs "LBF254-040 N-BK7 Best Form Lens" with a focal length of 40 mm is selected as image lens. For a lens diameter of 25.4 mm and a "best form" profile, this is the shortest focal length available.

In-between the two lenses light propagates parallel to the optical axis due to the collimation lens. Since the whole principle constitutes that the laser has its focal point right in the scattering volume, it is collimated by the first lens as well. This region of collimated light is the major advantage of the configuration. It is the optimal place to install the optical band pass filter, since it is indented for use with an angle of incidence of 0°. Also the beam trap (see Sec. 6.1.9) is placed there as well, since then its z-position is uncritical.

A disadvantage of this two-lens setup is that the second lens introduces further reflective surfaces and more absorption. Furthermore, the initial alignment gets more complex due to more movable parts. However, alignment can be done more easily. The influence of misalignment and the distance between the lenses is explored in Sec. 6.1.7.

6.1.2. Theoretical capture efficiency

Changing from the 2f-setup to the microscope setup is a switch from the black to the cyan colored detection cones indicated in Fig. 2.4. Figure 6.3 shows a comparison of the theoretical capture efficiencies of the 2f-setup and the microscope setup. The theoretical amount of stray light captured by the setup for a specific particle diameter is calculated by performing the integral over the scattered intensity (see Eq. (2.9)) with respect to the solid angle, guided by the setup's NA.

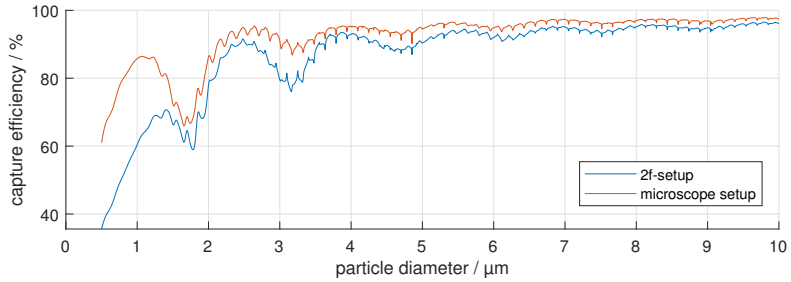

Figure 6.3.: Capture efficiency of the microscope setup in comparison to the 2f-setup. For particle diameters starting from 500 nm up to 10 µm, the theoretical capture efficiency is calculated using Mie theory. Only for smaller droplet diameters the microscope setup's capture efficiency is notably better, because for lager particle diameters the scattered intensity is then mostly in forward direction.

From the CNM droplets with diameters well above 3 µm are expected. Since for larger sphere sizes there is mostly forward scattering happening, the capture efficiency for the microscope setup is only better by a margin of 3-5%. Therefore, the main advantage of this configuration lies in the misalignment leeway, discussed later in Sec. 6.2.2.

6.1.3. Consequences of vertical laser misalignment

To achieve a stable operating range for the new prototype, it is of great interest to know the room of error in misalignment. The main influence will be a vertical drift of the scattering volume above the nozzle (laser misalignment, indicated in Figure 6.4), which in turn causes a shift of the signal at the detector.

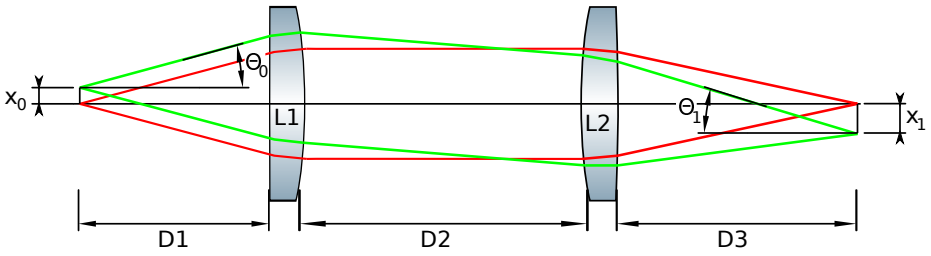

Figure 6.4.: Consequences of vertical laser misalignment. It is crucial to estimate how the focal point on the detector shifts with a vertical misalignment of the laser light sheet above the nozzle. The detector size x_1 determines the maximal permissible drift x_0 of the scattering volume. (L1) lens with focal length f_1, (L2) lens with focal length f_2, (D1)-(D3) drift spaces.

The offset x_1 depends on the initial offset x_0 and it is proportional to the ratio of the two focal lengths f_1 and f_2. However, it does not depend on the drift space between the lenses nor on the starting angle Θ_0. This has two major implications on the setup. First, the drift space D_2 may be chosen arbitrary, as long as the angle Θ_0 is not too large[1]. Second, for a detector with radius x_1 in the focal plane of L_2, the margin in misalignment of the source is simply x_0.

The active area of the "Hamamatsu S5971" photo diode on the AVL-ADC-sensor board has a diameter of 1.2 mm [39] which corresponds to $2x_1$. The focal lengths are $f_1 = 25.4$ mm and $f_2 = 40$ mm. By selecting different values for f_1 and f_2 it is obvious that a magnification is introduced, which is defined as

$$M = \frac{\text{image size } x_1}{\text{object size } x_0} = \frac{\text{image distance } b}{\text{object distance } g}.$$

With $b \equiv D3 = f_2$ and $g \equiv D1 = f_1$ one finds

$$x_0 = -\frac{f_1}{f_2} x_1 = 0.38 \text{ mm} \tag{6.2}$$

for the maximum allowed drift of the scattering volume. This is larger than any temperature dependent drift of the optics, which will be discussed in Sec. 6.1.8. From Eq. (6.2) we calculate a 1:1.57 impact of misalignment, which means a more sensitive behaviour compared to the 2f-setup. This shows the trade-off between a better imaging quality of the best form lens and the stability against lateral detector cage misalignment.

This problem may also be examined with *ray transfer matrices* (RTM). A ray starting at the focal plane of lens L_1 with an offset of x_0 and an angle of Θ_0 to the optical axis is described by the vector $\overrightarrow{X}_0$. After passing the two lenses and the three drift

[1] If starting angle Θ_0 and drift space D_2 are both large, the ray may not enter lens L_2 anymore.

spaces, it arrives at the focal plane of L_2 with an offset of x_1 and angle Θ_1, expressed with $\overrightarrow{X}_1$. Equation (6.3) shows the RTM for this case.

$$\underbrace{\begin{pmatrix} x_1 \\ \Theta_1 \end{pmatrix}}_{\overrightarrow{X}_1} = \underbrace{\begin{pmatrix} 1 & f_2 \\ 0 & 1 \end{pmatrix}}_{D_3} \underbrace{\begin{pmatrix} 1 & 0 \\ -\frac{1}{f_2} & 1 \end{pmatrix}}_{L_2} \underbrace{\begin{pmatrix} 1 & d_2 \\ 0 & 1 \end{pmatrix}}_{D_2} \underbrace{\begin{pmatrix} 1 & 0 \\ -\frac{1}{f_1} & 1 \end{pmatrix}}_{L_1} \underbrace{\begin{pmatrix} 1 & f_1 \\ 0 & 1 \end{pmatrix}}_{D_1} \underbrace{\begin{pmatrix} x_0 \\ \Theta_0 \end{pmatrix}}_{\overrightarrow{X}_0} \tag{6.3}$$

The solution for the arriving ray is

$$\overrightarrow{X}_1 = \begin{pmatrix} -\frac{f_2}{f_1} x_0 \\ \frac{\Theta_0 f_1^2 - x_0(f_1 - f_2 + d_2)}{f_1 f_2} \end{pmatrix}. \tag{6.4}$$

Rearranging the first component of $\overrightarrow{X}_1$ naturally yields Eq. (6.2) again, whereas from the second component we gain additional information. It describes the angle of incidence. The second component is not only dependent on Θ_0, the drift space length d_2 is now of significance, too. This is of importance in case detectors or filters with angular dependency are used.

6.1.4. Split chamber

The chamber is designed in such way, that it can be separated horizontally into two parts. Figure 6.5 shows a wire frame rendering of the module. With the bottom halve, stand-alone operation is possible, since it still provides the bottom connectors to attach both laser and detector cage (see Sec. 6.1.7). Without the top part it is possible to inspect the beam progression through the chamber directly. This enables precise laser and lens adjustments before the chamber is finally closed for low-pressure operation later.

The tube extending from the nozzle towards the detector enables accurate adjustment of the collimation lens, which has to be mounted in a 1-inch lens tube. Alternatively, operation in a 2f-setup (single lens) is possible. The lens tube is held in place by the compression forces created from the two halves bolted together. To ensure an air-tight chamber the lens tube must be wrapped with PTFE thread seal tape. The lens itself needs to be sealed up in the lens tube using e.g. PTFE thread seal tape or high temperature sealing compound.

While bolting the two halves together they are aligned using two dowel pins. The screws have to be tightened alternating and crosswise. After the chamber is closed, the dowel pins are removed and the window may be installed.

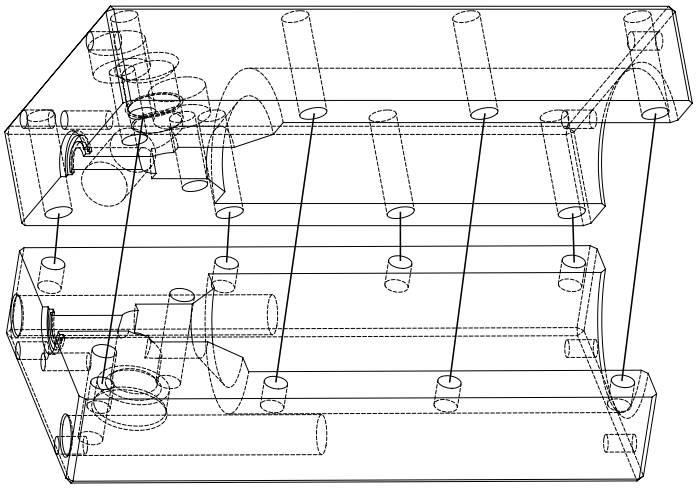

Figure 6.5.: CAD-drawings of split chamber of prototype III. For this prototype two matching halves have been machined, a bottom and a top part. If only the bottom halve is attached to the CNM, direct examination of the beam path is possible. This provides great freedom to inspect, debug and precisely adjust the whole setup, which is an integral feature of this design.

6.1.5. Schäfter & Kirchhoff Micro Line Laser

The new laser unitized for this prototype is the Schäfter & Kirchhoff (S&K) "5LT-100-2 + 55CM-660-23-M01-A8-C-6", depicted in Fig. 6.6(a). It is a combination of a very well collimated diode laser source with only non-diffractive elements, and a high quality focus optics with little lens aberration.

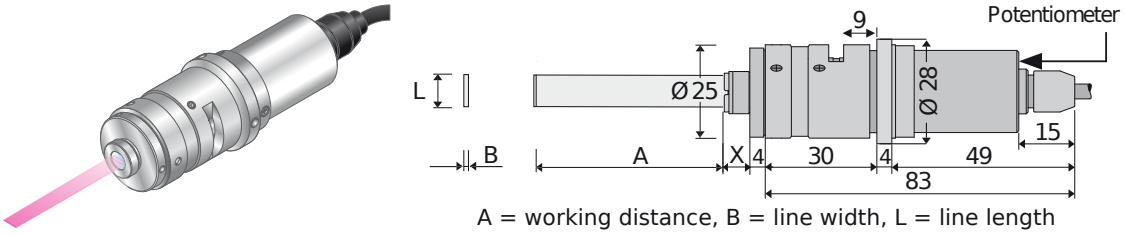

(a) Aspect rendering (b) Module dimensions in mm

Figure 6.6.: Schäfter & Kirchhoff micro line laser module used in prototype III[2]. (a) Aspect rendering of the module. (b) A cross-section trough the laser module. $A = 95\,\text{mm}$, $B \equiv 2w_0 = 18\,\mu\text{m}$, $L = 2.4\,\text{mm}$. Laser output power is controlled by the potentiometer.

It has a maximum optical output power of 23 mW, which is freely adjustable from 1%-100%. Figure 6.6(b) shows the laser module dimensions. With a wavelength of 660 nm it achieves a Rayleigh-length[3] z_0 of 729 µm and light sheet height (or line width)

[2]Both figures taken from `https://www.sukhamburg.com/products/Laser-Modules.html` (last visited 23.05.2019), and slightly modified.

[3]See Sec. 2.1 for a description of the Rayleigh-length.

B of 18 µm in a working distance A of 95 mm. The laser line in the focal point is shown in Fig. 6.7. The line length L of 2.4 mm is large enough such that there are no concerns about missing the particle stream. On the contrary, the beam must be centered very well to avoid hitting the chamber walls in the 5 mm wide corridor between window and nozzle. With its casing in 25 mm-norm it can be fitted to the standard components of the Thorlabs cage system without considerable modifications.

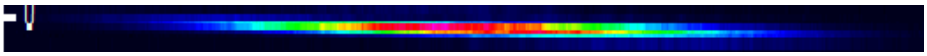

(a) Vertically zoomed view of the laser focus.

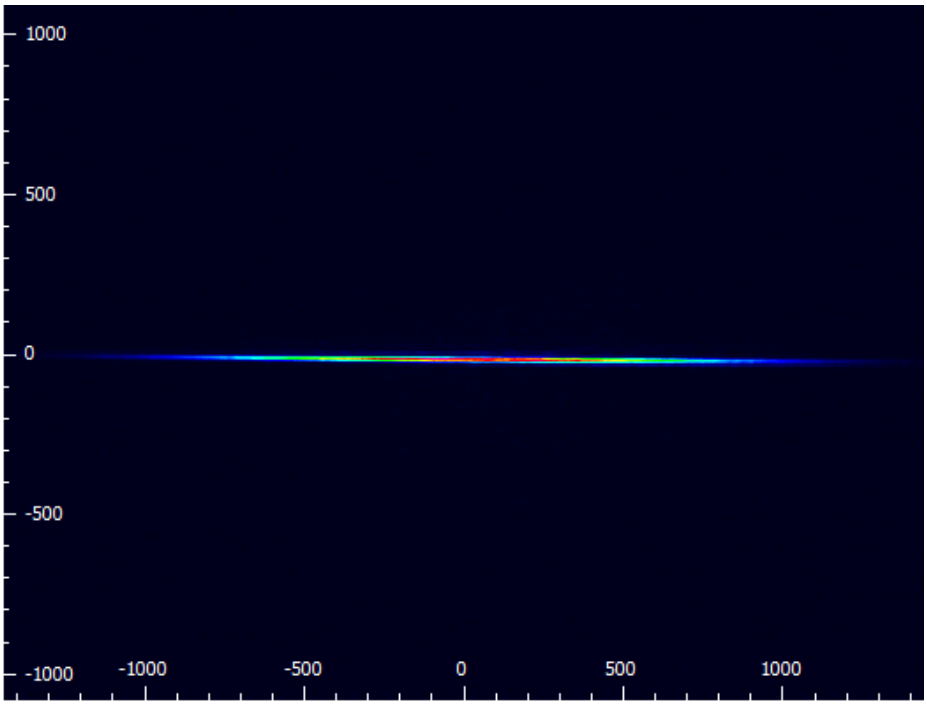

(b) Image of the CCD beam profiler in original aspect ratio.

Figure 6.7.: Schäfter & Kirchhoff laser light sheet recorded with the CCD beam profiler. (a) On the CCD the beam is just more than one pixel in height. The Edge Beam Profiler (see Sec. 3.1.6) has to be used in order to get a proper profile along the vertical direction. (b) The Gaussian shaped horizontal beam profile with 2.4 mm in width just fits the size of the CCD sensor.

Figure 6.8 shows the measurement of the laser line length L at the $1/e^2$-limit around the beam waist. The measurement as been performed with the Thorlabs "BC106N" beam profiler. The laser line length remains almost constant over the course of 4 mm with a slight divergent tendency of only 0.58 µm per mm, according to the linear regression.

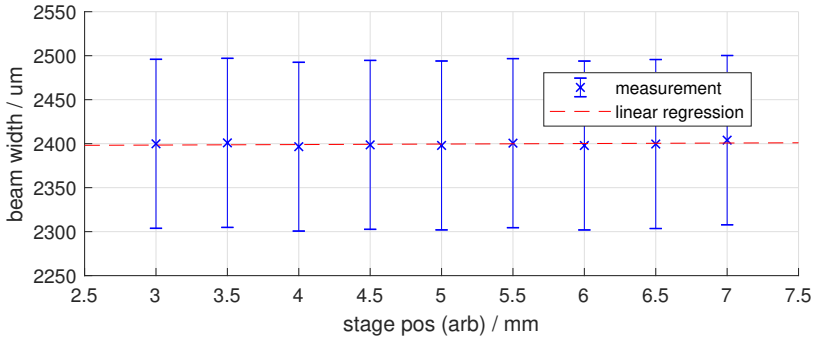

Figure 6.8.: Prototype III, Schäfter & Kirchhoff laser line length around the focal point. The line length L in µm is plotted against the stage position x in mm. The beam profiler has a coefficient of determination in beam with determination of 0.96. Fit $L = k \cdot x + d$, with $k = 0.58\,\mu m/mm$ and $d = 2397\,\mu m$.

6.1.6. Chamber window and its influence on the working distance

The optical chamber needs to be air-tight, thus the laser has to pass through a window. For this prototype, two different windows are selected:

A) Edmund optics "32947 WINDOW B270 10MM DIA CTD", MgF_2 coated B270 window
B) Edmund optics "45308 WINDOW UV 10MM DIA X 1MM TS", uncoated UV-fused silica window (UVFS)

Both windows have a diameter of 10 mm and a thickness of 1 mm. Window A is made of "B270" crown glass and features a non-standard MgF_2 *anti-reflective* (AR) coating. According to a query at the manufacturer, this coating might be able to withstand the high temperatures during operation. However, it is officially rated for 100°C only and therefore no guarantee is attributed by the vendor. Nevertheless, due to the AR-coating it is the preferred window. Window B is made from UVFS and no coating was applied. It serves as a backup-window in case window A fails.

To determine the influence of the respective windows on the laser beam waist, the Edge Beam Profiler (see Sec. 3.1.6) is used. Similar to what has been done in Sec. 4.2.2, vertical beam profiles are recorded for several distances around the beam waist. Figure 6.9 shows the measurements with the windows in the beam path, placed at the respective positions where they are installed in the optics unit. Table 6.1 lists the measurement results where the beam waist parameters are compared to the measurement without window.

For window A, which features the AR-coating, the line width $2w_0$ increases by about 6% from 20.9 µm to 22.2 µm, whereas for the uncoated window B the line width increases by 10% to 23.2 µm. Without window, the working distance is $A = (95.05 \pm 0.05)$ mm. Both window A and B extend the working distance by 450 µm and 400 µm respectively,

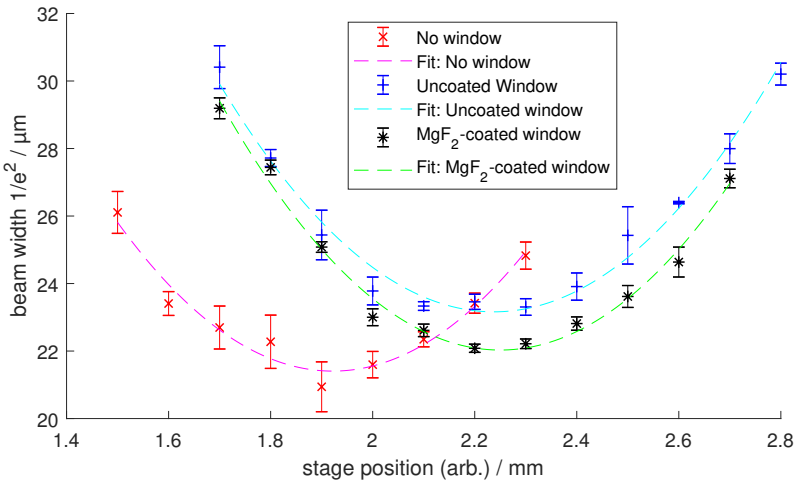

Figure 6.9.: Prototype III, laser beam waist displacement due to windows. For windows A and B and without windows, the laser beam waist at $1/e^2$-level is determined using an Edge Beam Profiler.

Table 6.1.: Influence of windows on the working distance of the S&K laser.
$2w_0$ ... light sheet width
A..... working distance
d..... window thickness
$2z_0$ .... Rayleigh range
$2z_0^{calc}$.. calculated Rayleigh range according to Eq. (2.5)

window	$2w_0$ / µm	A / mm	d / mm	$2z_0$ / µm	$2z_0^{calc}$ / µm
none	20.9 ± 0.5	95.05 ± 0.05	-	1080 ± 50	960 ± 50
A, MgF_2	22.2 ± 0.2	95.50 ± 0.05	1.15 ± 0.05	1250 ± 30	1170 ± 20
B, UVFS	23.2 ± 0.5	95.45 ± 0.05	1.35 ± 0.05	1330 ± 60	1280 ± 60

due to the longer optical paths in the window materials. This difference is attributable to the different window thicknesses and refractive indices. The laser focus shift Δz along the optical axis when going through a glass plate of thickness d and index of refraction n_2, in an environment with index of refraction n_1, is

$$\Delta z = d\left(1 - \frac{n_1}{n_2}\right). \tag{6.5}$$

For air and nitrogen we assume $n_1 \approx 1$, the indices of refraction for B270 and UVFS are $n_{\mathrm{B270}} = 1.523$ [48] and $n_{\mathrm{UVFS}} = 1.458$ [48] respectively. For the measured window thicknesses listed in Tab. 6.1, Eq. (6.5) concludes to a shift of

$$\Delta z_{\mathrm{A}} = (400 \pm 20)\,\mu\mathrm{m}$$

for window A and for window B to

$$\Delta z_{\mathrm{B}} = (420 \pm 20)\,\mu\mathrm{m},$$

which fits the measured shift very well. Also the Rayleigh range increases. From Eq. (2.5) it is known that for a certain wavelength the far-field divergence angle times the beam waist radius is a conservation quantity. Since the windows impair the beam waist the divergence angle is influenced too, which in turn causes an elongation of the Rayleigh range. Inserting Eq. (2.4) in Eq. (2.5) and solving for the Rayleigh range, we find the values in the last column of Table 6.1. The calculated values come close to the measurement data, even though Eq. (2.5) is based on the approximation of a linearized tangent.

Hereinafter, prototype III is operated with window A, unless stated otherwise. It shows advantages in beam waist quality and promises less reflections due to the MgF_2 AR-coating.

6.1.7. Cage system

The Thorlabs "30 mm Cage System" is used to directly attach both laser and detector to the optical chamber. In this way, vibrations and shocks will have least influence on the system. As depicted in Fig. 6.10, the selected components allow accurate laser adjustment to ensure an ideal placement of the focus point.

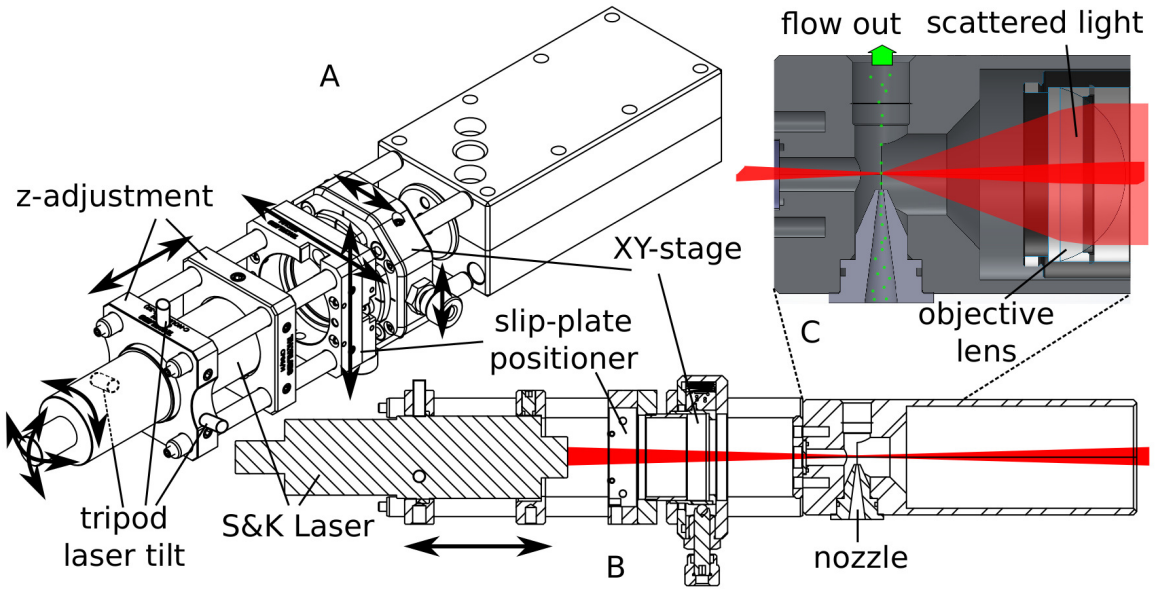

Figure 6.10.: CAD drawing of cage system on laser side. (A) Aspect view. The setup features a tripod to align the laser beam with the cage and a coarse positioner together with a fine XY-stage to allow for accurate laser adjustment. (B) Vertical cut. The z-position is adjusted by translating the laser retainer.

The laser module is retained between two CP06/M cage plates, where the rear one is modified with three screws in a 120°-arrangement. Together with the front cage

plate as pivot center, this creates a tripod for accurate laser tilting. From Sec. 6.1.6 it is known that the Rayleigh range is longer than 1 mm. Thus, no special precision mechanics is needed and it is sufficient to adjust the z-position by translating the whole laser retainer. To level out the light sheet the laser module is simply rotated inside the retainer.

After aligning the leveled laser beam with the cage using the tripod and adjusting the z-position, the slip-plate positioner "SPT1/M" is used to place the focus point roughly above the nozzle by hand-locking it in place with tightening locking screws. Finally, the "CXY1" XY-stage allows to accurately adjust the focus point above the nozzle using micrometer screws. The two XY-translation elements are connected with a short "SM1L05" lens tube, where the order in which they are placed in the cage is not of importance.

In the cage on the detector side beam trap, image lens, IR-filter and detector are mounted perfectly in line (see later in Sec. 6.3). The detector is adjustable in X-, Y-, and Z- direction.

6.1.8. Analysis of cage deformation with temperature

The alignment of laser, lenses and detector is performed in cold state on a conventional CPC. A vertical drift of the scattering volume above the nozzle is then predominately a consequence of cage deformation during the heat-up process. The difference in lengthening of upper and lower cage rods will cause the laser retainer to tilt backwards. As a consequence, the laser's focus point will move upwards and backwards, as illustrated in Fig. 6.11 with dy and dz. Backwards movement will make the pulse duration longer, since the particles traverse the beam at a different location outside the focal point. The upwards movement causes the image of the scattering volume on the detector to move downwards.

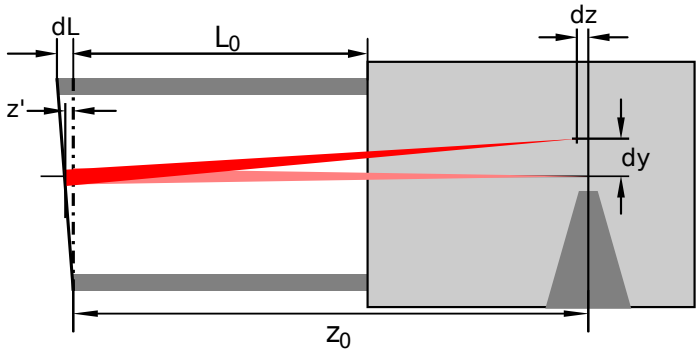

Figure 6.11.: Analysis of cage deformation with temperature. A tilt of the laser retainer by dL causes a shift of the focus point backwards by dz and upwards by dy.

A temperature difference of ΔT between the lower and upper cage rod causes a rod length difference ΔL by

$$\Delta L = L_0 \left(\mathrm{e}^{\alpha \Delta T} - 1\right)$$

with the expansion coefficient for stainless steel, $\alpha = 17.3 \cdot 10^{-6}\,\mathrm{K}^{-1}$ [30, p. 12-204]. With simple trigonometry the shift of the laser's focal point can be determined. Figure 6.12 shows the results for the utilized S&K laser along and vertical to the optical axis for a rod length of $L_0 = 50\,\mathrm{mm}$ and temperature differences of up to 50°C. However, the expected temperature difference is in the range of $10 - 20$°C during regular operation.

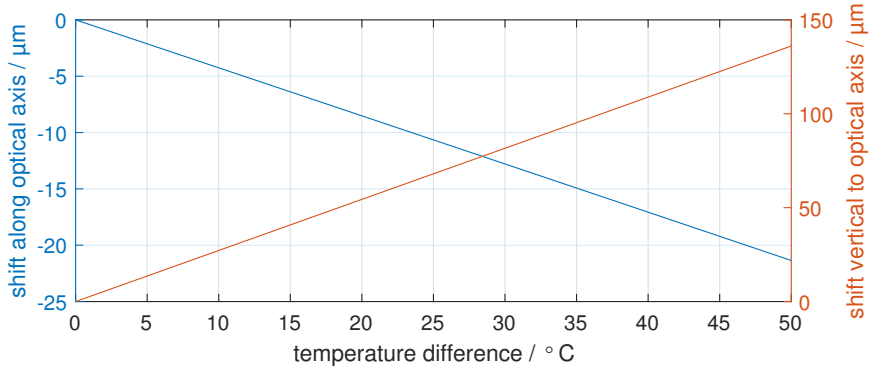

Figure 6.12.: Shift of the laser's focal point with temperature. (blue, left axis) The backwards shift of the focal point with just a few micro-meters is marginal compared to the laser's Rayleigh range of $z_0 = (1250 \pm 30)\,\mu\mathrm{m}$. (red, right axis) The vertical shift is more pronounced. For realistic temperature differences of $10 - 20$°C the scattering center will move up by about 30-50 µm.

The drift along the optical axis for a ΔT of 50°C is marginal and much smaller than the Rayleigh range of the S&K laser ($z_0 = (1250 \pm 30)\,\mu\mathrm{m}$).

From Eq. (6.2) we know that a drift up to 380 µm is still possible before losing signal on the detector. With a difference of over 50 µm at a ΔT of 20°C, the drift dy vertical to the optical axis is much larger than dz, but well within the acceptable range. Even for ΔT of 50°C only half of the acceptable misalignment tolerance is used, which also allows for a great margin in initial misalignment.

6.1.9. Beam trap: A prism mirror

As external beam trap the Thorlabs "MRA03-E02" prism mirror is selected. It is a right-angle prism with a broadband dielectric coating and a size of $L = 3.0\,\mathrm{mm}$. At the intended *angle of incidence* (AOI) of 45° it is highly reflective in the wavelength region of 400 - 750 nm, as indicated by the gray area in Fig. 6.13(a). In correspondence with the manufacturer a temperature stability to 100°C was affirmed.

The prism comes with a clear aperture (= reflecting surface area) of 70%, The surface around the edges is not defined, but acts like a diffuse reflective rim. However, since the divergence angle of the S&K-laser is rather small and the objective lens also collimates the laser beam, the active reflective area is large enough to effectively reflect the whole beam out of the cage into a beam dump, as seen in the photograph in Fig. 6.13(b).

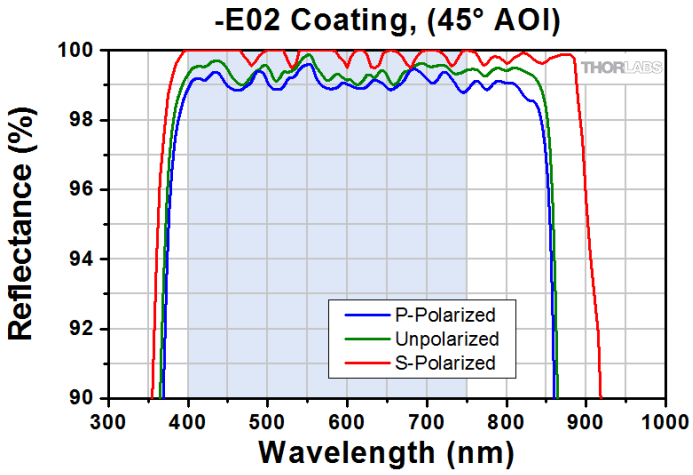

(a) Beam trap reflectance[4]

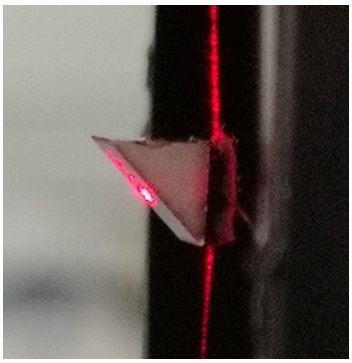

(b) Prism mirror installed in cage system

Figure 6.13.: Prism mirror beam trap. (a) The reflectance of the applied broadband dielectric coating on the Thorlabs "MRA03-E02" prism mirror. It is intended for use with an AOI of 45°. (b) A photograph of the laser spot the mirror. Above and below the suspension wires are visible, lit up by the light in the tail of the Gaussian profile well below the $1/e^2$-limit.

There have been tests using the prism mirror "MRA03-P01". It features a protected silver coating, has the same dimensions as the "MRA03-E02" and a mirror face that expands all the way to the edges. However, this one failed during high temperature operation due to degradation of the silver coating.

6.2. Configuration of the new optics module with a conventional CPC

All major components of the new module have been selected in Section 6.1 and testing of different lens configurations is now possible. The laser is installed in the cage system as described in Sec. 6.1.7 and thereby connected to the chamber. The detector side will be examined in open and closed state. Since the pulse duration is determined by the laser's Z-position, the focus is on high signal gain and quality at this point.

[4]Figure taken from `https://www.thorlabs.com/newgrouppage9.cfm?objectgroup_id=7715`, last visited 22.05.2019.

The temporal FWHM is optimised later and is expected to further boost the signal amplitude.

Like in Sec. 4.4, the laboratory CPC (see Sec. 3.1.1) is used first. It is operated with its standard parameters, saturator at $T_{\mathrm{sat}} = 38°\mathrm{C}$ and the condenser at $T_{\mathrm{cond}} = 26°\mathrm{C}$.

6.2.1. Open operation with bottom halve

The general signal yield depends on both the lens setup and beam trap position. In this section the 2f- and the microscope-like setup will be tested with the bottom halve of prototype III only. This enables to examine the laser beam closely from its origin all the way to the detector. Furthermore, without the upper halve it is easy to exchange and rearrange the lenses accordingly and no laser window is needed so far.

This open operation is only possible with the conventional CPC in over-pressure operation, where the sample aerosol is pushed through the CNM. The flow rate through the CNM is adjusted to $\Phi_{\mathrm{V}} = (1000 \pm 20)\,{}^{\mathrm{cm}^3}/_{\mathrm{min}}$ and ambient air is used as sample aerosol. Like in Chap. 4, the Thorlabs "APD120A/M" Silicon Avalanche Photo-detector is used in combination with the "Tektronik MDO3024" 350 MHz storage oscilloscope to collect data samples.

Open 2f setup

The 2f-setup has already been discussed in great detail in Chap. 4. The bi-convex lens with a focal length of 25.4 mm is used here again as central element. Off-axis light rays pass the NIR-filter with an angle. This is not beneficial for signal yield, since the filter is actually rated for an AOI of 0°.

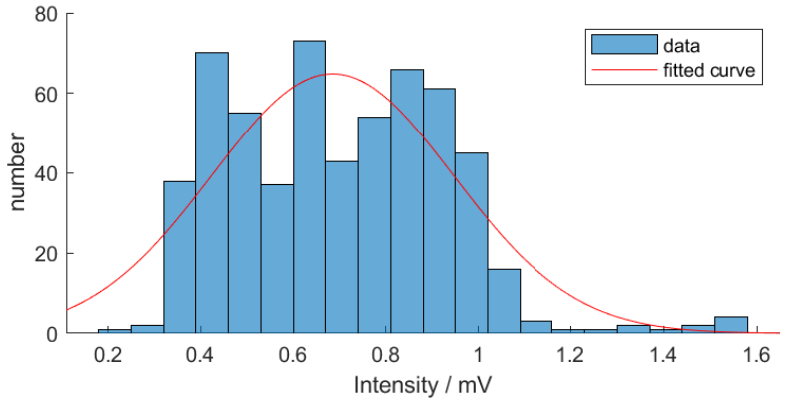

Figure 6.14.: Pulse height with prototype III in open 2f setup. The histogram is based on 575 pulses. A Gaussian distribution function fitted to the data set yields $I_{\mathrm{pulse}} = (700 \pm 300)\,\mathrm{mV}$ for the pulse height (1 sigma confidence interval).

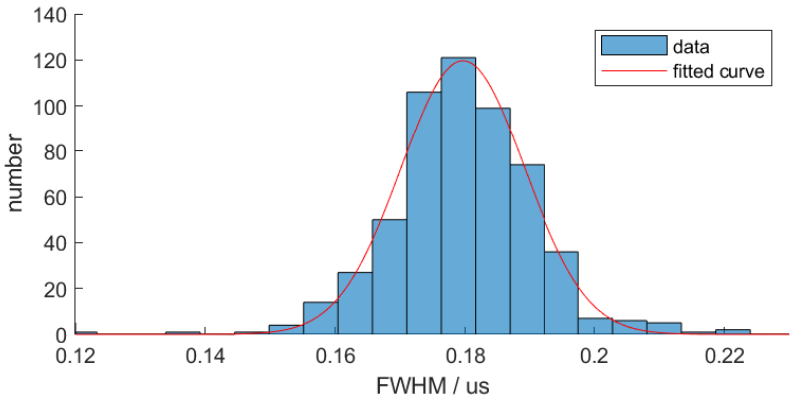

Figure 6.15.: Pulse length with prototype III in open 2f setup. The histogram is based on the same 575 pulses as Fig. 6.14. A Gaussian distribution function fitted to the data set yields $t_{\mathrm{FWHM}} = (180 \pm 15)\,\mathrm{ns}$ for the pulse duration (1 sigma confidence interval).

A 4 ms long sample containing 575 pulses yields the statistics in Fig. 6.14 and Fig. 6.15. The pulse intensity concludes to

$$I_{\mathrm{pulse}} = (700 \pm 300)\,\mathrm{mV}$$

and the pulse duration to

$$t_{\mathrm{FWHM}} = (180 \pm 15)\,\mathrm{ns} \;\rightleftharpoons\; t_{1/e^2} = (305 \pm 20)\ \mathrm{ns}.$$

With a noise amplitude of $I_{\mathrm{noise}} = (20 \pm 5)$ mV the signal quality is already very good:

$$\mathrm{SNR} \approx 35.$$

Analog to Sec. 4.4.1, the laser beam width is estimated using the signal length and the flow rate ($\Phi_{\mathrm{V}} = (1000 \pm 20)\,{}^{\mathrm{cm}^3}/_{\mathrm{min}}$). It concludes to

$$s_{\mathrm{pulse}} = (20.0 \pm 2.5)\,\mu\mathrm{m},$$

which confirms the measurement in Sec. 6.1.6 ($2w_0 = (20.9 \pm 0.5)\,\mu\mathrm{m}$).

Open microscope setup

The microscope-like setup is realised using the Thorlabs "LA1951" plano-convex lens, known from Chap. 4, as objective (or condenser) lens together with a Thorlabs "LBF254-040" best form lens as imaging lens ($f = 40\,\mathrm{mm}$). The regular plano-convex lens is selected to benefit from the higher NA it provides. Both NIR-filter and beam trap are placed between the lenses.

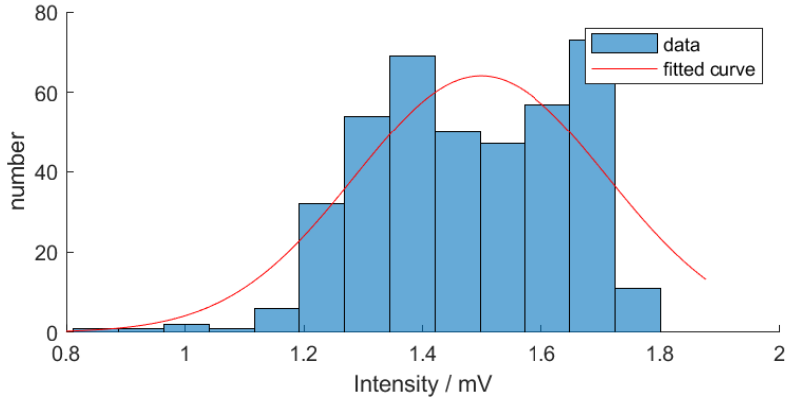

Figure 6.16.: Pulse height with prototype III in open microscope setup. The histogram is based on 409 pulses. A Gaussian distribution function fitted to the data set yields $I_{\text{pulse}} = (1500 \pm 250)\,\text{mV}$ for the pulse height (1 sigma confidence interval).

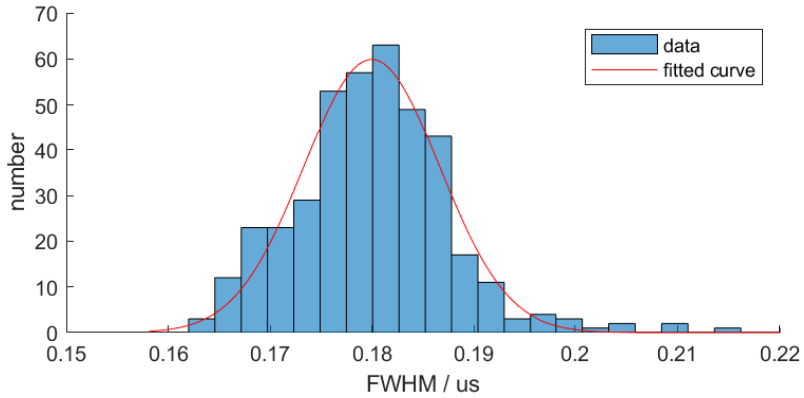

Figure 6.17.: Pulse length with prototype III in open microscope setup. The histogram is based on the same 409 pulses from Fig. 6.16. A Gaussian distribution function fitted to the data set yields $t_{\text{FWHM}} = (180 \pm 10)\,\text{ns}$ for the pulse duration (1 sigma confidence interval).

Figure 6.16 and Fig. 6.17 show statistics of a 4 ms long sample that contains 409 pulses. They yield

$$I_{\text{pulse}} = (1500 \pm 250)\,\text{mV}$$

for the pulse intensity and

$$t_{\text{FWHM}} = (180 \pm 10)\ \text{ns} \ \rightleftharpoons\ t_{1/e^2} = (305 \pm 15)\ \text{ns}$$

for the pulse duration. Since the laser position is exactly the same as for the 2f-setup and only the lenses are exchanged, the values for the pulse length are naturally very close. The laser beam width is again estimated to

$$s_{\text{pulse}} = (20 \pm 2)\,\mu\text{m},$$

where only the uncertainty is reduced due to the sharper peaked statistics. The noise amplitude is even smaller with $I_{\text{noise}} = (15 \pm 5)$ mV and the signal amplitude is more than doubled. Thus, the signal quality is enhanced to

$$\text{SNR} \approx 75.$$

It is striking that the histogram in Fig. 6.16 suddenly ends at 1.8 mV, while the distribution would suggest at least some more values to be there. This is because the same laser intensity as before is used, but the dynamical range of the "APD120A/M"-detector is exceeded. As a consequence, for subsequent measurements the laser power is adjusted to exploit the detectors dynamical range without overpowering it.

6.2.2. Closed operation with microscope setup

The top halve, visible in Fig. 6.5, is now installed. This does not change anything related to the detection side compared to open microscope setup. Only the laser window is introduced into the beam path.

The CNM has to be used in under-pressure operation now. The flow is restricted by a critical orifice to $\Phi_{\text{V}} = (1000 \pm 30)\,{}^{\text{cm}^3}/_{\text{min}}$. To prevent condensation of working fluid inside the chamber, the optics is heated to $T_{\text{opt}} = 40°\text{C}$. At this point, it is interesting how the signal quality suffers from lateral or longitudinal detector cage misalignment.

Sensitivity analysis of objective lens misalignment

Two cases are examined to determine the effects of a misalignment between the two lenses in the microscope setup. First, the XY-position of the detector cage including the beam trap is held constant at an optimized position while the gap between the two lenses is increased (Z-direction, corresponds to an elongation of the drift space D2 in Fig. 6.4). Second, the XZ-position of the detector cage is held constant and a shift along the X-axis is performed. The beam trap always stays in the same location, otherwise the laser would miss it at after a certain cage shift. The relative position of image lens and detector remains fixed. The results are presented in Fig. 6.18(a) and (b) respectively.

For both cases we do not expect significant changes in pulse duration, since the laser does not move. Measurements confirm that. The variation of the average pulse height is the interesting quantity here, since it has significant influence on SNR.

The shift along the optical axis gradually lowers the signal amplitude. With a shift of 5 mm about 10% of the signal amplitude is lost. If the distance between the lenses

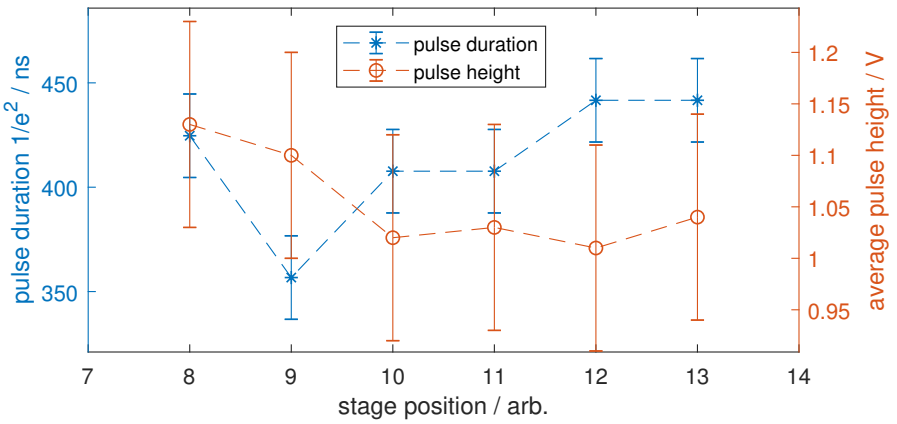

(a) Shift along the optical axis in mm

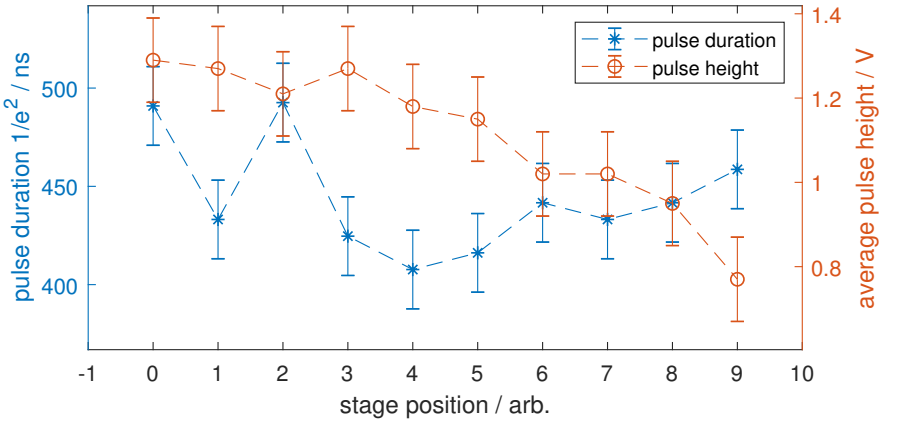

(b) Shift lateral to the optical axis in mm

Figure 6.18.: Influence of lateral or longitudinal cage misalignment. (a) The distance between the two lenses is increased while the xy-Position of the detector cage and beam trap is held constant. (b) The detector cage is shifted along the x-axis while the xz-position is held constant.

is increased, off axis rays with a slight angle to the optical axis (e.g. green lines in Fig. 6.4) will start missing the second lens and thus they won't be mapped onto the detector anymore.

Lateral shift of the detector cage introduces a change in overlap of the lenses free apertures. This has a direct influence on the signal yield. In Fig. 6.18(b), position 0 corresponds to an optimal centered position. This means that the image lens is shifted by more than one third of its diameter and only about 40% of signal intensity is lost.

In summary it can be stated that there is very little influence of small misalignment that could occur due to thermal expansion. Also the initial detector cage alignment

is uncritical and no precision mechanics are needed. In both measurements a longer pulse duration compared to the last section is noted. This is attributed to the lasers Z-position not being perfectly aligned yet. Additionally, the window causes a larger beam waist.

Optimizing the pulse duration

Before the "APD120A/M"-detector is exchanged with the photo diode detector and the counting electronics, the final adjustment of the laser needs to be performed. Laser tilt, X-, Y- and Z- position are optimized to achieve the shortest signal pulses. The signal amplitude is adjusted simply by varying the laser power, where a mean value of about 1 V is desired to fit the dynamical range of the detector[5]. As a consequence, the statistics of Fig. 6.14 and Fig. 6.16 are not comparable to the following pulse height measurements.

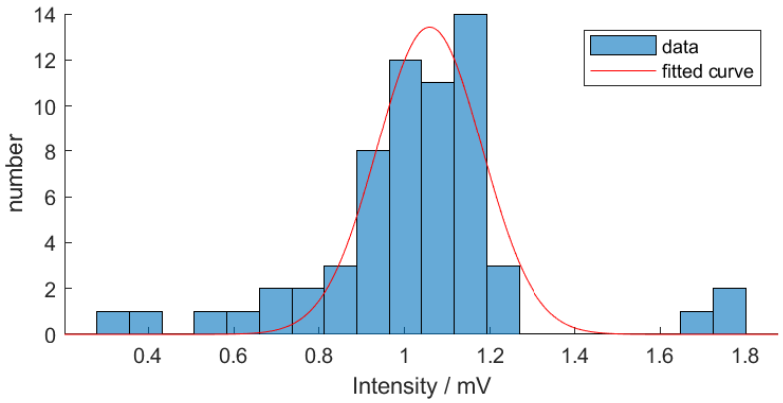

Figure 6.19.: Pulse height with prototype III in closed microscope setup. The histogram is based on 62 pulses. A Gaussian distribution function fitted to the data set yields $I_{\text{pulse}} = (1050 \pm 150)\,\text{mV}$ for the pulse height (1 sigma confidence interval).

The sample recorded with the final configuration is with 400 µs rather short and contains only 62 pulses. The statistics are given in Fig. 6.19 and Fig. 6.20. The desired voltage range around 1 V is attained very well with a pulse intensity of

$$I_{\text{pulse}} = (1050 \pm 150)\,\text{mV}.$$

A pulse duration of

$$t_{\text{FWHM}} = (180 \pm 10)\ \text{ns} \ \rightleftharpoons\ t_{1/e^2} = (300 \pm 20)\ \text{ns} \tag{6.6}$$

[5]Later with the AVL-ADC-sensor board, the laser power is again re-adjusted to fully exploit its dynamical range without risking saturation.

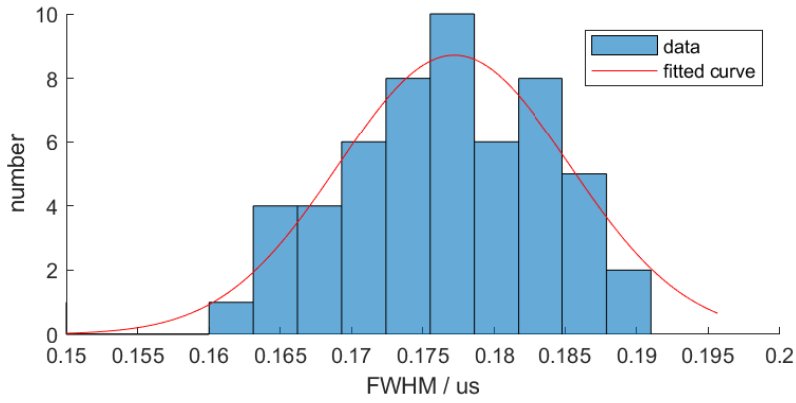

Figure 6.20.: Pulse length with prototype III in closed microscope setup. The histogram is based on the same 62 pulses as Fig. 6.19. A Gaussian distribution function fitted to the data set yields $t_{\mathrm{FWHM}} = (180 \pm 10)\,\mathrm{ns}$ for the pulse duration (1 sigma confidence interval).

could be realised. The estimated beam width is

$$2w_{0,\mathrm{laser}} = (20 \pm 3)\,\mu\mathrm{m}, \tag{6.7}$$

which agrees within the deviation interval with the measured value for window A in Tab. 6.1 ($2w_0 = (22.2 \pm 0.2)\,\mu\mathrm{m}$). Figure 6.21(a) shows an excerpt containing several pulses of the optimized signal. In Fig. 6.21(b) one pulse is visible in detail.

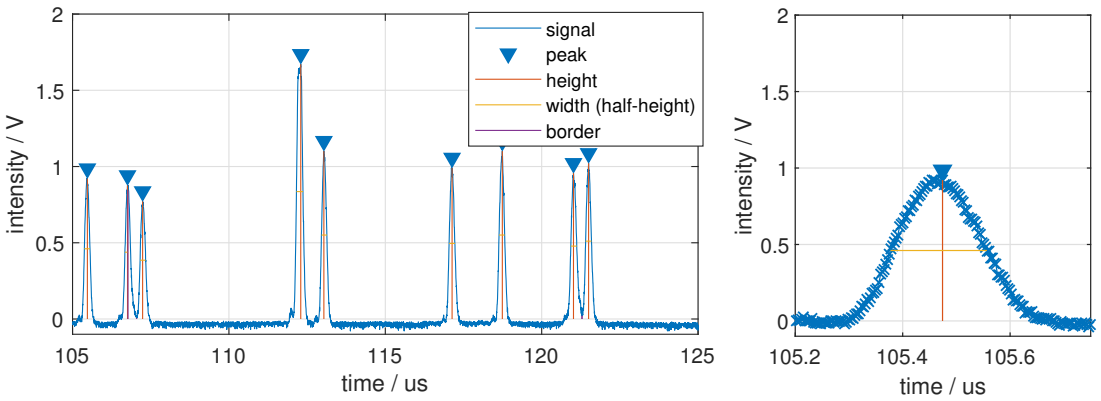

(a) Example pulses (b) Detail

Figure 6.21.: Excerpt from a particle signal from prototype III on the conventional CPC. (a) Example pulses with a FWHM of approximately 300 ns. (b) Detail on a single pulse.

With the manually reduced laser power and a noise amplitude of $I_{\mathrm{noise}} = (20 \pm 5)$ mV signal quality of

$$\mathrm{SNR} \approx 50$$

was achieved.

6.2.3. Incorporation of the AVL-ADC-sensor board

The signal quality achieved with prototype III so far is good enough to employ the AVL-ADC-sensor board. See Sec. 3.1.5 for a description of the detector. For the following test, particles from a standard salt generator [49] are sampled by the CNM. The salt generator is operated with a 50 ppm salt solution at 2 bars.

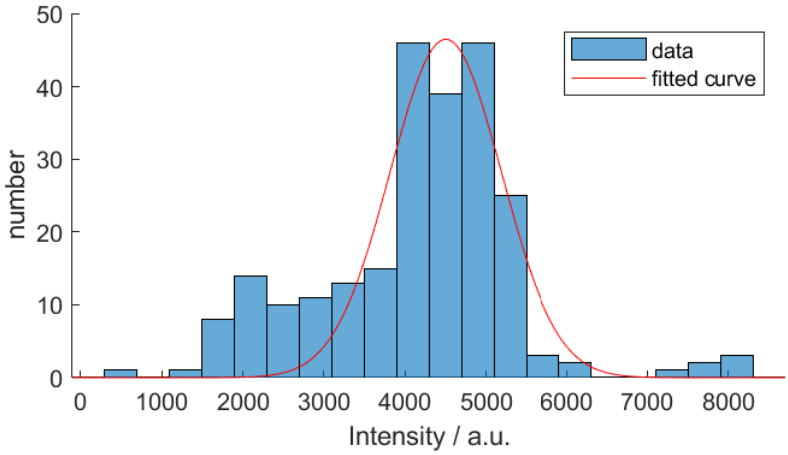

Figure 6.22.: Pulse height with prototype III in final setup. The histogram is based on 240 pulses. A Gaussian distribution function fitted to the data set yields $I_{\text{pulse}} = (4500 \pm 800)$ a.u. for the pulse height (1 sigma confidence interval).

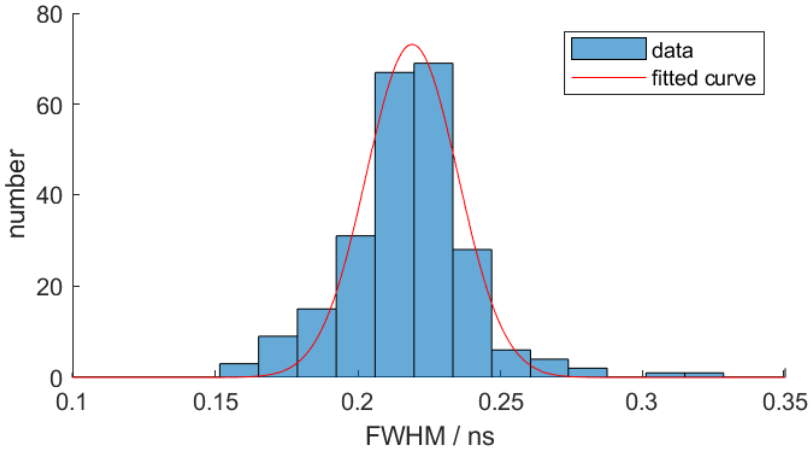

Figure 6.23.: Pulse length with prototype III in final setup. The histogram is based on the same 240 pulses as Fig. 6.22. A Gaussian distribution function fitted to the data set yields $t_{\text{FWHM}} = (240 \pm 20)$ ns for the pulse duration (1 sigma confidence interval).

The AVL-ADC-sensor board software allows to read the sample data of 1 ms collection time, which corresponds to 50.000 data-points at a sample frequency of 50 MHz.

In Figure 6.22 and Fig. 6.23 the corresponding statistics are plotted. For the pulse duration

$$t_{\mathrm{FWHM}} = (240 \pm 20)\ \mathrm{ns} \ \rightleftharpoons\ t_{1/e^2} = (370 \pm 35)\,\mathrm{ns} \tag{6.8}$$

is found. However, the laser position is identical to the one from Sec. 6.2.2 and yet a significant broadening of the pulse length is observed. This phenomenon was eventually back-traced to the upper frequency limit of electronics on the AVL-ADC-sensor board. Even though the optical pulse is assumed to be shorter, the electronic elements of the amplifier act like a low-pass filter with a cut-off frequency in this range. At this point an estimation of the laser beam width is futile.

The maximum value the ADC can resolve is 8175 a.u.. Therefore, the laser intensity was adjusted such that the dynamical range of the detector can be exploited. The pulse intensity is set to

$$I_{\mathrm{pulse}} = (4500 \pm 800)\,\mathrm{a.u.}$$

With $I_{\mathrm{noise}} = (200 \pm 50)\,\mathrm{a.u}$[6] the signal quality is determined to

$$\mathrm{SNR} \approx 23$$

and is thereby improved almost by a factor of 3 compared to Sec. 4.5.4 (SNR ≈ 8). Even though this does not seem to be a major improvement, the slopes of the signal do not contain fringes anymore. Thus, the AVL-ADC-sensor board can be employed with confidence. Figure 6.24(a) shows an excerpt of the recorded signal and Fig. 6.24(b) one pulse in detail. Comparing that to Fig. 4.22, this is a significant improvement.

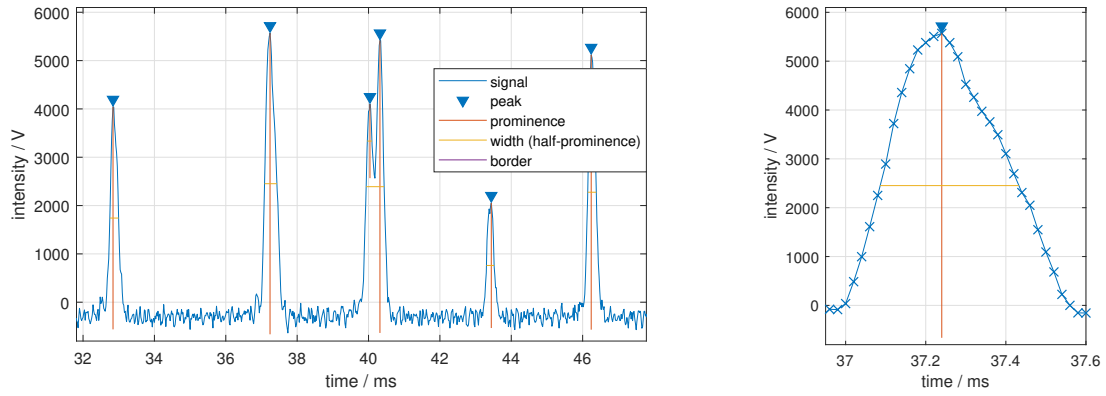

(a) Example pulses (b) Detail

Figure 6.24.: Particle signal from prototype III with the conventional CPC. (a) An excerpt with example pulses, the signal SNR is ≈ 23. (b) Looking at the center pulse in detail, one can see the steadily rising edge without any fringes.

The same algorithm which is used in the FPGA on the detector board, is available in script form for Matlab. Using that script, the data read from the AVL-ADC-sensor

[6]The main contribution to this noise is attributed to the amplifier and the ADC electronics.

board is evaluated and benchmarked against the Matlab-function "findpeaks()". In this way, it is possible to find the best performing values for the counting algorithm. The final optimized parameters are listed in Tab. 6.2.

Table 6.2.: Optimized parameters for the peak count algorithm of the AVL-ADC-sensor board

Option	value
THRHLD_PK	750
SMPL_MN_INCR	150
SMPL_MIN_DECR	10
SMPL_PK_VALD	3

With these parameters the counting algorithm was tested for several data sets with higher and lower pulse densities, see Tab. 6.3. This rather simple evaluation yields a peak detection efficiency of about 97%.

Table 6.3.: Detection efficiency for the peak count algorithm of the AVL-ADC-sensor board. The peak quantity for the 1 ms long samples is determined using the Matlab-function "findpeaks()". η... detection efficiency

data set	peak quantity	AVL-ADC-sensor board	η
1	240	221	92%
2	299	288	96%
3	111	107	97%
4	78	78	100%
5	24	24	100%
6	30	29	97%
		mean:	97%

6.3. Final optics setup

The full optical setup with prototype III including all components is shown in Fig. 6.25.

On the detector side also a simple cage system is introduced. Image-lens and optical bandpass filter are mounted inside a "LCP02/M" 30 mm to 60 mm cage adapter plate. By moving the adapter plate back and forth, the distance between the two lenses is selected. A "LCP03/M" blank cage plate is custom milled to house the AVL-ADC-sensor board. By sliding it along the 60 mm cage the image distance is adjusted to 40 mm.

The distance between the laser and the nozzle center is set to $d_{MgF_2} = (95.50 \pm 0.05)$ µm, as determined in Sec. 6.1.6. With the XY-stages the laser is adjusted such that it

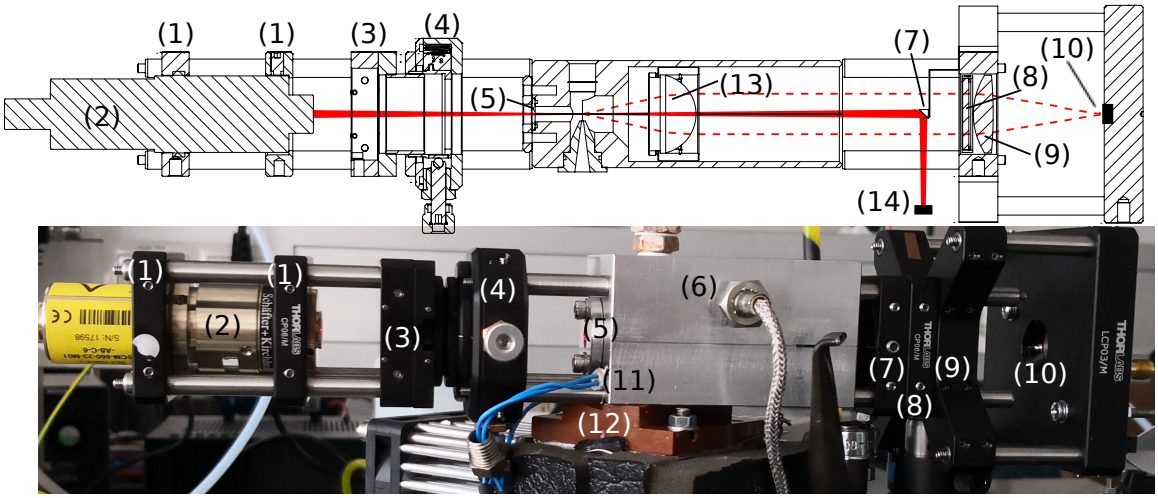

Figure 6.25.: Final optics setup with prototype III. (1) Custom made tripod retainer to align the laser with the cage. The laser is leveled by rotation and the working distance is adjusted by moving the retainer along the cage rods. (2) Schäfter & Kirchhoff laser. (3) Slip Plate positioner for coarse and (4) XY-translation stage for fine adjustment in radial direction. (5) Laser window with retaining ring. (6) M8-tap for PT100 3-wire temperature sensor (thermocouple as alternative). (7) Suspended prism mirror that reflects the light out of the regular optical path. (8) Optical bandpass filter. (9) Objective lens, 40 mm best-form lens housed inside the cage adapter plate. (10) Detector, AVL-ADC-sensor board. (11) Heating cartridges. (12) Thermally isolating base plate. (13) Plano convex objective lens. (14) Beam dump.

traverses the chamber perfectly centered. The plano convex objective lens is placed with its principal plane 25.4 mm away from the nozzle centre.

6.4. Verification with conventional CPC

A verification of the full setup is done on the conventional CPC before switching over to the HTCPC. The performance is evaluated by looking at the linearity and upper counting limit. With the linear regime and the upper counting limit determined, the new optics is then used to determine the characteristics of the conventional CPC. Thereby a reference frame is established before moving on to the HTCPC.

6.4.1. Measurement setup

To conduct controlled measurements of aerosols a sophisticated laboratory setup is necessary. The schematics is given in Fig. 6.26.

Pressurized air (Fig. 6.26(part 1)) is first cleaned in an oil separator (2) before it is connected to the particle source. As standardized particle source, a salt generator [49]

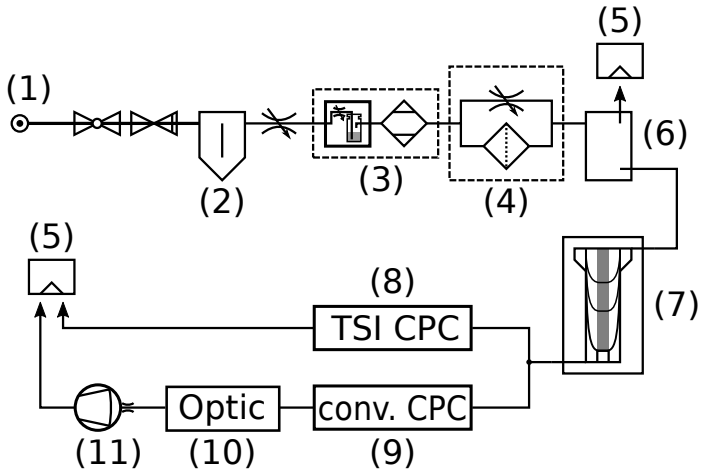

Figure 6.26.: Measurement setup for the verification process of prototype III. (1) Pressurized air source, >8 bar. (2) Oil separator and valve for pressure reduction to 4 bar. (3) Salt generator with pressure reduction to 2 bar, operated with a 50 ppm solution and an air dryer column downstream. (4) Dilution bridge stage (DBS). (5) Exhaust ventilation system. (6) Expansion volume, pressure reduction to ambient pressure. (7) DMA (see Sec. 3.1.3. (8) TSI 3775 CPC as reference (pump inside the instrument). (9) Laboratory CPC. (10) prototype III optics with AVL-ADC-sensor board as particle counter. (11) Membrane pump with critical orifice.

with a 50 ppm NaCl-solution and 2 bar operating pressure is employed (3). Directly afterwards, the gas containing the salt particles is dried in an air dryer column, which uses silica-based granulate to absorb air moisture. This is an important step, because moisture in the aerosol leads to semi-volatile particles that adulterate the measurements with a conventional CPC. With a *dilution bridge stage* (DBS) the particle concentration is adjusted (4). A DBS is essentially an air filter (e.g. HEPA-filter) with a bypass valve. An expansion volume is used to reduce the aerosol to ambient pressure, since both CPCs used downstream are suction fed. Excess air is vented to an exhaust.

The aerosol sampled with the CPCs (Fig. 6.26(part 8,9)) is first funneled trough a TSI DMA (6), which is used to select particles with a certain mobility diameter. For a more detailed description of this instrument see Sec. 3.1.3. A TSI 3775 CPC (8) is used as benchmark for the laboratory CPC (9) and together they draw a sample flow of up to $2.3\,{}^{\text{l}}/_{\text{min}}$ of from the DMA. The DMA's sheath flow is set to $10\,{}^{\text{l}}/_{\text{min}}$, which constitutes a ratio of about 5:1. That causes a rather broad size distribution with a classification width of ±3%, but in turn a higher particle number is passed through. The impactor size of 0.071 cm is selected appropriately.

The laboratory CPC is operated with the saturator at $T_{\text{sat}} = 38°\text{C}$ and the condenser at $T_{\text{cond}} = 28°\text{C}$. The optics temperature is set to $T_{\text{opt}} = 40°\text{C}$ to avoid condensation of n-butanol in the chamber, especially on window and lens. The lab. CPC flow rate is measured to $\Phi_{\text{V}} = (900 \pm 20)\,{}^{\text{cm}^3}/_{\text{min}}$ using a "red-y compact" flow meter.

For sampling with the AVL-ADC-sensor board, the algorithm parameters determined in Sec. 6.2.3 are used, see Tab. 6.2. For one measurement value, mean and standard deviation of 30 successive samples are used. Each individual sample value represents the pulse count of 100 ms sample time and is followed by 900 ms dead time for processing and data transfer[7], leading to a total collection time of 30 s.

Section 3.1.1 lists the standard operation conditions of the TSI 3775 reference CPC. The measurement with this CPC is conducted simultaneously with the laboratory CPC. Mean and standard deviation of 30 individual samples of 1 s sample duration are collected. The instrument's flow rate is set to 1.3 $^{l}/_{min}$.

6.4.2. Linearity and upper counting limit

To determine the linearity the laboratory CPC with the prototype III optics is benchmarked against the TSI CPC. With the DMA a particle diameter of 50 nm is selected. At this size the CPCs are expected to be operated in a regime where both CNMs have their maximal activation efficiency already. In total they draw (2.2 ± 0.2) $^{l}/_{min}$ from the DMA.

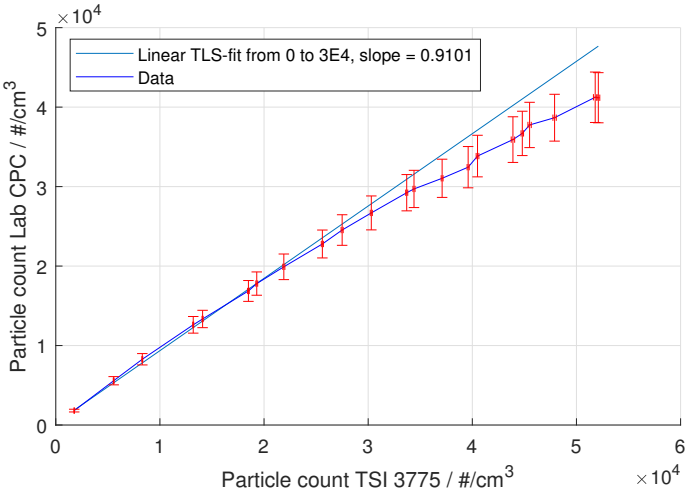

Figure 6.27.: Counting efficiency of conventional CPC with prototype III and salt particles. For a mobility diameter of 50 nm and various concentrations, particle count rates of the laboratory CPC and TSI 3775 CPC are plotted against each other. The particle concentration is controlled by the DBS valve position. For lower count rates there is an adequate linear relationship between the two instruments. Above 30.000 $^{particles}/_{cm^3}$ the laboratory CPC with the prototype III optics unit and AVL-ADC-sensor board starts to drift, which marks the upper counting limit.

[7] A shorter dead time than 500 ms is not recommended, since data transfer from the previous and instructions for the next sample time might start to overlap on the COM-port, thereby scrambling the data.

Figure 6.27 shows a plot of the particle count of the TSI CPC versus the particle count of the laboratory CPC with prototype III optics. By gradually opening or closing the DBS bypass valve the particle concentration is varied.

Starting from about 30.000 $^{\text{particles}}/_{\text{cm}^3}$ the laboratory CPC drifts away from the TSI reference CPC. This value marks the upper counting limit without coincidence correction. Above this concentration coincidence effects start to have significant influence on the particle count. In general, also the TSI CPC experiences such coincidence effects. However, the instruments software features a sophisticated coincidence correction to measure concentrations up to 50.000 $^{\text{particles}}/_{\text{cm}^3}$ in single particle count mode[8] [33].

A *total least squares* fit (TLS fit) to the data from $0 - 30.000\,^{\text{particles}}/_{\text{cm}^3}$ yields a slope of 0.91 for the linear region. This proportionality factor depends less on the counting algorithm itself, but more on the CNM below, which has certain activation efficiency[9] and particle losses. This activation efficiency is an instrument property and is considered later in terms of a device constant k. All error estimations for derived quantities are done by a simple 2-point method.

6.4.3. Counting efficiency of the laboratory CPC

Before the optics is carried over to the HTCPC, it is used to measure counting efficiency curves of the laboratory CPC. Different temperature differences between saturator and condenser cause different super-saturated environments, thereby influencing the nucleation efficiency of the CNM. Here, the saturator temperature will be held constant and the condenser temperature is altered. By lowering the condenser temperature the degree of super-saturation is increased and the activation efficiency should rise, especially for smaller particle sizes. This causes a shift of the Kelvin diameter d* (see Sec. 3.1.1) to smaller values.

In Fig. 6.28 the counting efficiency curves of the laboratory CPC for salt particles as sample aerosol are plotted. For the higher condenser temperature of 30°C the Kelvin diameter is with 40 nm visibly larger than for other condenser temperatures, where it is below 20 nm. However, for salt particles the activation efficiency at small particle sizes is different compared to particles from combustion processes.

Therefore, a second measurement is conducted employing a tungsten-oxide (WOx) aerosol standard. In particular a "Grimm 7860 WOx generator" [50] is used, which unlike the salt aerosol standard produces particles that are more similar to actual combustion products. Conveniently, the WOx generator does not constitute a complicated measurement setup yet. However, the aerosol flow provided by the WOx generator

[8] For concentrations above that value the instrument switches into a "photometric mode" as an alternative measurement method, where basically the opacity of the gaseous stream is the measured parameter [33].

[9] The probability that a condensation nucleus actually forms a droplet of working fluid.

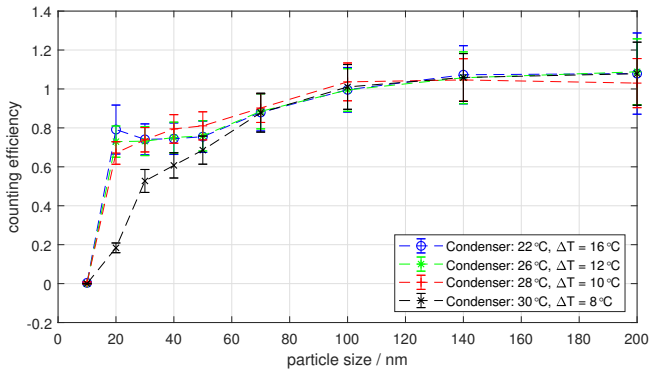

Figure 6.28.: Counting efficiency of conventional CPC with prototype III and salt particles. The particle size corresponds to the electrical mobility diameter selected by the DMA. The activation efficiency for salt particles and n-butanol as working fluid is rather high [15, p. 390]. Hence, the curves for condenser temperatures between 22°C and 28°C cannot be distinguished in a conclusive way. Only for a condenser temperature of 30°C a shift of the Kelvin diameter to larger particle sizes is visible.

is lower than the 2.2 l/min drawn from the expansion volume. As a consequence the sample flow setting of the TSI 3775 is reduced to 0.3 l/min, which in turn reduces the sample flow through the DMA to 1.2 l/min. To hold up the same ratio of about 1:5, the sheath flow is reduced to 6.5 l/min.

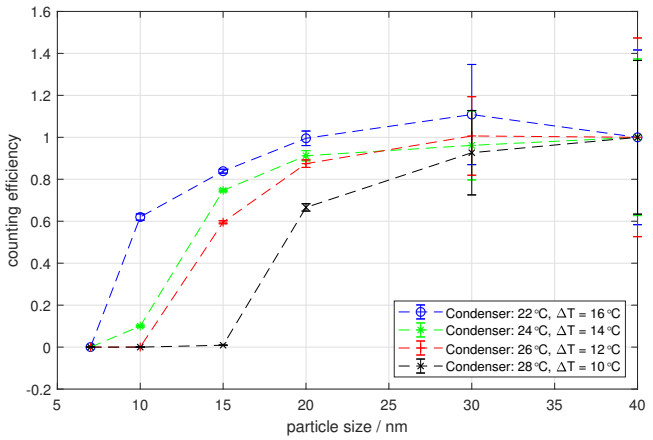

Figure 6.29.: Counting efficiency of conventional CPC with prototype III and WOx particles. The particle size corresponds to the electrical mobility diameter selected by the DMA. Saturator at $T_{\mathrm{sat}} = 38°\mathrm{C}$. It is clearly visible that for a greater super-saturation, hence lower condenser temperatures, the Kelvin diameter shifts to lower particle diameters.

Figure 6.29 shows the counting efficiency curves of the laboratory CPC for WOx particles as sample aerosol. Because the generated WOx particles are very small (mean diameter $\approx 15\,\mathrm{nm}$), the maximum tested diameter is limited to 40 nm.

6.5. High temperature operation

In this last step the newly designed prototype III optics is mounted onto the HTCPC. Before starting up the high temperature CNM, the long term stability at high temperatures has to be evaluated. A first test run at 70°C showed that the cage system has to be slightly modified and cooled for chamber operation over 200°C. The heat transferred via the cage rods towards the optical elements is too high to be dissipated by the cage plate's small surface area.

6.5.1. Cage cooling and temperature stability

Firstly, the slip plate positioner and the XY-stage are exchanged compared with Fig. 6.25 in order to move the XY-stage,(with its plastic components inside) further away from the hot chamber. Then, heat sinks are mounted onto the slip plate positioner on the laser side and the 30 mm-60 mm cage plate adapter on the detector side. Since the latter also houses the optical band-pass filter and lens, those elements are guaranteed to be cooled as well. Because the heat sinks add plenty of weight to the cage, a custom detector board retainer is 3D-printed to reduce weight.

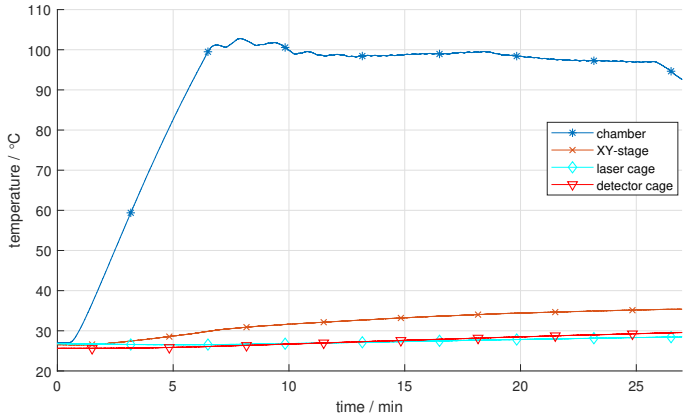

Figure 6.30.: Temperature stability of prototype III. The chamber is heated to 100°C with heat sinks applied on laser and detector cage, but without fiberglass isolation on the chamber yet. In Fig. 6.31 the sensor positions are indicated. The over-heating, caused by the ill-parametrized temperature control unit, is clearly visible. At $t = 18\,\text{min}$ the heating is turned of and the chamber temperature reduces, while the cage keeps heating up.

The progress of heating the optics to 100°C with heat sinks applied is visible in Fig. 6.30. After 6 minutes, the temperature exceeds the targeted 100°C and over-heating occurs. This is because the heat, spreading from the heating cartridges in the bottom halve, reaches with great delay the temperature sensor, which is mounted in the top halve. In general, such overheating is easily prevented by the regulatory

circuit of the temperature control unit. However, fine-tuning the control parameters of the feedback loop is beyond the scope of this work at this point. Also, over-heating is no problem as long as the optical elements do not get too hot, since the main purpose of the chamber's high temperature is to prevent condensation inside. After about 18 minutes heating is turned off and the chamber temperature begins to fall. Naturally, the cage keeps heating up as long as there is heat supplied to the metal rods, which causes the cage temperatures to keep rising after turn off. Based on experience, heating the unit to its intended 215°C and reaching a stable temperature state takes 15-20 min, depending on the initial temperature. Thereafter the regular operation may start.

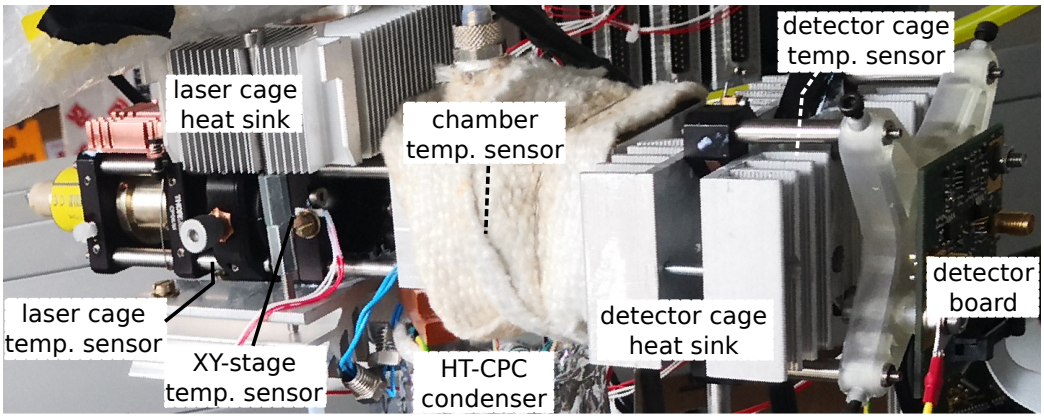

Figure 6.31.: Thermal isolation of prototype III and cooling of the cage system. Compared to Fig. 6.25, heat sinks have been mounted to the cage elements and a fiberglass mat was added to enhance temperature stability and to facilitate a more uniform temperature distribution. The detector board is mounted now in a light-weight 3D-printed retainer.

Although this measurement is conducted at lower than target temperatures, it shows that air convection in combination with the heat sinks is clearly enough to dissipate the heat transferred via the cage rods towards the laser and detector components. No active cooling is needed.

6.6. Thermal distribution during the heating process

For the measurement with a thermal camera shown in Fig. 6.32, one side of the chamber is painted with matt, black oven paint. While the chamber is heated to 120°C, thermal images are recorded using a "Flir Ex E4" IR-camera. In Fig. 6.32(a) and (b) it is clearly visible how the heat spreads out from the heating cartridges. Figure 6.32(c) shows the image at maximum over-heating, where (142 ± 2)°C are reached. After 10-15 min the temperature has stabilized and the thermal distribution gets more uniform as seen in Fig. 6.32(d). After several instances of heating up and cooling down the system did not show any signs of deformation or misalignment.

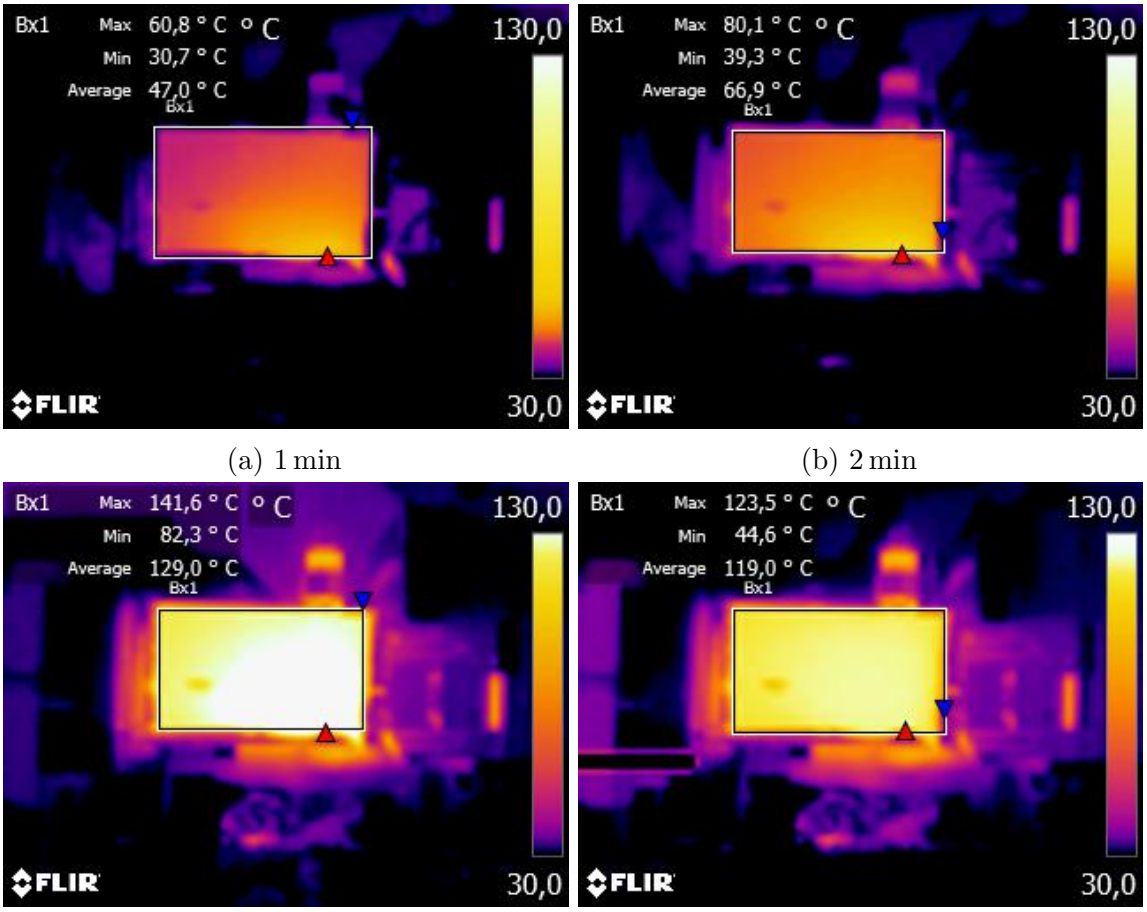

(a) 1 min (b) 2 min

(c) 6 min (d) 12 min

Figure 6.32.: Thermal distribution during heat-up of prototype III. The rectangle marks the chamber outline. (a) Heat starts spreading spreading from the cartridges. (b) Some cage elements start to show in the thermal image. (c) Over-heating. (d) Uniform thermal distribution. Deviation in temperature measurement is ±2°C [51].

Finally, a thermal insulation made from fiberglass is applied to the chamber to enhance temperature stability and foster a better temperature distribution throughout the chamber. Figure 6.31 shows the whole newly designed optical setup applied to the HTCPC. The system in this configuration promises a very good stability and no necessity for re-alignment.

7. Operation of prototype III with the HTCPC

With the new high temperature particle counting optics described in Chap. 6, an evaluation of the HTCPC can be performed. A verification of the HTCPC has been done by Kügler [21] and Kupper, Kraft, Bergmann & Boies [20]. In this chapter, the prototype III optics will be used to perform a preliminary measurement of the HTCPC counting efficiency. A key part here is the counting optics long term stability. The eventual goal is to get the HTCPC ready for a full characterization process.

7.1. Measurement setup

Detailed schematics of the measurement setup are given in Fig. 7.1. As particle source a miniCAST (Fig. 7.1(part 3)) is used, see Sec. 3.1.4. It produces soot particles with similar properties to those from diesel engine exhaust gasses. The miniCAST is operated with its standard operation parameters, listed in Tab. 3.2. With over-pressure, particles are transported from miniCAST through a DBS (4), a catalytic stripper (6) (see Sec. 3.1.2) and the DMA (7) (see Sec. 3.1.3) into an expansion volume (16). A catalytic stripper is necessary to remove semi-volatile particles before measurement, because as reference the regular n-butanol driven TSI 3775 (8) is used (see Sec. 3.1.1). Both the reference CPC (8) and the HTCPC (9) draw the sample aerosol from the expansion volume. The excess air from the miniCAST and the expansion volume is drained into an exhaust ventilation system (5).

The sample aerosol flow drawn by the CPCs thought the TSI 3082 DMA is 1.8 l/min. To again have a sample-to-sheath flow ratio of about 5:1, the sheath flow is set to 10 l/min and the impactor size of 0.071 cm is selected. With the instrument flow rate set to 0.3 l/min, the reference CPC samples the aerosol simultaneously with the HTCPC, recording mean and standard deviation of 30 individual samples of 1 s sample period each.

A rotary vane pump with a critical orifice ("main pump", Fig. 7.1(part 15)) establishes the volume flow of 1 l/min through the HTCPC. It transports nitrogen gas (= carrier gas) through the saturator, where it is loaded with working fluid, and then further into the condenser, where the supersaturation is initiated by chilling the gas. The

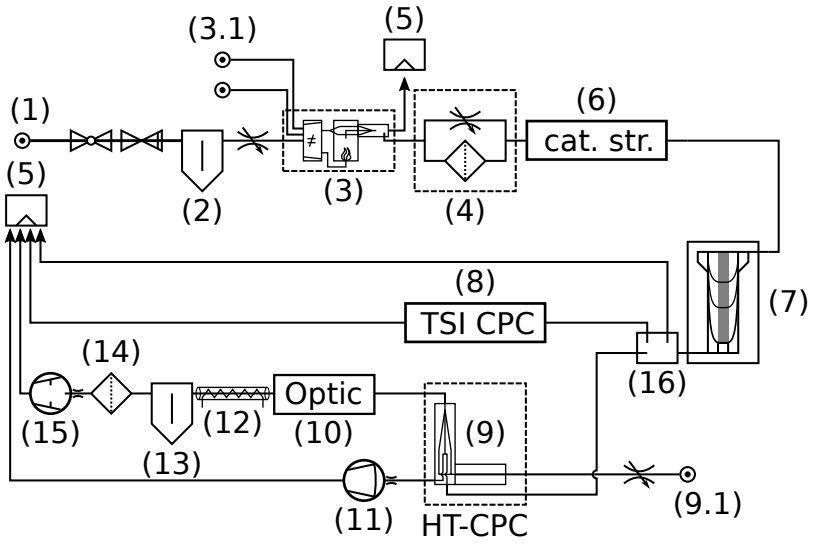

Figure 7.1.: Measurement setup for the verification process of Prototype III. (1) Pressurized air source, >8 bar. (2) Oil separator and valve for pressure reduction to 3.75 bar. (3) CAST soot generator (see Sec. 3.1.4), pressure reduction to ambient pressure. (3.1) Propane and nitrogen supply for miniCAST soot generator. (4) DBS, needle valve and HEPA filter in parallel. (5) Exhaust ventilation system. (6) Catalytic stripper (see Sec. 3.1.2). (7) DMA (see Sec. 3.1.3). (8) TSI 3775 CPC as reference, pump inside the instrument. (9) HTCPC. (9.1) Nitrogen supply for HTCPC. (10) Prototype III optics with AVL-ADC-sensor board as particle counter. (11) "Sample pump", membrane pump with critical orifice. (12) Flexible tube heated to 60°C. (13) Working fluid separator, condensation trap. (14) HEPA air filter for pump protection. (15) "Main pump", rotary vane pump with critical orifice. (16) Expansion volume.

nitrogen itself is drawn from an expansion volume, supplied by a regular gas bottle (9.1). In the condenser the sample flow joins with the super-saturated volume flow and condensation of the working fluid on the nuclei is triggered. The high temperature counting optics from Sec. 6.3 (10) is attached on-top of the condenser section. After the droplets passed the optics and have been counted, a heated tube (12) funnels the hot supersaturated gas through a cold trap (13), where the working fluid is separated from the carrier gas. While the main pump sustains the HTCPC, the sample pump (membrane pump) (11) with a 1 l/min-limiting critical orifice transports the sample aerosol past the capillary inlet, from which the sample aerosol is drawn into the condenser section. The excess air from both pumps is lead to an exhaust ventilation system (5). For the AVL-ADC-sensor board the algorithm parameters from Tab. 6.2 are used again. The pulse count of 250 ms sample time is followed by 750 ms dead time. Mean and standard deviation of 30 successive sample periods result in the final measurement value.

7.2. Counting efficiency

Similar to the measurement conducted in Sec. 6.4.3, the counting efficiency of the HTCPC is determined. The HTCPC is operated at a fixed condenser temperature of $T_{\mathrm{cond}} = 180°\mathrm{C}$. This is the minimal temperature it may be operated at to keep all volatile components in the gas phase. With the lower temperature T_{cond} fixed, the saturator temperature has to be increased or decreased to alter the degree of super-saturation in the condenser section.

By changing the carrier gas temperature during saturation, the working fluid's partial vapor pressure is influenced, thus the capacity of working fluid in the gas phase changes. This in turn also dictates the amount of working fluid in the super-saturated vapour state later in the condenser section.

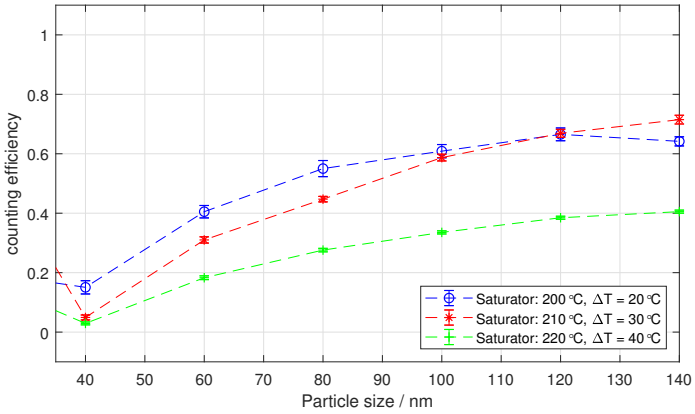

Figure 7.2.: Counting efficiency of the HTCPC. The newly developed counting optics is used to measure a preliminary counting efficiency of the HTCPC. The condenser temperature is held constant at 180°C, while the saturator temperature is varied.

Figure 7.2 shows the counting efficiency for three different differential temperatures, $\Delta T = 20/30/40°\mathrm{C}$. They constitute saturator temperatures of $T_{\mathrm{sat}} = 200/210/220°\mathrm{C}$. The optics temperature is set to be at least 15°C higher than the saturator temperature, hence $T_{\mathrm{opt}} = 215/225/235°\mathrm{C}$. For each data point the measurement is repeated five times with both the TSI CPC and the HTCPC simultaneously.

The measurement has indicated a great particle loss in this setup. The counting efficiency is expected to reach 100% far below 100 nm already. Further, the three curves appear in reverse, unlike the expectations, where a higher saturator temperature (= greater super-saturation) should cause higher counting efficiency and smaller Kelvin diameter, like seen in Fig. 6.29 for the conventional CPC and WOx particles. A survey of this phenomenon is far beyond the scope of this thesis and will not be discussed here. For a detailed discussion of influences and effects related to the HTCPC working principle, refer to Kupper, Kraft, Bergmann & Boies [20].

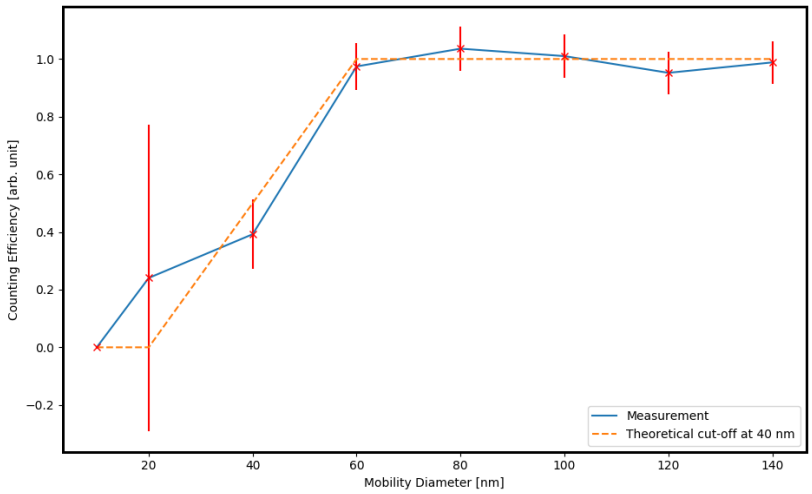

Figure 7.3.: Counting efficiency of the HTCPC. The newly developed counting optics is used to measure a preliminary counting efficiency of the HTCPC[1].

As a consequence of this immanent high particle loss, the setup was carefully rebuilt with new tubing and a cleaned instrument. In Fig. 7.3 the measurement with the reconditioned setup is presented, which is also published in "High-Temperature Condensation Particle Counter Using a Systematically Selected Dedicated Working Fluid" by Kupper, Kraft, Bergmann & Boies [20]. Only one saturator temperature, $T_{\mathrm{sat}} = 200°\mathrm{C}$, has been tested for now. The cut-off diameter for the HTCPC in this setup is at

$$d_{50} = (45 \pm 5)\,\mathrm{nm}. \tag{7.1}$$

Here, theoretical particle losses in tubing for certain particle sizes have been considered too.

[1]Figure taken from Kupper, Kraft, Bergmann & Boies, "High-Temperature Condensation Particle Counter Using a Systematically Selected Dedicated Working Fluid" [20].

8. Conclusion

As a starting point of this thesis a thorough analysis of an existing setup, prototype I, was performed (Chap. 4). Together with knowledge gathered from prototype II (Chap. 5), a final high temperature optics unit, prototype III, was designed (Chap. 6). As a final step, the newly developed optics is used to evaluate the HTCPC.

8.1. Evaluation of prototype I and prototype II

The first simple solution, prototype I, uses a cylinder lens in combination with a collimated laser source to create a thin sheet of laser light right above the nozzle. Particles traversing the laser light sheet cause stray light that is then captured by a lens and imaged onto a detector.

By carefully examining every element of prototype I, several issues have been identified and key points in development for a succeeding prototype have been derived (see Sec. 4.6). A new prototype has to have a feasible way to check the laser focus above the nozzle. The utilized laser in combination with the focus optics has to be of high beam quality to guarantee a thin laser light sheet. Thus, diffractive optics are not an option. In the detection path, the beam trap has to be designed such that it obstructs as little scattered light as possible, while efficiently annihilating the beam. In order to guarantee a good collection efficiency, the focal distance of the objective lens has to be adjustable. Also, the angle of total internal reflection has to be considered to avoid the virtual aperture effect.

After the optimization process of the elements described in Sec. 4.2 a pulse duration of $t_{1/e^2} = (560 \pm 35)\,\mathrm{ns}$ (Eq. (4.6)) was achieved during operation on the HTCPC, see Fig. 4.19. With that value and the known flow rate, the laser light sheet width is calculated to $2w_{0,\mathrm{laser}} = (36 \pm 5)\,\mu\mathrm{m}$ (Eq. (4.8)).

In Chap. 5, a second prototype was inspected. It is an optic that utilizes an elliptical mirror to collect scattered rays and image them onto a detector, which in this case is a multi-mode fiber. The light sheet above the nozzle is also established by a collimated laser in combination with a cylinder lens, with the major advantage that the lens is mounted inside an adjustable tube to fine-tune the laser focus. However, exactly this functionality is the root cause why this prototype failed. The tube to adjust the lens

presumably deformed or buckled during heat-up and/or cooling down, which caused it to be dead-locked inside the main block. In Sec. 5.3 this module failure is described in more detail.

Despite the troubles, it was possible to collect samples for a performance evaluation, see Fig. 5.4. A pulse duration of $t_{1/e^2} = (700 \pm 50)\,\mathrm{ns}$ (Eq. (5.1)) has been found. It is quite likely that this prototype is capable of shorter pulses, but further examinations were not possible due to the module breakdown.

Nevertheless, important knowledge has been gathered through the examination of this prototype, as listed in Sec. 5.4. The elliptical mirror was naturally chosen as central element, where the surrounding parts are adjusted to. However, neither the nozzle, which dictates y- and z-position of the scattering volume (the x-position is guided by the placement of the laser light sheet), nor the fiber, where x- and z-position are fixed and only the positioning along the y-axis is possible to adjust to the mirror's focal length, are flexible enough to align the detection path very well. In conclusion, a potential new high-temperature counting optic has to be designed in a way to minimize co-dependent optic elements on one hand, but on the other hand allow a maximal flexibility in adjustment.

8.2. Development and verification of prototype III

With lessons learned from prototype I and II, a new optics setup for high temperature operation was developed. The key components were carefully selected (see Sec. 6.1) and a new chamber with great capabilities to inspect and debug the optical path was designed (see Sec. 6.1.4).

By using Mie theory (discussed in Sec. 2.2), the capture efficiencies for different lens setups were determined (Fig. 6.3), with the outcome that the microscope like setup is better, yet not decisive superior. However, in summary it guarantees an inherent misalignment free setup (see Sec. 6.2.2). As beam trap, a right-angle prism mirror was introduced with the major advantage, that the beam is annihilated elsewhere and stray light in the detection path is reduced.

With the chamber being separated into two halves, it is possible to examine the light sheet width directly. In closed operation, no sealant on the contact surface is necessary due to the high machining quality. The only critical seal is at the laser window, where an O-ring seal is used that expands over the intersection between the two halves. The lens is freely movable along the optical axis and clamped between the two halves, which holds it in place. A Thorlabs Cage System, which contains all other components, is attached directly to the chamber and guarantees a rigid structure. An analysis of thermal deformation of the cage rods in Fig. 6.12 yields rather small influence.

As new laser a Schäfter & Kirchhoff Micro line generator is used, which is evaluated in Sec. 6.1.5. In Sec. 6.1.6 the window's influence on the laser focal region is explored, Table 6.1 lists the results. A window increases the Rayleigh range as well as the line width by 6-10%. The working distance also increased by 400-450 µm. In the process of selecting the new windows, a suitable coating for windows and lenses at high temperatures (up to 250°C) has been found: Magnesium fluoride, MgF_2. The new setup in its final configuration is described with all its components in Fig. 6.25.

Verification with a conventional CPC showed a pulse duration of $t_{1/e^2} = (300 \pm 20)$ ns (Eq. (6.6)) and the laser light sheet width is calculated to $2w_{0,\text{laser}} = (20 \pm 3)\,\mu\text{m}$ (Eq. (6.7)). This shows the great improvement compared to prototype I. However, after the implementation of the AVL-ADC-sensor board and without any other changes to the system, the pulse duration was determined to $t_{1/e^2} = (370 \pm 35)$ ns (Eq. (6.8)). This unfortunate broadening of the pulse was back-traced to the upper frequency limit of the amplifier electronics, which acts like a low-pass filter.

With the AVL-ADC-sensor board mounted as detector unit the peak count algorithm parameters are optimized to reach a high detection efficiency and a high maximum count rate. The optimized values are listed in Tab. 6.2.

The new optics was characterized on the conventional CPC before switching over to the HTCPC. In Fig. 6.27 the upper counting limit was determined to 30.000 $^{\text{particles}}/_{\text{cm}^2}$, which marks the end of the linear regime. In the course of the counting efficiency measurement of the conventional CPC in Sec. 6.4.3, also the long term measurement stability was verified.

Section 6.5 discusses the application of prototype III on the HTCPC. Heat sinks had to be mounted on the cage system in order to keep the optical elements within their rated temperature range, though no active cooling is needed. The thermal distribution during an exemplary heating process is visible in Fig. 6.32 and shows that over-heating takes place due to a slow regulatory circuit of the temperature control unit.

8.3. Evaluation of the HTCPC using prototype III

Due to the optics prototype III, reliable particle counting in laboratory measurements with the HTCPC is possible now, see Chap. 7. Unlike the expectations, the three curves for the counting efficiency in Fig. 7.2 appear in reverse. A higher saturator temperature (= greater super-saturation) should cause an increased counting efficiency and reduced Kelvin diameter. This indicates that further research in this area is required. Nevertheless, long term high temperature stability of the counting optics was proven to temperatures up to 235°C.

Figure 7.3 shows a second counting efficiency measurement conducted with a renewed measurement system for one differential temperature, $\Delta T = 20°C$, where also particle losses in dependence of diameter are corrected. The cut-off diameter for the HTCPC in this setup appears to be $d_{50} = (45 \pm 5)\,\mathrm{nm}$ (Eq. (7.1)), which is about 20 nm higher than the goal of 23 nm, prescribed by the EU/ECE Regulation 83/49 [10].

9. Outlook

Optics prototype III enables reliable particle counting with the HTCPC. It is now possible to start the full characterization of the HTCPC under laboratory conditions. The high temperature particle counting optics is now in a ready-to-go state, where an optimization of the operation temperatures of all instrument sections may be performed in future testing.

9.1. The instrument's potential and technology prospect

The high operation temperature of the condenser section enables this instrument to directly measure the solid particle number from sample aerosols without intensive pre-conditioning. By operating above 180°C the volatile and semi-volatile components stay in the gaseous state. Therefore, this instrument has great potential for direct automotive exhaust gas measurements. Together with the high temperature particle counting optics, prototype III, intensive tests can be performed now.

Subsequent to the finalization of this thesis, the HTCPC with the prototype III counting optics was successfully tested on a dynamo for direct automotive exhaust gas measurements. However, a benchmark against current systems with exhaust gas pre-conditioning is yet to be done.

9.2. Issues to address

Although the instrument performs well and measurements are possible, there are some issues to address for further development:

- Even though there was suspected particle loss in the measurement of Fig. 7.2, the counting efficiency curves should appear in reverse order. This calls for further investigation of the HTCPC with this working fluid and possibly a redesign of the condenser section.

- The volume flow across the capillary is one of the most crucial parameters. Unfortunately, attaining this value proved to be challenging. Without this parameter known precisely, the measurement is compromised.
- Another topic for the development of a fully functional test system with the HTCPC will be a cold trap to separate working fluid efficiently. At the moment, separation of the working fluid from the carrier gas is performed by pumping through a water bath to cool it down and successive filtering. However, the filters clog after a certain operation time and the water heats up to a point where it starts to evaporate quickly. To enable a user-friendly long term operation, an efficient separation is essential. Also, recovery of working fluid might be possible.
- The current feedback loop of the system is too slow and causes both saturator and condenser to undergo variations in temperature in the ± 0.4°C-range with a frequency of approximately 1 Hz. The control unit to set the different temperatures of saturator, condenser and optics needs to be refined for a defined instrument operation.

List of Figures

List of Tables

Bibliography

1. Kupper, M., Kügler, M., Gleichweit, M., Kraft, M., Koch, M. & Bergmann, A. High-Temperature Condensation Particle Counter Optimized for Engine Exhaust. Article in preparation (2019) (cit. on pp. v, vii).
2. Axmann, H. *Verfahren zur Bestimmung der Partikelkonzentration in Abgasen von Verbrennungsmotoren* German. Dissertation (Institute of Electronics, Technical University of Graz, 2014) (cit. on pp. 1, 3).
3. Giechaskiel, B., Alfoldy, B. & Drossinos, Y. A metric for health effects studies of diesel exhaust particles. *Journal of Aerosol Science* **40,** 639–651. ISSN: 0021-8502 (8 Aug. 2009) (cit. on pp. 1, 2).
4. U.S. EPA. *Air Quality Criteria for Particulate Matter* (U.S. Environmental Protection Agency, Washington, DC, USA, 2004) (cit. on p. 1).
5. Silverman, D. T., Samanic, C. M., Lubin, J. H., Blair, A. E., Stewart, P. A., Vermeulen, R., Coble, J. B., Rothman, N., Schleiff, P. L., Travis, W. D., Ziegler, R. G., Wacholder, S. & Attfield, M. D. The Diesel Exhaust in Miners Study: A Nested Case–Control Study of Lung Cancer and Diesel Exhaust. *JNCI: Journal of the National Cancer Institute* **104,** 855–868. ISSN: 0027-8874 (June 2012) (cit. on p. 1).
6. Pope III, C. A., Burnett, R. T., Thun, M. J., Calle, E. E., Krewski, D., Ito, K. & Thurston, G. D. Lung Cancer, Cardiopulmonary Mortality, and Long-term Exposure to Fine Particulate Air Pollution. *JAMA* **287,** 1132–1141. ISSN: 0098-7484 (Mar. 2002) (cit. on p. 1).
7. International Agency for Research on Cancer. *Diesel engine exhaust carcinogenic* `https://www.iarc.fr/news-events/iarc-diesel-engine-exhaust-carcinogenic/` (2019) (cit. on p. 1).
8. Attfield, M. D., Schleiff, P. L., Lubin, J. H., Blair, A., Stewart, P. A., Vermeulen, R., Coble, J. B. & Silverman, D. T. The Diesel Exhaust in Miners Study: A Cohort Mortality Study With Emphasis on Lung Cancer. *JNCI: Journal of the National Cancer Institute* **104,** 869–883. ISSN: 0027-8874 (11 2012) (cit. on p. 1).

9. Council of the European Union. *Council Directive 91/441/EEC of 26 June 1991 amending Directive 70/220/EEC on the approximation of the laws of the Member States relating to measures to be taken against air pollution by emissions from motor vehicles* 8 (Official Journal of the European Communities, 1991) (cit. on p. 1).

10. Council of the European Union. *Commission Regulation (EC) No 692/2008 of 18 July 2008 implementing and amending Regulation (EC) No 715/2007 of the European Parliament and of the Council on type-approval of motor vehicles with respect to emissions from light passenger and commercial vehicles (Euro 5 and Euro 6) and on access to vehicle repair and maintenance information* 130 (Official Journal of the European Communities, 2008). Appendix 1, Table 2 (cit. on pp. 1–3, 16, 94).

11. Intra, P. & Tippayawong, N. An overview of aerosol particle sensors for size distribution measurement. *Maejo International Journal of Science and Technology* **1,** 120–136. ISSN: 1905-7873 (Aug. 2007) (cit. on pp. 2, 19, 20).

12. Ferin, J., Oberdörster, G. & Penney, D. P. Pulmonary Retention of Ultrafine and Fine Particles in Rats. *American Journal of Respiratory Cell and Molecular Biology* **6,** 535–542 (Nov. 1991) (cit. on p. 2).

13. Wilson, W. E. & Suh, H. H. Fine Particles and Coarse Particles: Concentration Relationships Relevant to Epidemiologic Studies. *Journal of the Air & Waste Management Association* **47,** 1238–1249 (1997) (cit. on p. 2).

14. Giechaskiel, B., Vanhanen, J., Väkevä, M. & Martini, G. Investigation of vehicle exhaust sub-23 nm particle emissions. *Aerosol Science and Technology* **51,** 626–641 (2017) (cit. on pp. 2, 3).

15. Baron, P. A. *Aerosol measurement. Principles, Techniques, and Applications* 3rd edition. Ed. by Kulkarni, P. Ed. by Willeke, K., 6, 121, 136, 274–277, 342–349, 381–391, 413. ISBN: 978-0-470-38741-2 (John Wiley & Sons Inc., New Jersey, 2011) (cit. on pp. 2, 9, 10, 13, 16–19, 27, 83).

16. Kraft, M., Reinisch, T. & Bergmann, A. Non-reactive Working Fluids for Reliably Sensing Nanoparticles in Automotive Exhaust Gases. *Procedia Engineering* **168,** 51–54. ISSN: 1877-7058 (2016) (cit. on pp. 3, 15).

17. Giechaskiel, B., Maricq, M., Ntziachristos, L., Dardiotis, C., Wang, X., Axmann, H., Bergmann, A. & Schindler, W. Review of motor vehicle particulate emissions sampling and measurement: From smoke and filter mass to particle number. *Journal of Aerosol Science* **67,** 48–86. ISSN: 0021-8502 (2014) (cit. on pp. 3, 16, 17).

18. Rongchai, J. K. & Collings, N. *High Temperature Condensation Particle Counter (HT-CPC)* Department of Engineering, University of Cambridge. `http://www.nanoparticles.ch/archive/2012_Rongchai_PR.pdf` (2019) (cit. on pp. 3, 25).

19. Collings, N., Rongchai, K. & Symonds, J. A condensation particle counter insensitive to volatile particles. *Journal of Aerosol Science* **73,** 27–38. ISSN: 0021-8502 (2014) (cit. on pp. 3, 4, 25).

20. Kupper, M., Kraft, M., Bergmann, A. & Boies, A. High-Temperature Condensation Particle Counter Using a Systematically Selected Dedicated Working Fluid. *Aerosol Science and Technology* (2019). Manuscript submitted for publication. in revision (cit. on pp. 3, 25–27, 87, 89, 90).

21. Kügler, M. *Particle Detection and Experimental Evaluation of Different Material Combinations for Saturators of Particle Counting Devices* Master Thesis (Institute of Electronic Sensor Systems, Technical University of Graz, Graz, Jan. 2018) (cit. on pp. 3, 25, 87).

22. Donges, A. & Noll, R. *Laser Measurement Technology* Fundamentals and Applications, 26–31, 56, 57. ISBN: 978-3-662-43633-2 (Springer, Heidelberg, 2015) (cit. on pp. 5–7, 10).

23. Sun, H. *A Practical Guide to Handling Laser Diode Beams* ISBN: 978-94-017-9782-5 (Science + Business Media, Dordrecht, Heidelberg, 2015) (cit. on pp. 6, 7).

24. Meschede, D. *Optik, Licht und Laser* 3. Auflage. German, 57, 167. ISBN: 978-3-8351-0143-2 (Vieweg+Teubner, Wiesbaden, 2008) (cit. on pp. 7, 38).

25. Mie, G. Beiträge zur Optik trüber Medien, speziell kolloidaler Metallösungen. German. *Annalen der Physik, Vierte Folge* **25,** 377–445 (1908) (cit. on pp. 8, 9).

26. Kerker, M. *The Scattering of Light and Other Electromagnetic Radiation* ISBN: 9781483225241 (Academic Press Inc., Elsevier, New York, 1969) (cit. on p. 9).

27. Mongelli, G. F. An exact solution to Maxwells equation for a Sphere applied to Silver Nanoparticles. *International Journal of Chemistry, Mathematics and Physics* **25,** 12–13 (Feb. 2019) (cit. on p. 9).

28. McLinden, C. *Mie Scattering* University of Leeds. `https://www.ess.uci.edu/~cmclinden/link/xx/node19.html` (2019) (cit. on p. 10).

29. Schäfer, J.-P. *Implementierung und Anwendung analytischer und numerischer Verfahren zur Lösung der Maxwellgleichungen für die Untersuchung der Lichtausbreitung in biologischem Gewebe* German. Dissertation (University of Ulm, 2011). doi:10.18725/OPARU-1914. `http://vts.uni-ulm.de/doc.asp?id=7663` (cit. on p. 11).

30. *CRC Handbook of Chemistry and Physics. Internet Version* (ed Lide, D. R.) `http://www.hbcpnetbase.com` (CRC Press LLC, Boca Raton, FL, 2005) (cit. on pp. 11, 67).

31. Nussenzveig, H. M. *Diffraction Effects in Semiclassical Scattering* ISBN: 9780521383189. `http://www.cambridge.com/9780521383189` (Cambridge University Press, New York, 1992) (cit. on p. 11).

32. TSI Incorporated. *Ultrafine Condensation Particle Counter (CPC) 3756* (2018). https://www.tsi.com/getmedia/26bc92c7-3481-4822-b3fd-6055a8de70da/3756_US_5002015_RevB_Web?ext=.pdf (2019). P/N 5002016 Rev B (cit. on p. 13).

33. TSI Incorporated. *Condensation Particle Counter 3775. Operation and Service Manual* (2007). http://dustmonitors.ru/d/68562/d/cpc-3775r.pdf (2019). P/N 1980527 Rev D (cit. on pp. 14, 82).

34. Biswas, P., Jones, C. L. & Flagan, R. C. Distortion of Size Distributions by Condensation and Evaporation in Aerosol Instruments. *Aerosol Science and Technology* **7,** 231–246 (1987) (cit. on p. 16).

35. TSI Incorporated. *Electrostatic Classifier Model 3082. Datasheet* (2013). https://www.tsi.com/getmedia/18bb5a6c-e2c0-42a4-b5ba-928cec739eba/3082_Electrostatic%20Classifier_A4_5001530_RevA_Web?ext=.pdf (2019). P/N 5001530 Rev B (cit. on pp. 18, 19).

36. Flagan, R. C. On Differential Mobility Analyzer Resolution. *Aerosol Science and Technology* **30,** 556–570 (1999) (cit. on p. 19).

37. (ed Jing, L.) *Standard Combustion Aerosol Generator (SCAG) for Calibration Purposes* 3rd ETH Workshop Nanoparticle MeasurementAug. 9, 1999. Swiss Federal Institute of Technology ETH Zurich (Institute for Solid State Physics, ETH Hönggerberg Zürich, 1999). http://www.sootgenerator.com/documents/Pub-ETH-Workshop1999_Ji.pdf (2019) (cit. on pp. 20, 21).

38. Jing, L. *High-performance soot generators for gaseous and liquid fuel* Jing Ltd. http://www.sootgenerator.com/publ.htm (2019) (cit. on p. 20).

39. *Si PIN photodiode. High-speed photodiodes* S5971. KPIN1025E07. HAMAMATSU PHOTONICS K.K (Ichino-cho, Higashi-ku, Hamamatsu City, Japan, 2011) (cit. on pp. 22, 44, 59).

40. de Araújo, M. A. C., Silva, R., Lima, E., Pereira, D. & De Oliveira, P. Measurement of Gaussian laser beam radius using the knife-edge technique: Improvement on data analysis. *Applied optics* **48,** 393–6 (Feb. 2009) (cit. on pp. 23, 24).

41. Newport Corporation. *Motorized Actuator, LTA-HS Integrated with CONEX-CC Controller. Model: CONEX-LTA-HS* MKS Instruments. https://www.newport.com/p/CONEX-LTA-HS (2019) (cit. on p. 24).

42. Thaler, B. *Ultrafast molecular photodissociation dynamics studied with single-pulse femtosecond photoelectron-photoion-coincidence spectroscopy* Master Thesis (Institute of Experimental Physics, Technical University of Graz, Graz, Mar. 2017) (cit. on p. 24).

43. PubChem Database. *Eicosane* National Center for Biotechnology Information. https://pubchem.ncbi.nlm.nih.gov/compound/Eicosane (2019). CID=8222 (cit. on p. 25).

44. *Development And testing Of An Aerosol Sensor For Direct Measurements in Engine Exhaust* European Aerosol Conference 2018 (CTR Carinthian Tech Research AG, Villach, AT, 2018) (cit. on p. 27).

45. Demtröder, W. *Experimentalphysik 2. Elektrizität und Optik* 6. Auflage. German. ISBN: 978-3-642-29944-5 (Springer-Verlag, Berlin Heidelberg, 2013) (cit. on p. 36).

46. Frey, B. J., Leviton, D. B. & Madison, T. J. *Cryogenic temperature-dependent refractive index measurements of N-BK7, BaLKN3, and SF15 for NOTES PDT* (NASA Goddard Space Flight Center, Greenbelt, Maryland, 2007) (cit. on p. 36).

47. *APD110x/120x Operation Manual. Avalanche Photodetectors* M0009-510-963. Version 2.2.0. Thorlabs GmbH (Dachau, Germany, 2018). https://www.thorlabs.com/_sd.cfm?fileName=MTN003267-D02.pdf&partNumber=APD120A/M (2019) (cit. on p. 44).

48. *Optical Glass Specifications* Edmund Optics, Ltd. https://www.edmundoptics.de/resources/application-notes/optics/optical-glass/ (2019) (cit. on p. 64).

49. *Atomizer Aerosol Generators. ATM 220* Series ATM. Topas GmbH (Dresden, Germany, 2016). https://www.topas-gmbh.de/wordpress/dateien/produkte/200_ATMoverview_eng.pdf (2019) (cit. on pp. 76, 79).

50. *Aerosol Generators. Model 7860* Tungsten Oxide Generator. GRIMM Aerosol Technik Ainring GmbH & Co. KG (Ainring, Germany, 2018). %7Bhttps://www.grimm-aerosol.com/fileadmin/files/grimm-aerosol/3%5C%20Products/Nano%5C%20Particle%5C%20Measurement/Aerosol%5C%20Generator/7860/Product%5C%20PDFs/Generators.pdf%7D (2019) (cit. on p. 82).

51. *User's manual FLIR Ex series* # T559828. Version 2.2.0. FLIR Systems, Inc (Wilsonville, OR, U.S.A., 2017). https://www.flir.com/globalassets/imported-assets/document/flir-ex-series-user-manual.pdf (2019) (cit. on p. 86).

Appendix A.

A.1. Design drawings prototype III

Teil 1:

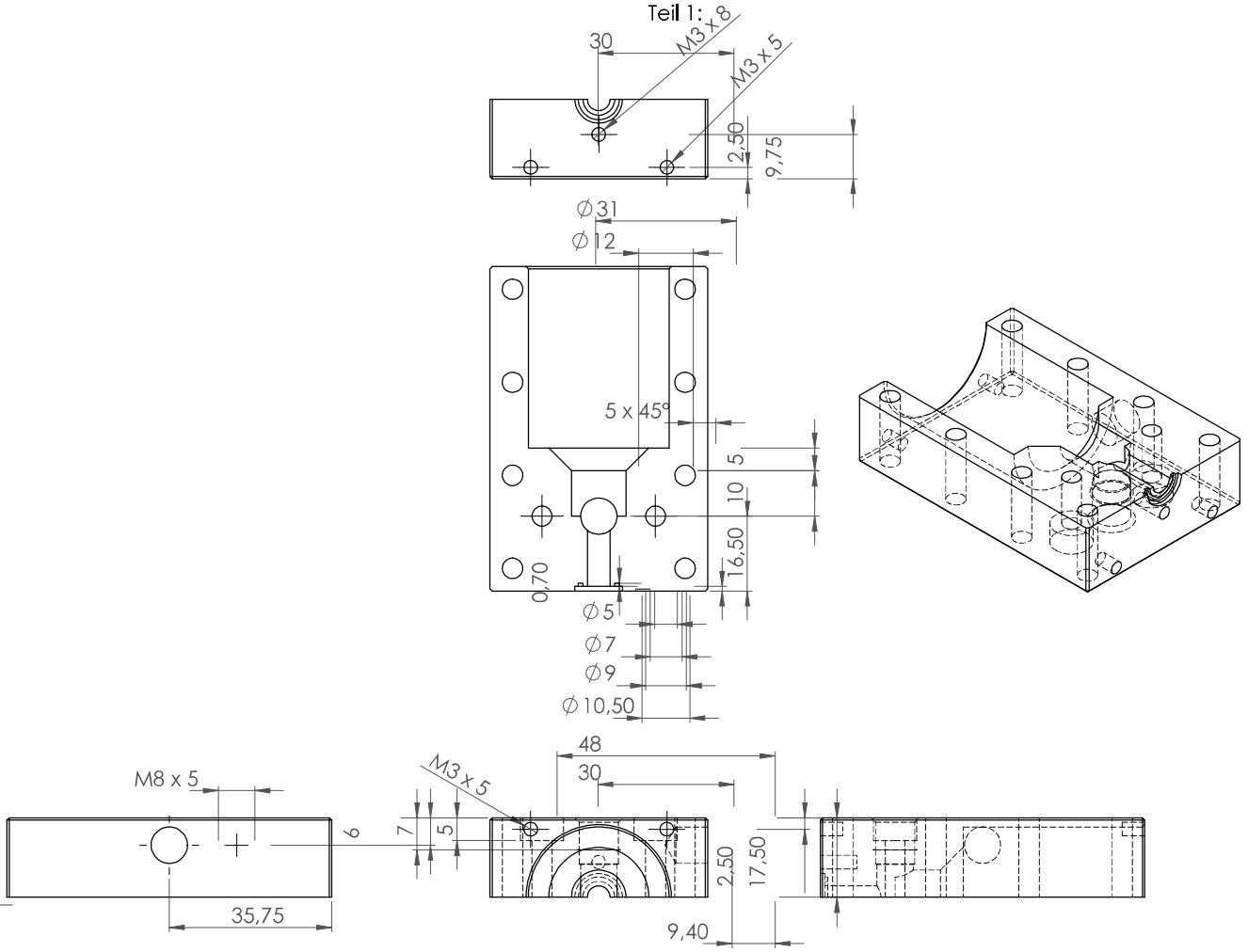
30
M3 x 8
M3 x 5
2,50
9,75
∅31
∅12
5 x 45°
5
10
16,50
0,70
∅5
∅7
∅9
∅10,50

M8 x 5
6
7
5
M3 x 5
48
30
2,50
17,50
35,75
9,40

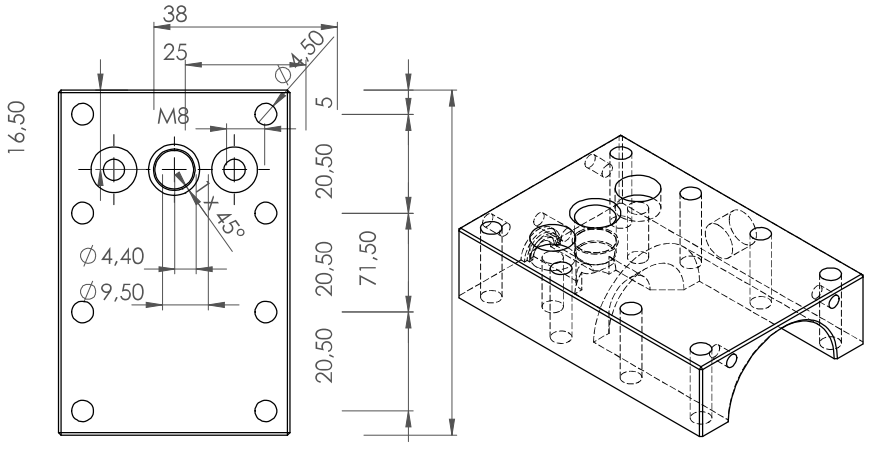
38
25
∅4,50
5
M8
16,50
20,50
20,50
20,50
71,50
45°
∅4,40
∅9,50

Teil 3:

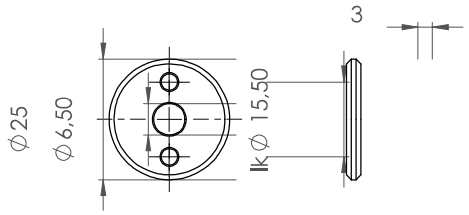
3
∅25
∅6,50
Ik∅ 15,50

Teil 2:

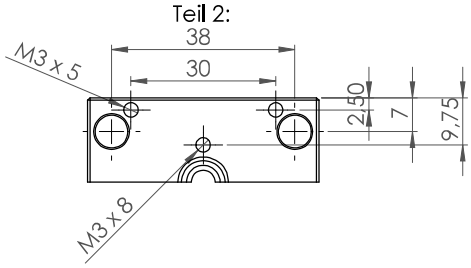

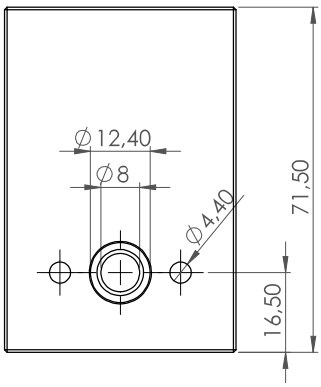

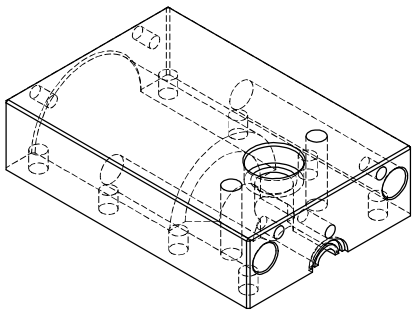

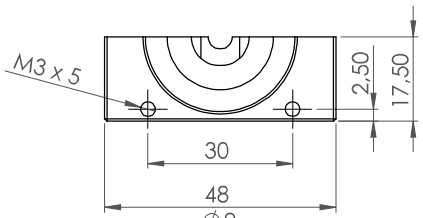

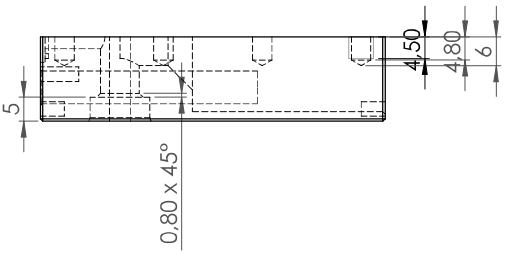

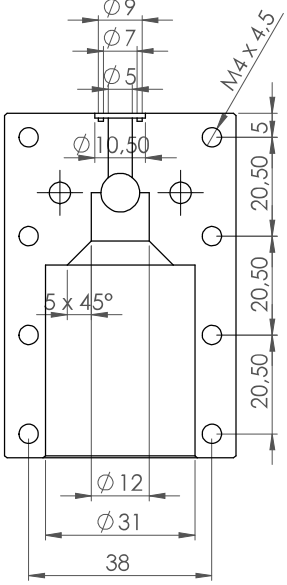

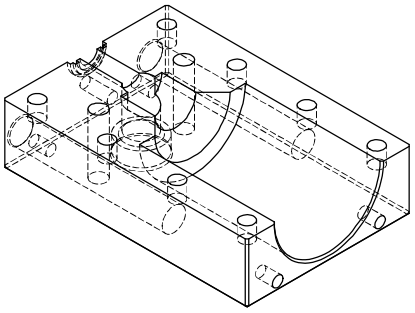

WENN NICHT ANDERS DEFINIERT: BEMASSUNGEN SIND IN MILLIMETER OBERFLÄCHENBESCHAFFENHEIT: TOLERANZEN: LINEAR: WINKEL:	OBERFLÄCHENGÜTE:				ENTGRATEN UND SCHARFE KANTEN BRECHEN	ZEICHNUNG NICHT SKALIEREN	ÄNDERUNG
	NAME	SIGNATUR	DATUM			BENENNUNG:	
GEZEICHNET	Swaschnig		2.1.19				
GEPRÜFT							
GENEHMIGT							
PRODUKTION							
QUALITÄT				WERKSTOFF: Aluminium		ZEICHNUNGSNR. Optikeinheit	A2
				GEWICHT:		MASSSTAB:1:1	BLATT 1 VON 1